

School of Industrial & ICT Engineering

**Design, Simulation, Construction and  
Characterization of a Vibrant  
Magnetic Structure for its Use in  
Magnetostrictive Energy Harvesters**



International Bachelor's Degree in  
Industrial Engineering

Bachelor's Degree Final Project

Daniel Sotelo Aguirre

Directors: Juan Jesús Beato López & Eneko Garayo Urabayen

Pamplona, January 2022

upna

Universidad Pública de Navarra  
Nafarroako Unibertsitate Publikoa



# Design, Simulation, Construction and Characterization of a Vibrant Magnetic Structure for its Use in Magnetostrictive Energy Harvesters

---

Bachelor's Degree Final Project

**Author**

Daniel Sotelo Aguirre

**Directors**

Juan Jesús Beato López

*Department of Science*

Eneko Garayo Urabayen

*Department of Science*



International Bachelor's Degree in Industrial Engineering

upna

Universidad Pública de Navarra  
Nafarroako Unibertsitate Publikoa

PAMPLONA, January 2022





## Abstract

The project consists of the design, simulation, construction and characterization of a vibrant magnetic structure for its potential use as the core of magnetostrictive vibrational energy harvesters. This element transfers the vibrations from an environmental source to the active magnetostrictive material, enabling this way the energy generation through the experienced magnetization changes and Faraday's law principles. So, its performance becomes essential in the subsequent energy conversion efficiency of the harvester device.

The first part of the project consists of several numerical simulations (by using MATLAB<sup>®</sup> and Gmsh<sup>©</sup>) to verify the viability of the design and optimize the system. This task will be done by the modification of relevant parameters to reduce the resonance frequency and maximize the stresses generated in the active material for obtaining the maximum output power. The reduction of the working frequency is justified since most of the industrial processes take place at frequencies around or even lower than 100 Hz. At this interval, the piezoelectric harvester devices, which are the most commonly used, present relevant disadvantages related to their increasing size as frequency decreases. In this context, a compact, simple, long lasting and cheap structure design could improve vibrational energy harvesting performance in industrial applications thank to the substitution of piezoelectric harvesters by magnetostrictive ones.

In the second part of the project a prototype will be built in the laboratory and it will be characterized to verify if the experimental results agree with the numerical simulations and if satisfactory performance is obtained in terms of resonance frequency and amplitude of vibration.

**Keywords:** vibrational energy harvesting; magnetostriction; low frequency vibrating systems; mechanical resonance; damping; finite element method; MATLAB<sup>®</sup>, galfenol.

## Resumen

El trabajo consiste en el diseño, simulación, construcción y caracterización de una estructura magnética vibrante para su potencial uso como base en recolectores de energía (“harvesters”) magnetostrictivos vibratoriales. Este elemento transfiere las vibraciones de una fuente del entorno al material magnetostrictivo activo, permitiendo de esta forma la generación de energía a través de los cambios experimentados en la magnetización y los principios de la ley de Faraday. Por lo tanto, su rendimiento es esencial en la siguiente conversión energética en el dispositivo recolector.

En la primera parte del trabajo se realizarán varias simulaciones numéricas (con MATLAB® y Gmsh®) para verificar la viabilidad del diseño y optimizar el sistema. Esta tarea se realizará a través de la modificación de parámetros relevantes para reducir la frecuencia de resonancia y maximizar las tensiones generadas en el material activo para obtener la máxima potencia de salida. La reducción de la frecuencia de resonancia está justificada porque la mayoría de los procesos industriales tienen lugar a frecuencias entorno a o incluso por debajo de los 100 Hz. En este rango de frecuencias los recolectores piezoeléctricos, los más comúnmente utilizados, presentan desventajas significativas relacionadas con el progresivo aumento de sus dimensiones conforme la frecuencia disminuye. En este contexto, un diseño de estructura compacta, sencilla, duradera y barata podría mejorar el rendimiento de la recolección de energía vibracional en aplicaciones industriales gracias a la sustitución de los recolectores piezoeléctricos por recolectores magnetostrictivos.

En la segunda parte del proyecto se construirá un prototipo en el laboratorio y se caracterizará para comprobar si los resultados experimentales coinciden con los resultados de las simulaciones numéricas y si se obtiene un resultado satisfactorio en términos de frecuencia de resonancia y amplitud de vibración.

**Palabras clave:** recolector de energía vibracional; magnetostricción; sistemas vibrantes de baja frecuencia; resonancia mecánica; amortiguación; método de elementos finitos; MATLAB®, galfenol.

# Acknowledgements

I would like to dedicate this space to thank all who have supported and guided me during the development of this project.

First, I would like to thank my project directors Jesús and Eneko for their implication and their guidance throughout the project. It has been a pleasure to work with you along these months. Additionally, I would like to thank Cristina for giving me the opportunity to work on this topic.

Second, I would like to thank my parents and my brother for their unconditional support. Thank you for always being there.

Finally, I would like to say a special thank to all my friends for making everything better and easier. Thanks in special to Alberto, Borja and Ion, who started this degree with me, for all the good moments that we shared together along these years.



*Engineering is the art of directing  
the great sources of power in nature  
for the use and convenience of man.*

Thomas Tredgold.



# Contents

<b>List of Figures</b>	<b>xi</b>
<b>List of Tables</b>	<b>xv</b>
<b>List of Codes</b>	<b>xvii</b>
<b>Nomenclature</b>	<b>xix</b>
<b>1. Introduction</b>	<b>1</b>
1.1. Background and motivation . . . . .	1
1.2. Scope statement . . . . .	1
1.3. Content . . . . .	2
<b>2. Literature Review and Theoretical Background</b>	<b>3</b>
2.1. Internet of Things and Energy Harvesters Context . . . . .	3
2.2. Vibration Energy Harvesters . . . . .	6
2.3. Magnetostrictive Vibration Energy Harvesters . . . . .	8
2.3.1. Energy Transfer and Transformation . . . . .	8
2.3.2. Magnetostriction and Villari Effect . . . . .	8
2.3.3. Magnetostrictive Materials . . . . .	10
2.3.4. Electromagnetic Coupling . . . . .	12
2.3.5. Harvester Configuration Examples . . . . .	13
2.3.5.1. Axial Type Harvesters . . . . .	13
2.3.5.2. Bending Type Harvesters . . . . .	13
2.4. Structural Analysis . . . . .	15
2.4.1. General Formulation of the Linear Elasticity Model . . . . .	16
2.4.2. Elastostatics . . . . .	17
2.4.3. Elastodynamics . . . . .	18
2.4.3.1. Mechanical Resonance and Eigenfrequency Analysis . . . . .	18
2.4.3.2. Damping . . . . .	19
<b>3. Harvester Design and Simulation</b>	<b>21</b>
3.1. Initial Design . . . . .	21
3.2. Mechanical Simulations . . . . .	23
3.2.1. Finite Element Method . . . . .	23

---

3.2.2.	Software Used in the Simulations . . . . .	24
3.2.2.1.	SolidWorks® . . . . .	24
3.2.2.2.	MATLAB® . . . . .	24
3.2.2.3.	Gmsh® . . . . .	25
3.2.3.	Geometry Definition . . . . .	25
3.2.4.	Meshing of the Harvester Geometry . . . . .	26
3.2.5.	PDE Problem Definition . . . . .	30
3.2.6.	Resonance Frequencies and Modes of Vibration . . . . .	31
3.2.7.	Static Simulation (Gravity Load) . . . . .	33
3.2.8.	Dynamic Simulation (Harmonic Load) . . . . .	34
<b>4.</b>	<b>Harvester Vibrating Magnetic Structure Characterization</b>	<b>37</b>
4.1.	U-shaped Main Body Characterization . . . . .	37
4.2.	Laboratory Material . . . . .	38
4.2.1.	Generation of Ambient Vibration . . . . .	39
4.2.1.1.	Shaker . . . . .	39
4.2.1.2.	Function Generator . . . . .	40
4.2.1.3.	AC Amplifier . . . . .	40
4.2.1.4.	Ammeter . . . . .	41
4.2.1.5.	Accelerometer . . . . .	41
4.2.1.6.	3D-printed Harvester Support . . . . .	41
4.2.2.	Characterization of U-shaped Body Vibration . . . . .	42
4.2.2.1.	Vibration Magnetic Sensor . . . . .	42
4.2.2.2.	Sensor Circuit Board . . . . .	44
4.2.2.3.	Oscilloscope . . . . .	46
4.3.	Experimental Measurements . . . . .	46
4.3.1.	Determination of the Optimal Tip-Sensor Distance . . . . .	46
4.3.2.	Calibration of the Displacement Sensor . . . . .	47
<b>5.</b>	<b>Results and Discussion</b>	<b>51</b>
5.1.	U-shaped Harvester Body . . . . .	51
5.2.	Potential Harvester Construction . . . . .	53
5.2.1.	U-shaped Harvester Body with Galfenol Sheet and 3D-printed Piece . . . . .	53
5.2.1.1.	Galfenol Sheet . . . . .	54
5.2.1.2.	Copper Wiring . . . . .	55
5.2.1.3.	Resonance Analysis . . . . .	55
5.2.2.	U-shaped Harvester Body with Galfenol Sheet, 3D-printed Piece and Additional Tip Mass . . . . .	57
5.2.2.1.	Tip Mass . . . . .	57
5.2.2.2.	Resonance Analysis . . . . .	58
5.3.	Comparison between Theoretical and Empirical Results . . . . .	60

---



---

<b>6. Conclusions and Future Work</b>	<b>65</b>
6.1. Main Conclusions . . . . .	65
6.2. Future Work Lines . . . . .	66
6.2.1. Harvester Performance Determination . . . . .	66
6.2.2. Mechanical-Magnetic Coupling and Electromagnetic Induction Numerical Simulations . . . . .	67
6.2.3. Real Applications Implementation . . . . .	67
<b>Bibliography</b>	<b>69</b>
<b>A. Vibrant Magnetic Structure and Support Technical Drawings</b>	<b>73</b>
<b>B. Optimal Galfenol Sheet Selection for the Future Harvester</b>	<b>89</b>
<b>C. MATLAB® Scripts</b>	<b>93</b>
C.1. MechanicalSimulation.m . . . . .	93
C.2. animateHarvester.m . . . . .	99
C.3. calc_vol_average.m . . . . .	101
C.4. ExperimentalData.m . . . . .	102
C.5. GalfenolMagnetizationModel.m . . . . .	104

---



# List of Figures

2.1.	IoT applications examples and overall integration . . . . .	3
2.2.	Global number of connected IoT devices . . . . .	4
2.3.	Scheme of the different IoT applications energy sources . . . . .	5
2.4.	Devices power consumption and possible harvested power from different sources . . . . .	5
2.5.	Vibration energy harvesters classification . . . . .	6
2.6.	Energy flow diagram of a magnetostrictive vibration energy harvester .	8
2.7.	Effect of an external magnetic field, $\mathbf{H}$ , on the shape of a simplified ferromagnetic material with positive magnetostriction after saturation .	9
2.8.	Villari effect diagram . . . . .	10
2.9.	Absolute magnetostrictive coefficients of different materials . . . . .	11
2.10.	General axial magnetostrictive energy harvester configuration and an application for extracting energy from human walking . . . . .	13
2.11.	Unimorph single-layer and composite and bimorph magnetostrictive energy harvesters . . . . .	14
2.12.	U-shaped unimorph magnetostrictive vibration energy harvester . . . .	15
2.13.	Diagram for the elastic model . . . . .	15
2.14.	Different modes of vibration of a string tied at its two ends . . . . .	19
3.1.	U-shape magnetostrictive vibration energy harvester configuration proposed by Ueno . . . . .	21
3.2.	Behavior of the U-shape harvester under vibrations . . . . .	22
3.3.	2D and 3D FEM examples . . . . .	23
3.4.	Harvester domains identification . . . . .	25
3.5.	U-shape magnetostrictive vibration energy harvester geometry created with SolidWorks® . . . . .	26
3.6.	Detail on the geometry of the fixed end of the harvester . . . . .	26
3.7.	Volumes and physical volumes in Gmsh® . . . . .	28
3.8.	Mesh generated by Gmsh® . . . . .	29
3.9.	Comparison between the mesh generated by MATLAB® and Gmsh® . .	29
3.10.	Harvester domains and faces identification . . . . .	30
3.11.	Frame of the animation of the harvester modes of vibration . . . . .	32
3.12.	Displacement in the $z$ direction (mm) and $\sigma_{xx}$ stresses (MPa) under static loading for the two-domain geometry . . . . .	33

---

4.1. U-shaped iron main body . . . . .	38
4.2. Laboratory setup . . . . .	38
4.3. Laboratory setup connections . . . . .	39
4.4. LDS <sup>®</sup> V201 permanent magnet shaker . . . . .	39
4.5. AFG310 SONY Tektronix Arbitrary Function Generator . . . . .	40
4.6. LDS <sup>®</sup> LPA100 linear power amplifier . . . . .	40
4.7. 34401A Agilent multimeter . . . . .	41
4.8. TLD352C33 ICP <sup>®</sup> sensor and 480C02 ICP <sup>®</sup> signal conditioner . . . . .	41
4.9. 3D-printed support details . . . . .	42
4.10. Electric impedance versus external magnetic field . . . . .	43
4.11. Displacement sensor . . . . .	43
4.12. Signal deconvolution diagram . . . . .	44
4.13. Analog homemade electronic interface schematic . . . . .	45
4.14. Analog homemade electronic interface . . . . .	45
4.15. Tektronix MDO3024 Oscilloscope . . . . .	46
4.16. Calibration of the displacements sensor . . . . .	48
5.1. Frequency sweep of the U-shaped harvester body . . . . .	53
5.2. As-cast Galfenol sheet . . . . .	54
5.3. U-shaped iron body with and without glued Galfenol sheet . . . . .	54
5.4. U-shaped body with Galfenol sheet and 3D-printed wiring piece . . . . .	55
5.5. Structure body with Galfenol sheet and 3D-printed piece oscillating in resonance . . . . .	55
5.6. Frequency sweep of the U-shaped harvester body with Galfenol sheet and 3D-printed piece . . . . .	57
5.7. Structure body with Galfenol sheet, 3D-printed piece and additional tip mass . . . . .	58
5.8. Frequency sweep of the U-shaped harvester body with Galfenol sheet, 3D-printed piece and additional tip mass . . . . .	59
5.9. Comparison between the resonance analyses at a constant shaker vibration amplitude of 0.1 mm . . . . .	60
5.10. Comparison of theoretical and empirical results of the U-shaped body . . . . .	61
5.11. Displacement in the $z$ direction (mm) and $\sigma_{xx}$ stresses (MPa) under dynamic loading for the two-domain geometry . . . . .	62
B.1. Galfenol magnetization curves for the two built-in stresses available from the manufacturer TdVib LLC . . . . .	90

---

# List of Tables

2.1. Summary of the advantages and disadvantages of the different vibration energy harvester types . . . . .	7
2.2. Material properties of Fe–Co alloys, Terfenol–D and Galfenol . . . . .	12
3.1. Materials mechanical properties . . . . .	30
3.2. Frequencies of resonance corresponding to first six modes of vibration .	31
4.1. Calibration of the displacement sensor . . . . .	48
5.1. Data from the frequency sweep analysis of the U-shaped harvester body	52
5.2. Data from the frequency sweep analysis of the U-shaped harvester body with Galfenol sheet and 3D-printed piece . . . . .	56
5.3. Data from the frequency sweep analysis of the U-shaped harvester body with Galfenol sheet, 3D-printed piece and additional tip mass . . . . .	58
5.4. Damping coefficients determination . . . . .	61
C.1. Inputs and outputs of the function animateHarvester.m. . . . .	99
C.2. Inputs and outputs of the function cal_vol_average.m. . . . .	101



# List of Codes

3.1. Gmsh <sup>®</sup> Domain Assignment and Meshing Parameters for the two-domain geometry . . . . .	27
3.2. Gmsh <sup>®</sup> Domain Assignment and Meshing Parameters for the four-domain geometry . . . . .	27
C.1. Geometry and PDE Problem Definition . . . . .	93
C.2. Coefficients Definition and Boundary Conditions . . . . .	93
C.3. Mesh Generation . . . . .	95
C.4. Solution: Resonance Frequencies . . . . .	95
C.5. Animation of the Prototype's First 6 Modes of Vibration . . . . .	95
C.6. Solution: Gravity Load, Deformations and Stresses . . . . .	96
C.7. Damping Coefficients Determination . . . . .	96
C.8. Solution: Harmonic Load, Deformations and Stresses . . . . .	97
C.9. Stresses in the magnetostrictive material . . . . .	98
C.10. Function animateHarvester.m . . . . .	99
C.11. Function calc_vol_average.m . . . . .	101
C.12. Calibration of the Displacements Sensor (Figure 4.16) . . . . .	102
C.13. Frequency sweep of the first prototype configuration (Figure 5.1) . . . . .	102
C.14. Frequency sweep of the second prototype configuration (Figure 5.6) . . . . .	102
C.15. Frequency sweep of the third prototype configuration (Figure 5.8) . . . . .	103
C.16. Comparison between the resonance analyses (Figure 5.9) . . . . .	103
C.17. Galfenol Magnetization Function Model . . . . .	104





# Nomenclature

## Acronyms

AC	Alternating Current
AM	Amplitude Modulation
DC	Direct Current
emf	Electromotive force
FEM	Finite Element Method
GMI	Giant Magnetoimpedance
IoT	Internet of Things
MEMS	Micro-electromechanical Systems
OA	Operational Amplifier
PDE	Partial Differential Equation
PLA	Polylactic Acid
RF	Radiofrequency
RMS	Root Mean Square
SoC	System on Chip
WJC	Water Jet Cutting

## Greek Letters

$\alpha$	First Rayleigh parameter
$\beta$	Second Rayleigh parameter
$\delta\Omega$	Geometric domain boundaries
$\varepsilon$	Strain tensor
$\varepsilon_{ind}$	Induced electromotive force
$\lambda$	First Lamé parameter
$\lambda_s$	Saturation magnetostrictive coefficient
$\mu$	Magnetic permeability

---

$\nu$	Poisson coefficient
$\rho$	Density
$\boldsymbol{\sigma}$	Stress tensor
$\bar{\sigma}$	Actions boundary condition
$\tau$	Shear stress
$\Omega$	Geometric domain
$\omega$	Angular frequency
$\omega_n$	Natural frequency

## Latin Letters

$A_0$	Acceleration peak amplitude
$A_c$	Coil's cross section
$\mathbf{B}$	Magnetic flux density vector
$\mathbf{C}$	Damping matrix
$\mathbf{c}$	Matrix relating displacements and stresses
$E$	Young modulus
$E_\sigma$	Uniaxial magnetic anisotropy energy
$f$	Frequency
$G$	Second Lamé parameter
$g$	Gravitational acceleration
$\mathbf{H}$	Magnetic field intensity vector
$I_{RMS}$	Root mean square AC current intensity
$\mathbf{K}$	Stiffness matrix
$\mathbf{M}$	Bulk saturation magnetization vector
$\mathbf{M}$	Mass matrix
$\mathbf{M}_s$	Saturation magnetization vector
$\mathbf{m}$	Domain magnetization vector
$m$	Mass
$N_c$	Number of coil turns
$t$	Time
$\mathbf{u}$	Displacement vector
$\mathbf{u}_0$	Displacement amplitude vector
$\ddot{\mathbf{u}}$	Acceleration vector

---

---

$\bar{u}$	Supports boundary condition
$V_{App}$	Peak-to-peak accelerometer voltage signal
$V_{out}$	Peak-to-peak displacement sensor voltage signal
$\mathbf{X}$	Volume forces vector
$\mathbf{X}_0$	Volume forces amplitude vector
$X_0$	Prototype displacement amplitude
$Y_0$	Shaker displacement amplitude

---



# Chapter 1

## Introduction

### 1.1. Background and motivation

The current work is presented as a Bachelor's Thesis (Trabajo Fin de Grado) in Industrial Engineering, with a workload corresponding to 12 ECTS. The motivation about magnetostrictive harvesters to collect energy from ambient vibrations was obtained from the proposal to participate in this line of research by the Sciences Department of the Public University of Navarre (UPNA).

The knowledge background about this topic was acquired throughout several subjects of the Bachelor's degree such as, among others, Further Studies in Physics, Advanced Physics, Elasticity and Strength of Materials and Design and Testing of Machines; and was highly enriched during the progress of this work.

### 1.2. Scope statement

The majority of industrial processes have associated the generation of vibrations at relatively low frequencies (around 100 Hz). These environmental vibrations can be used for the generation of green electrical energy through energy harvesting principles. Within vibration harvesters, those based in piezoelectric materials are the most commonly employed, however, at this frequency interval, these devices display some disadvantages principally related to their gradually larger size when the frequency of vibration is reduced. This way, the main objective of the project is the design and optimization, based upon mechanical criteria, of a U-shaped vibrant magnetic structure to be employed as the core of a potential magnetostrictive harvester to substitute piezoelectric ones in low-frequency industrial applications.

The importance of this analysis relies on the fact that this structure represents the basis of any magnetostrictive vibrational energy harvester, since its performance

strongly determines the efficiency of the energy transformation from the initial mechanical energy (vibration) to the final electrical energy. This performance highly depends on the mechanical properties of the vibrant structure, and on the design parameters, fundamentally, the resonance frequency, the stresses and the displacement amplitudes under vibration. The optimization of these parameters becomes the sub-objective of this study. Their enhancement enables the design of a low resonance frequency, compact, easily manufactured, long-lasting and cheap device. Its simpler and low cost features will permit the massive application to any type of industrial process and even at remote locations, permitting the piezoelectric-based devices substitution.

The design is carried out with SolidWorks® CAD software and it is optimized in the programming environment of MATLAB®, by performing both static and dynamic mechanical simulations. Then a prototype is built being its performance compared with the one predicted by the numerical simulations.

### **1.3. Content**

The project has been organized in six chapters which are recommended to be read in order. This present Chapter 1 exposes an introduction to the project and defines the scope and the content. Chapter 2 introduces the reader to the subject of magnetostrictive harvesters and the importance of the mechanical properties of the structure on the performance of the device. In this chapter, literature is reviewed in order to know which is the current state of the art. Chapter 3 summarizes the design procedure by performing mechanical simulations in order to obtain the theoretical results. Chapter 4 explains in detail the prototype construction, the laboratory equipment and the procedure followed to take the experimental measurements as well as the obtained experimental results. In Chapter 5 the obtained results are discussed and the theoretical and experimental results are contrasted. Finally, in Chapter 6 the author's conclusions about this project and future work lines are exposed. The technical drawings of the designed harvester structure and 3D-printed support needed for the lab measurements are collected in Appendix A. In Appendix B it is shown the procedure to choose the optimal magnetostrictive material for the construction of the future harvester. The MATLAB® scripts for the mechanical simulations and the plots are collected in Appendix C.

---

# Chapter 2

## Literature Review and Theoretical Background

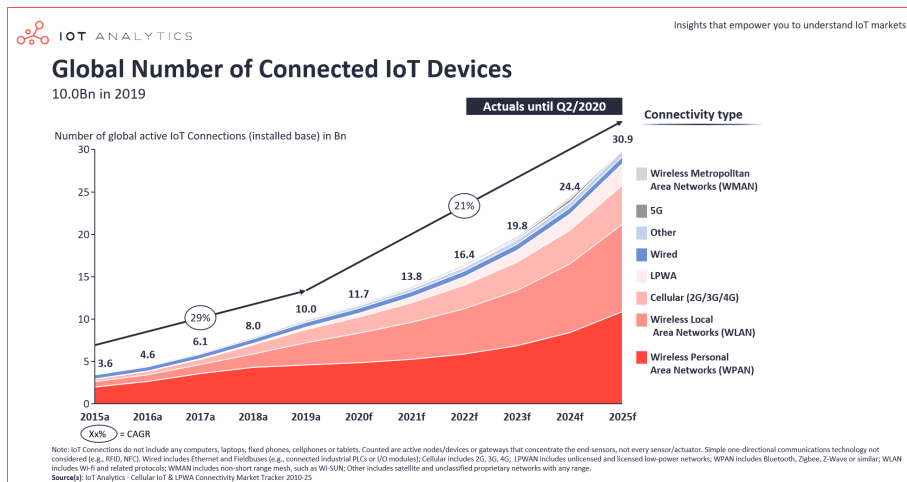
### 2.1. Internet of Things and Energy Harvesters Context

In the past few decades the development of wireless devices has experimented a huge growth thanks to the comfort and high number of possibilities they provide [1]. One of the applications of these wireless devices is to use them as sensors which can monitor and gather information from different systems in order to analyze their behavior and accordingly generate external responses. The technology involving the creation of interacting wireless sensor networks connected to the Internet which can interact between them is known as the Internet of Things (IoT). It is a line of research broadly used in relevant fields such as health monitoring, home and industrial automation or security (see Figure 2.1); and expected to have even more importance in the future [1].



Figure 2.1: IoT applications examples and overall integration [2].

Applications of IoT have become almost infinite thanks to the rapid development of the implicated technologies [3]. These sensors have achieved to be of a very small size and power consumption thanks to the Systems on Chip (SoCs), which are integrated circuits including all the different modules typical from a computer [4]. The networks of communication for these kind of devices have also experimented great development in order to achieve greater range with less power consumption. With respect to their source of power, the current most common choice is the use of batteries, due to the simplicity of their installation. However, their main drawback is that they require of certain maintenance since they have to be replaced periodically. This fact joined to the expected growth of IoT devices (see Figure 2.2) results in a scenario determined by a great expense of resources and negative environmental impact. On the other hand, self-powered sensors seem to be the solution to this problem, and have become of high interest in the last few years to provide the IoT devices with energy in the most efficient way [3].

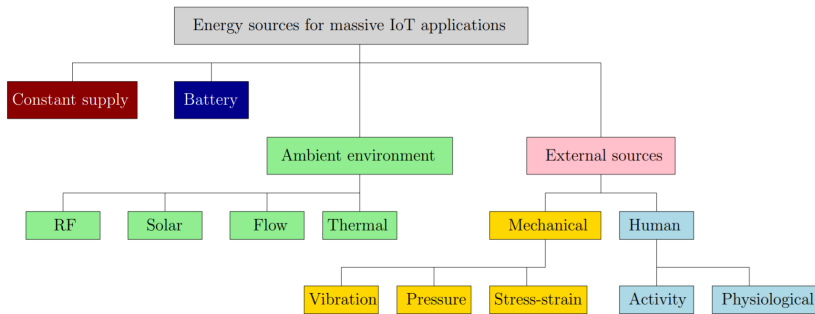


**Figure 2.2:** Global number of connected IoT devices [5].

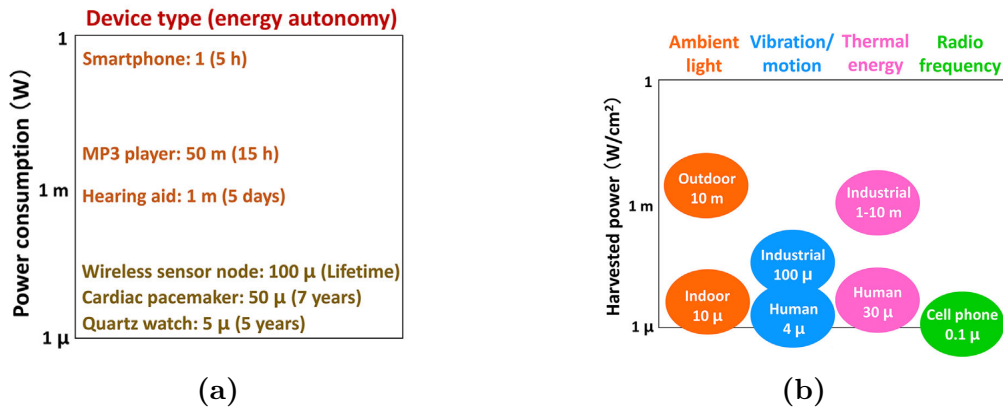
One interesting possibility is to convert ambient energy into electrical energy to feed this type of mechanisms. The extraction of the energy present in the device body or in its surrounding environment, which would otherwise dissipate, is what it is called energy harvesting. In the case of low power and low and mid-range applications, the sensors could be self-powered under this principle, avoiding the necessity of batteries [6]. In the case of medium power applications where batteries are required or for long-range communications, energy harvesters can be employed for increasing batteries life-time and for recharging them [6]. Energy harvesters would therefore contribute to moderate the environmental impact at the time that they reduce the maintenance costs associated to the batteries replacement. In addition to that, these devices can be implemented in remote and difficult-access places where regular battery maintenance is unfeasible.



Different types of harvesters can be found depending on the ambient source chosen to power the IoT devices. The most common are: heat (thermal energy), vibrations (mechanical energy) and electromagnetic waves (radio-frequency energy, RF) [6]. Figure 2.3 shows a scheme with the most common energy sources for IoT applications. Not every source of energy will be adequate for powering any device. A previous analysis to compare the consumption of the powered target component and the energy harvested by each source has to be made. Figure 2.4 shows the power consumption of some selected technological devices and a comparison between the approximated harvested power of each energy source.



**Figure 2.3:** Scheme of the different IoT applications energy sources [6].



**Figure 2.4:** (a) Typical power consumption of some selected battery-powered technological devices. (b) Harvested power from different environment energy sources [1].

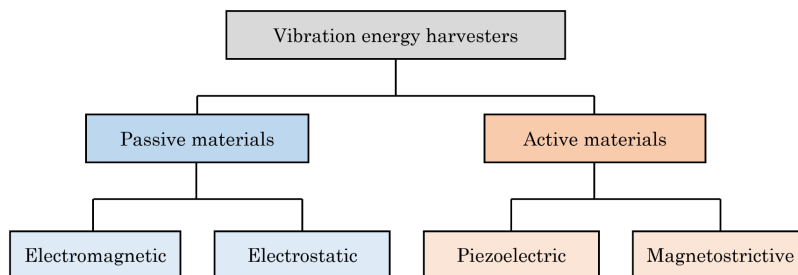
Anyway, a common characteristic of harvesting systems is that the energy generation procedure is generally developed by a functional or active material [7], namely those materials in which external stimuli (temperature, pressure, etc.) enable to control one or more of their properties. Nevertheless, passive materials (materials in which no property can be controlled by external stimuli) are also used. A great investment is expected to be made by companies to develop and perfect these technologies [1].

## 2.2. Vibration Energy Harvesters

Among the different energy sources, this work centers on vibration energy harvesters. Structural vibrations seem to be one of the most promising sources [7] since they are present in many different locations, including industrial environments. For instance, solar energy, which can be harvested based on the photoelectric effect, presents high dependence on the weather. Thermal energy, based on the thermoelectric effect, presents difficulties to achieve the sufficient temperature difference to obtain the desired power output. Finally, the power obtained from electromagnetic waves is generally very low (microwatts) and it is significantly reduced when distance from the radio frequency source increases.

Consequently, vibration harvesters present a large field of applications. To maximize the power output, both the frequency range and amplitude of the potential vibrations have to be deeply analyzed. As a result, several types of harvesters have been developed due to the great range of vibration sources. For example, buildings and bridges show low frequencies ( $\leq 0.1$  Hz) and low amplitudes ( $\leq 0.1$  g); home appliances show moderate frequencies ( $\leq 150$  Hz) and amplitudes ( $\leq 0.5$  g) [8]; and motors of automobiles and heavy machinery show high amplitudes and a frequency which strongly depends on the engine speed. This work is focused on the common industrial processes with vibrations at frequencies around 100 Hz [9] and acceleration amplitudes around  $10 \text{ m/s}^2$  [9].

Similar to the general classification, vibration energy harvesters can also employ passive or active materials [7] for energy generation (see Figure 2.5). In general, active-based devices exhibit more advantages since they offer a higher coupling between the mechanical and electrical domain [10] (explained in more detail in Section 2.3.4).



**Figure 2.5:** Vibration energy harvesters classification.

Attending to passive materials-based harvesters, two different types can be found: electrostatic and electromagnetic. Electrostatic energy harvesters act as variable capacitors (pair of electrodes with a dielectric layer in between whose distance changes due to the vibrations). As the electrodes are charged at the beginning, the change of

distance between them induces alternating currents (AC). On the other hand, electromagnetic harvesters use coils and permanent magnets to generate the electrical energy. Their working principle is based on Faraday's law. Briefly, when vibration occurs a relative movement between the magnet and the coil results, enabling the induction of an AC voltage between the coil terminals and therefore the energy generation.

On the other side, active materials-based devices can also be divided into two groups, explicitly: piezoelectric and magnetostrictive materials. Piezoelectric energy harvesters are based on the piezoelectric effect [1]. As commented before, these devices are the most commonly employed, however, they present several drawbacks such as the brittleness of the piezoelectric materials, the high output impedance signal that requires complex signal condition electronics and their larger sizes as frequency decreases ( $\leq 100$  Hz). These disadvantages can be overcome with the use of magnetostrictive harvesters [7]. They are based on materials that usually present higher mechanical strength and lower output impedance signal when compared with piezoelectrics. These characteristics permit an easy fabrication procedure, turning magnetostrictive harvesters into long-lasting generators with a longer useful life and with a clear applicability at low frequencies. Nevertheless, they require the use of coils and magnets for their fabrication, hindering their integration with micro-electromechanical systems (MEMS). A summary of the advantages and disadvantages of each vibration energy harvester type can be seen in Table 2.1.

**Table 2.1:** Summary of the advantages and disadvantages of the different vibration energy harvester types [3].

Type	Advantages	Disadvantages
Electromagnetic	-no need of active material -no external voltage source	-bulky size: magnets and pick-up coil -difficult to integrate with MEMS -max. voltage of 0.1 V
Electrostatic	-no need of active material -compatible with MEMS -voltages of 2–10 V	-external voltage (or charge) source -mechanical constraints needed -capacitive
Piezoelectric	-no external voltage source -high voltages of 2–10 V -compact configuration -compatible with MEMS -high coupling in single crystals	-depolarization -brittleness in bulk piezolayer -poor coupling in piezo-film -charge leakage -high output impedance
Magnetostrictive	-high mechanical-electrical coupling -no problems of depolarization -high flexibility -suited to low frequency vibration	-nonlinear effect -pick-up coil -may need bias magnets -difficult to integrate with MEMS

## 2.3. Magnetostrictive Vibration Energy Harvesters

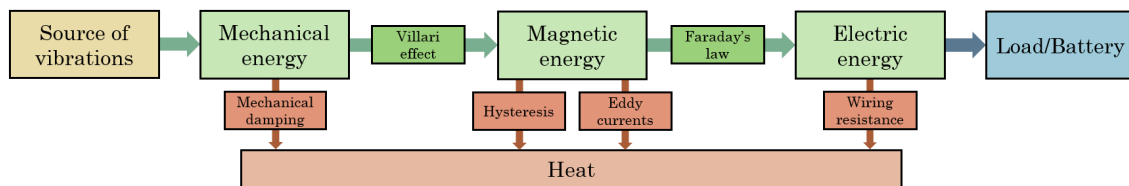
### 2.3.1. Energy Transfer and Transformation

Generally, two steps can be considered in the energy generation procedure developed by the magnetostrictive harvesters.

- The transformation of the mechanical energy of the external vibration into magnetic energy by means of the inverse magnetostrictive (or Villari) effect experienced by the active magnetostrictive material.
- The conversion of the magnetic energy into electrical (electromagnetic-coupling) governed by Faraday's law principles.

In a few words, electrical energy generation is produced when the ambient vibrations of the source are transmitted to the magnetostrictive material. As a consequence, the active or magnetostrictive material experiences variable mechanical stresses that generate different magnetization states and thus, a variable magnetic flux through the collecting coil. Therefore, the transmission of the ambient vibrations to the active material is essential for the harvester performance and subsequent energy conversion efficiency. Consequently, a meticulous design stage of the harvester vibrating magnetic structure is strictly required for obtaining an optimized response, since this element is the one responsible of transferring the vibration to the magnetostrictive material fixed on it.

In a second order of relevance, other aspects such as mechanical damping and the reorientation of magnetic domains in the material (hysteresis) may introduce some energy losses that affect to the energy generation efficiency. The overall energy flow description can be graphically seen in Figure 2.6.



**Figure 2.6:** Energy flow diagram of a magnetostrictive vibration energy harvester.

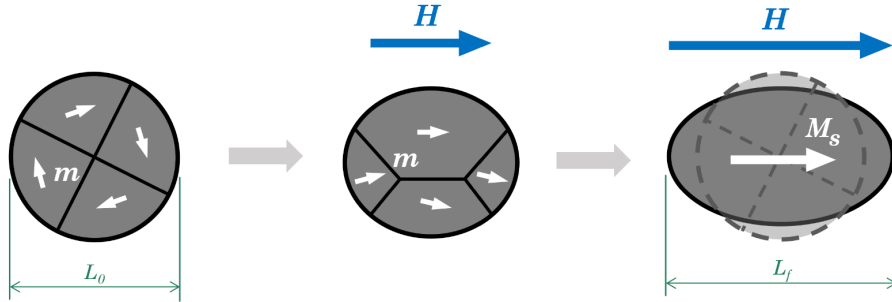
### 2.3.2. Magnetostriction and Villari Effect

Magnetostriction was first measured by J. P. Joule in 1842 when he magnetized an iron sample and measured its length change. It can be defined as the property of

ferromagnetic materials that produces a dimension change when they are exposed to an external magnetic field.

Ferromagnetic materials are internally divided into magnetic domains. These regions can be defined as the areas of the material where the magnetization points in the same direction. The boundaries between domains are called domain walls. Although both elements affect magnetostriction, our analysis will be developed under the Stoner-Wohlfarth approximation that considers only the effect of non-interacting domains for the explanation of the phenomenon.

As Figure 2.7 illustrates, after applying an external magnetic field,  $\mathbf{H}$ , the magnetic domains start to orient in the magnetic field direction. When the external field is further increased a saturation state is reached (the magnetization of every domain is in the same direction, acting as a single domain with saturation magnetization  $\mathbf{M}_s$ ). Depending on the magnetostriction sign an increase (positive magnetostriction) or shrinkage (negative magnetostriction) in its length results. This effect is generally quantified by the saturation magnetostriction constant,  $\lambda_s = \frac{\Delta L}{L_0}$  which is defined as the variation in length  $\Delta L$  (length in the saturated state,  $L_f$ , minus the initial length,  $L_0$ ), divided by the initial length in the demagnetized state.



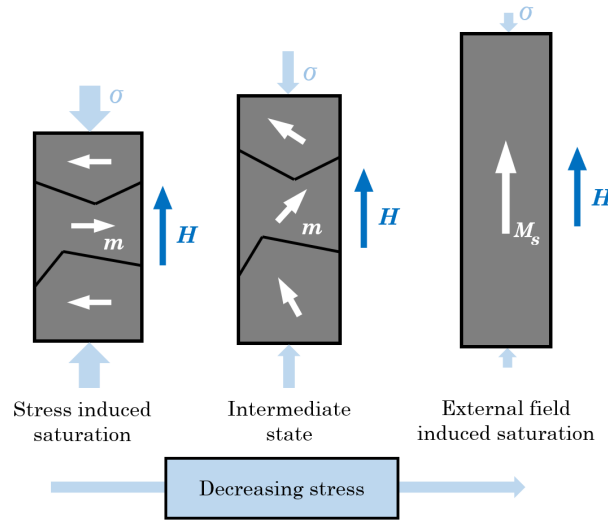
**Figure 2.7:** Effect of an external magnetic field,  $\mathbf{H}$ , on the shape of a simplified ferromagnetic material with positive magnetostriction after saturation.

Anyway, magnetostrictive harvesters are based on the inverse magnetostrictive effect (or Villari effect) discovered in 1865 by the Italian physicist E. Villari. It consists on a change on the material magnetization  $\mathbf{M}$  (for a given external field  $\mathbf{H}$ ) when the sample is subjected to mechanical stresses,  $\sigma$ .

The case of a single magnetic domain will be analyzed to understand the effect of the sign of  $\lambda_s$  in the behavior of a magnetostrictive material under external stresses. The application of uniaxial stress,  $\sigma$ , would lead to the induction of a uniaxial magnetic anisotropy energy,  $E_\sigma$ , that comes given by Equation 2.1 [11].

$$E_\sigma = \frac{3}{2} \lambda_s \sigma \sin^2 \theta \quad (2.1)$$

In the equation,  $\theta$  is the angle formed by  $\mathbf{M}_s$  and the direction of application of the stress. Depending on the sign of both  $\lambda_s$  (positive or negative magnetostriction) and  $\sigma$  (material subjected to tension,  $\sigma > 0$ , or compression,  $\sigma < 0$ ); two different lower-energy states are possible. If both parameters have the same sign the state of lower energy corresponds to  $\theta = 0^\circ$  (external field saturated state in Figure 2.8). On the other hand, if they have opposite sign, the state with lower energy corresponds to  $\theta = 90^\circ$ , according to Equation 2.1, which is a demagnetized state (see stress induced saturation in Figure 2.8). This means that for instance, tensile stresses favor the alignment of magnetization in the direction of the applied stress or perpendicular to it depending on whether  $\lambda_s$  is positive or negative respectively. An opposite behavior is found under compressive stresses.



**Figure 2.8:** Villari effect diagram.

Figure 2.8 exemplifies this equation for a material with positive  $\lambda_s$  under compressive ( $\sigma < 0$ ) loading. When the compressive stress applied is large, the magnetic domains tend to rotate and their magnetization is oriented in the direction perpendicular to the one of the external field ( $\theta = 90^\circ$ ); so the bulk magnetization  $\mathbf{M}$  (weighted sum of the magnetization of each of the domains  $\mathbf{m}$ ) is zero. As the compression is decreased, considered as the application of progressively more intense tensile stresses, magnetic domains start to align with the external field until reaching saturation.

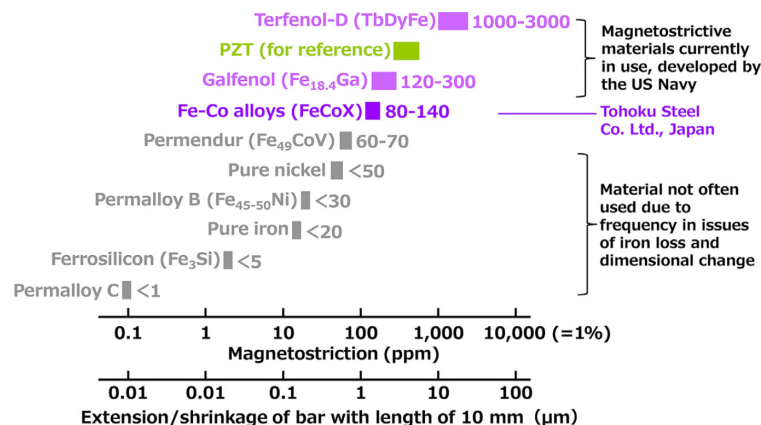
### 2.3.3. Magnetostrictive Materials

From Villari effect it is known that the higher the magnetostriction coefficient, the greater the magnetization of the material for a given stress. This way, high magnetostriction materials will be the ones of interest to be coupled to the designed vibrating

structure. Different materials have been used for constructing magnetostrictive harvesters. Among the most relevant the following can be found.

- Terfenol–D: It is an alloy of rare elements,  $\text{Tb}_{0.3}\text{Dy}_{0.7}\text{Fe}_2$ . It has the highest room-temperature magnetostrictive coefficient. Its main disadvantages are its high cost and its brittleness.
- Galfenol: It is an iron–gallium (Fe–Ga) alloy that exhibits also a large magnetostriction, although lower than Terfenol–D. It is highly used due to its good trade-off between magnetostriction and mechanical properties (i.e. much higher ultimate tensile strength than Terfenol–D, see Table 2.2). This optimum combination enables this material to be machined with conventional machining techniques, forged, rolled, drawn and welded to other ferrous materials while maintaining excellent magnetic properties [12]. Additionally, its performance is less sensitive to temperature, it exhibits a lower density, and it is less expensive than Terfenol–D (raw material cost to produce Galfenol is about \$0.08/g compared to \$0.50/g for producing Terfenol–D [13]). The cost for this alloy is still high in comparison with other materials. This cost is due to the complexity of the manufacturing process, known as advanced Bridgman process, that involves directional solidification and the machining of the material. Due to its good properties, this is the material that has been selected to conform the initial harvester prototype.
- Magnetostrictive Fe–Co alloys: They are good candidates for sensors, actuators and energy harvesters due to their low cost and abundance. In addition to this, iron–cobalt alloys present better mechanical properties than Terfenol–D and Galfenol, as a result of their higher tensile strength and larger ductility [1]. However, a lower magnetostriction coefficient is found for these alloys.

A general comparison of these alloys is shown in Figure 2.9 and Table 2.2.



**Figure 2.9:** Absolute magnetostrictive coefficients of different materials [1].

**Table 2.2:** Material properties of Fe–Co alloys, Terfenol–D and Galfenol [1].

		Fe–Co alloys	Terfenol–D	Galfenol
Magnetostrictive	Magnetostriction (ppm)	Max > 140 80–140	Max 3000 800–1200	Max 300 120–240
Magnetic	Coercivity (A/m)	< 200	300	3000
	Saturation flux density (T)	2.0 <	1.0	1.5
	Relative permeability	100	< 10	< 100
Mechanical	Tensile strength (MPa)	600 <	30	400
	Elongation (%)	< 30	< 1	1 <
	Young’s modulus (GPa)	200	< 100	< 100
Thermal	Coefficient of thermal expansion ( $10^{-6} \text{ K}^{-1}$ )	11.9	12	11
	Curie temperature ( $^{\circ}\text{C}$ )	900	380	680
Electrical	Volume resistivity ( $\mu\Omega \cdot \text{cm}$ )	10	58	85
Density ( $\text{g} \cdot \text{cm}^{-3}$ )		8.4	9.25	7.8

### 2.3.4. Electromagnetic Coupling

The final stage in the electric energy generation is the conversion of magnetic energy of the active material under Faraday’s law principles. As it has been explained, the stresses generated in the harvester structure due to mechanical vibrations will produce changes in the bulk magnetization of the magnetostrictive material and thus the magnetic flux density in the material will change with time.

The time-varying magnetic flux density variation generates a voltage difference (electromotive force, emf) that can be collected with a coil according to:

$$\varepsilon_{ind} = -N_c A_c \frac{\partial B}{\partial t} \quad (2.2)$$

where  $\varepsilon_{ind}$  is the induced electromotive force (emf),  $N_c$  is the number of turns of the coil,  $A_c$  is the coil’s cross section and  $B$  is the modulus of the magnetic flux density vector,  $\mathbf{B}$ . In Equation 2.2 an homogeneous magnetic field parallel to the coil is assumed. In order to obtain a higher emf, it is possible to increase the number of turns. Nevertheless, as mentioned before, the bulkiness of this pick-up coil is one of the disadvantages of this type of harvester.

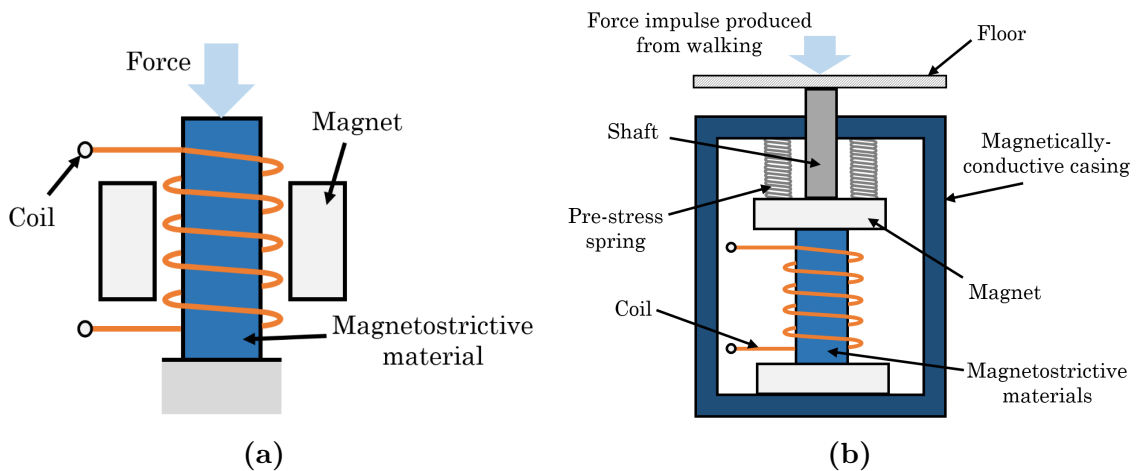


### 2.3.5. Harvester Configuration Examples

Attending to literature, a magnetostrictive vibration harvester is generally composed of a mechanical vibrating body (frame), a magnetostrictive material body, a pick-up coil and permanent magnets. Depending on their disposition in the assembly, two main types of magnetostrictive harvester configurations can be found: axial and bending, according to the stress state of the active material.

#### 2.3.5.1. Axial Type Harvesters

This type of energy harvesters are characterized by the presence of axial stresses on the magnetostrictive material. One of the main applications of axial type magnetostrictive energy harvesters is obtaining energy from impacts, as the configuration designed for collecting energy from human walking [14] (see (b) in Figure 2.10).



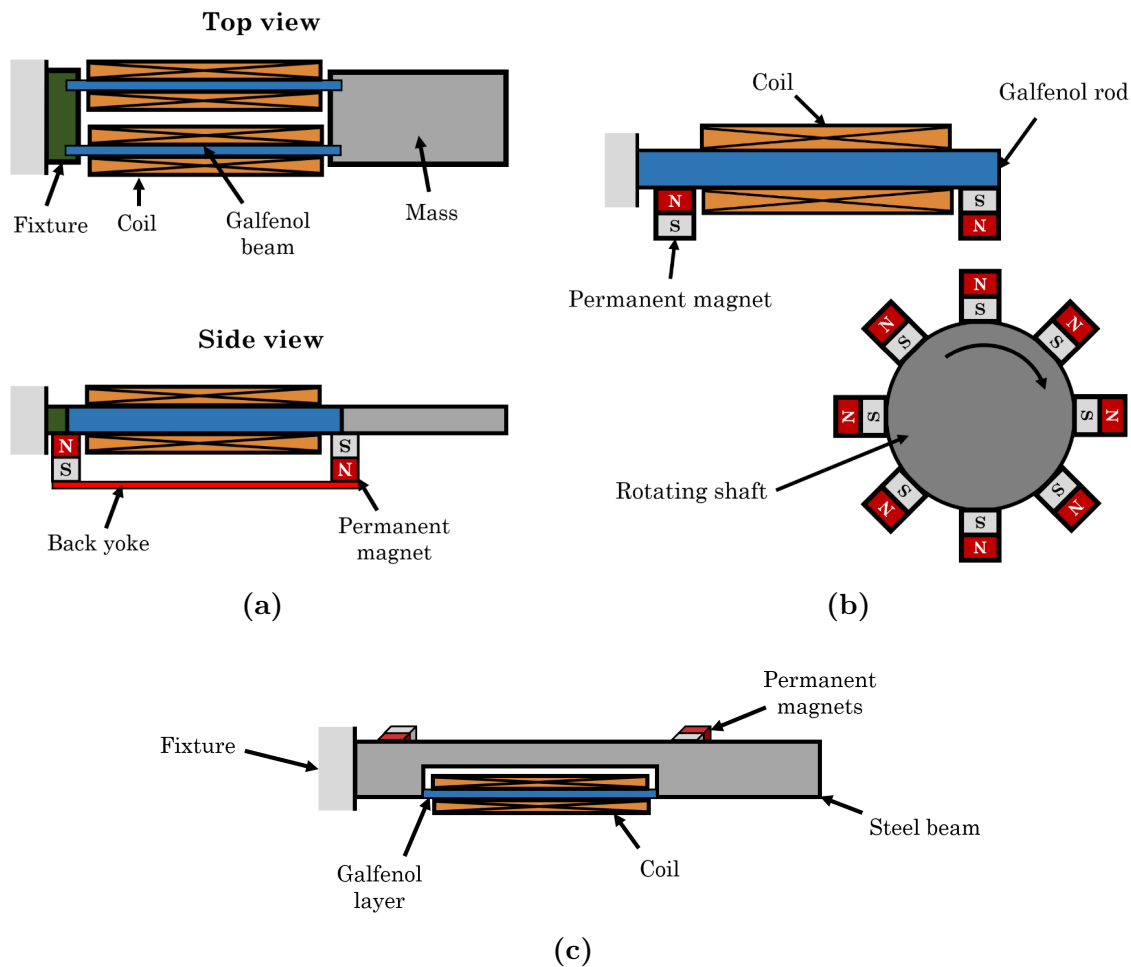
**Figure 2.10:** (a) General axial magnetostrictive energy harvester configuration. (b) Harvester to collect energy from human walking with pre-stress springs to protect the Terfenol-D rod [7, 14].

The main drawbacks of this type of harvesters are the limited frequency bandwidth, the necessity of protection mechanisms (e.g. pre-stress springs) due to the installation of the magnetostrictive material (brittle in many occasions) in the load path, and the large axial force required.

#### 2.3.5.2. Bending Type Harvesters

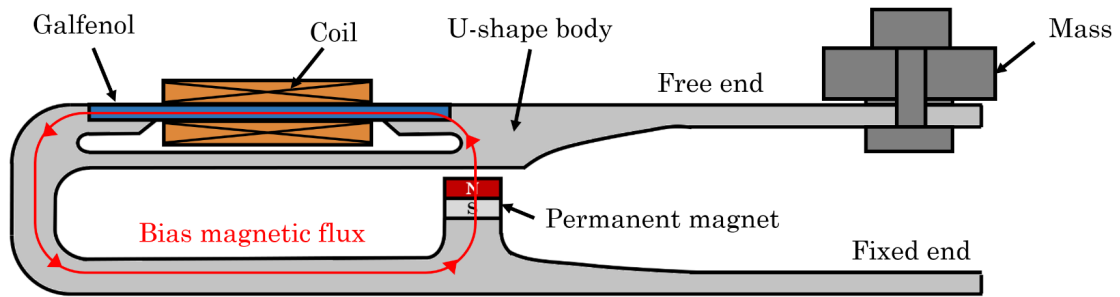
Bending type magnetostrictive energy harvesters have the advantage that they can collect energy from any vibrating surface, contrary to axial type harvesters. They are

based on the vibration of a cantilever structure. Several different configurations have been studied in the literature, and can be resumed in two groups: unimorph beam and bimorph beam harvesters, depending on whether they have one or two magnetostrictive material bodies respectively. Figure 2.11 shows three different examples of bending type harvesters.



**Figure 2.11:** (a) Bimorph magnetostrictive energy harvester [15]. (b, c) Unimorph magnetostrictive energy harvesters [16, 17].

One of the most-employed geometries is the so-called U-shaped (unimorph structure), which can be seen in Figure 2.12. This structure becomes the initial point of the analysis made in this work. It can be seen that the harvester has a permanent magnet to create a magnetic flux that orients the magnetic domains in the longitudinal direction when no stress is present.

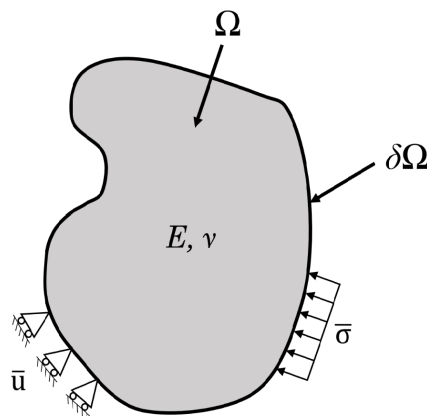


**Figure 2.12:** U-shaped unimorph magnetostrictive vibration energy harvester [18].

## 2.4. Structural Analysis

In order to design an optimum magnetostrictive harvester, numerical mechanical simulations will be carried out. These simulations will be based on a linear elastic model for the harvester. The numerical problem will be solved by FEM (Finite Element Method). In the following section the fundamentals of Linear Elasticity Theory are explained since these concepts will be required for the mechanical simulation of the magnetostrictive energy harvester structure. A general mathematical formulation of the theory will be made and then it will be studied both in the static and the dynamic cases.

The Linear Elasticity Theory models how solids deform and the stresses they suffer due to external loads. The two main assumptions of this model are: small deformations and linear relationship between stress and strain components. This is why this model is not valid if yielding is produced. This theory is included in the Theory of Elasticity which belongs to the discipline of Solid Mechanics.



**Figure 2.13:** Diagram for the elastic model.

The problem intended to be solved is the elastic problem, which is defined by the geometry, the material mechanical properties and the actions. The geometry is defined by domains ( $\Omega$ ) and boundaries ( $\delta\Omega$ ); the material mechanical properties mainly are: the Young modulus ( $E$ ) and the Poisson ratio ( $\nu$ ); and the actions can be of two different types: volume forces (vector  $\mathbf{X}$ ) and boundary conditions (either supports,  $\bar{u}$ , or boundary actions,  $\bar{\sigma}$ ). The condition of fixation is known as Dirichlet boundary condition ( $\bar{u} = 0$ ). A diagram of the defined elastic model is shown in Figure 2.13.

### 2.4.1. General Formulation of the Linear Elasticity Model

In this section, the general mathematical formulation of the linear elasticity model is presented. In the subsequent equations, Einstein notation will be used (also known as index notation). The elastic problem can be solved from three different expressions: the strain-displacement equations (expression 2.3a), the motion equations (second Newton's law, expression 2.3b) and the constitutive equations (Hooke's generalized law, expression 2.3c) [19].

$$\varepsilon_{ij} = \frac{1}{2}(u_{i,j} + u_{j,i}) \quad (2.3a)$$

$$\sigma_{ij,j} + X_i = \rho\ddot{u}_i \quad (2.3b)$$

$$\sigma_{ij} = K_{ijkl}\varepsilon_{kl} \quad (2.3c)$$

In expressions 2.3a, 2.3b and 2.3c,  $\boldsymbol{\varepsilon}$  is the strain tensor,  $\mathbf{u}$  the displacement vector,  $\boldsymbol{\sigma}$  the stress tensor,  $\mathbf{X}$  the volume forces vector,  $\rho$  the density,  $\ddot{\mathbf{u}}$  the acceleration vector and  $\mathbf{K}$  is the stiffness tensor of the material. If the material is considered to be homogeneous (properties are the same in all the points of the material) and isotropic (the material behaves the same along every direction); the stiffness tensor just depends on two independent parameters: the Young Modulus  $E$ , and the Poisson ratio  $\nu$ . Usually two other parameters are used for simplifying the expressions, known as Lamé parameters:  $\lambda$  and  $G$ ; which can be calculated with equations 2.4a and 2.4b [19].

$$\lambda = \frac{E\nu}{(1+\nu)(1-2\nu)} \quad (2.4a)$$

$$G = \frac{E}{2(1+\nu)} \quad (2.4b)$$

With this new parameters Equation 2.3c becomes Equation 2.5 in matrix notation [19].

$$\begin{pmatrix} \sigma_x \\ \sigma_y \\ \sigma_z \\ \tau_{xy} \\ \tau_{xz} \\ \tau_{yz} \end{pmatrix} = \begin{bmatrix} \lambda + 2G & \lambda & \lambda & 0 & 0 & 0 \\ \lambda & \lambda + 2G & \lambda & 0 & 0 & 0 \\ \lambda & \lambda & \lambda + 2G & 0 & 0 & 0 \\ 0 & 0 & 0 & 2G & 0 & 0 \\ 0 & 0 & 0 & 0 & 2G & 0 \\ 0 & 0 & 0 & 0 & 0 & 2G \end{bmatrix} \begin{pmatrix} \varepsilon_x \\ \varepsilon_y \\ \varepsilon_z \\ \varepsilon_{xy} \\ \varepsilon_{xz} \\ \varepsilon_{yz} \end{pmatrix} \quad (2.5)$$

where duplicated off-diagonal elements have been omitted due to the symmetry of the strain and stress tensors. Equation 2.3a can also be rewritten in matrix notation as:

$$\begin{pmatrix} \varepsilon_x \\ \varepsilon_y \\ \varepsilon_z \\ \varepsilon_{xy} \\ \varepsilon_{xz} \\ \varepsilon_{yz} \end{pmatrix} = \begin{bmatrix} 1 & 0 & 0 & 0 & 0 & 0 & 0 & 0 & 0 \\ 0 & 0 & 0 & 0 & 1 & 0 & 0 & 0 & 0 \\ 0 & 0 & 0 & 0 & 0 & 0 & 0 & 0 & 1 \\ 0 & \frac{1}{2} & 0 & \frac{1}{2} & 0 & 0 & 0 & 0 & 0 \\ 0 & 0 & \frac{1}{2} & 0 & 0 & 0 & \frac{1}{2} & 0 & 0 \\ 0 & 0 & 0 & 0 & 0 & \frac{1}{2} & 0 & \frac{1}{2} & 0 \end{bmatrix} \begin{pmatrix} u_{x,x} \\ u_{x,y} \\ u_{x,z} \\ u_{y,x} \\ u_{y,y} \\ u_{y,z} \\ u_{z,x} \\ u_{z,y} \\ u_{z,z} \end{pmatrix} \quad (2.6)$$

Combining this with Equation 2.5 the stresses can be determined as a function of the derivatives of the displacements by using a  $6 \times 9$  matrix called  $\mathbf{c}$  as shown in Equation 2.7.

$$\begin{pmatrix} \sigma_x \\ \sigma_y \\ \sigma_z \\ \tau_{xy} \\ \tau_{xz} \\ \tau_{yz} \end{pmatrix} = \begin{bmatrix} \lambda + 2G & 0 & 0 & 0 & \lambda & 0 & 0 & 0 & \lambda \\ \lambda & 0 & 0 & 0 & \lambda + 2G & 0 & 0 & 0 & \lambda \\ \lambda & 0 & 0 & 0 & \lambda & 0 & 0 & 0 & \lambda + 2G \\ 0 & G & 0 & G & 0 & 0 & 0 & 0 & 0 \\ 0 & 0 & G & 0 & 0 & 0 & G & 0 & 0 \\ 0 & 0 & 0 & 0 & 0 & G & 0 & G & 0 \end{bmatrix} \begin{pmatrix} u_{x,x} \\ u_{x,y} \\ u_{x,z} \\ u_{y,x} \\ u_{y,y} \\ u_{y,z} \\ u_{z,x} \\ u_{z,y} \\ u_{z,z} \end{pmatrix} \quad (2.7)$$

### 2.4.2. Elastostatics

Elastostatics is the application of linear elasticity to static cases, where the body is under equilibrium, and accelerations are null ( $\ddot{\mathbf{u}} = 0$ ). This way Equation 2.3b turns into [19]:

$$\sigma_{ij,j} + X_i = 0 \Leftrightarrow \nabla \cdot \boldsymbol{\sigma} + \mathbf{X} = \nabla \cdot (\mathbf{c}\nabla\mathbf{u}) + \mathbf{X} = \mathbf{0} \quad (2.8)$$

Where the components that conform the stress tensor  $\boldsymbol{\sigma}$  are calculated from the product of the previously defined matrix  $\mathbf{c}$  and  $\nabla\mathbf{u}$ , defined as the 9-component column vector constituted by the derivatives of the displacement vector components, as shown in Equation 2.7.

### 2.4.3. Elastodynamics

Elastodynamics involves time-dependence on the equations of linear elasticity. This way, in this case  $\ddot{\mathbf{u}} \neq 0$  and Equation 2.3b is written as [19]:

$$\sigma_{ij,j}(t) + X_i(t) = \rho\ddot{u}_i(t) \Leftrightarrow \nabla \cdot (\mathbf{c}\nabla\mathbf{u}(t)) + \mathbf{X}(t) = \rho\ddot{\mathbf{u}}(t) \quad (2.9)$$

This equation can be applied to a body that is moving in harmonic motion. In this case, the system is considered to be oscillating at a unique frequency  $f$ . The angular frequency corresponding to  $f$  is  $\omega = 2\pi f$ . If the motion is considered to be harmonic, then the system's points will show oscillatory displacements, that is,  $\mathbf{u}(t) = \mathbf{u}_0 \cos(\omega t)$ . By taking the second derivative of this expression with respect to time it can be obtained:

$$\ddot{\mathbf{u}}(t) = -\mathbf{u}_0 \omega^2 \cos(\omega t) \quad (2.10)$$

where  $\mathbf{u}_0$  is the displacement amplitude. Equation 2.10 can be solved by substituting each of the time-dependent variables with their corresponding amplitudes, as shown in Equation 2.11.

$$\nabla \cdot (\mathbf{c}\nabla\mathbf{u}_0) + \mathbf{X}_0 = \rho\omega^2\mathbf{u}_0 \quad (2.11)$$

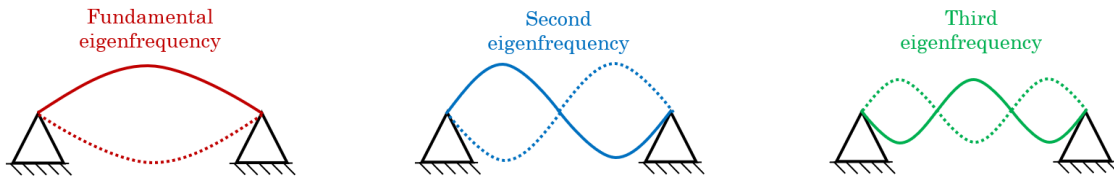
#### 2.4.3.1. Mechanical Resonance and Eigenfrequency Analysis

Resonance is a phenomenon consisting on the amplitude increase of the oscillations of a dynamic system when an input (or a Fourier component of this input) is periodically applied at a frequency equal or close to the resonant frequencies of the system. That is, an input applied at a frequency equal to or close to the natural frequency of a system will produce much larger amplitude oscillations than the same input applied at non-resonant frequencies. This phenomenon is observed in many different fields

---

in which waves are involved. Some examples are electromagnetic resonance, acoustic resonance (of special interest in music) or mechanical resonance.

Resonance frequencies are also known as natural frequencies or eigenfrequencies. Each resonance frequency has its corresponding mode of vibration (eigenmode) with its corresponding displacement amplitudes. For example, the three first eigenmodes of a system consisting of a string tied at its two ends are shown in Figure 2.14.



**Figure 2.14:** Different modes of vibration of a string tied at its two ends.

Natural frequencies are strongly related to the mass and the stiffness of the system, and are independent of the body load. They are also called eigenfrequencies because their calculation is an eigenvalue problem. There will be as many eigenvalues as degrees of freedom. However, in general just the first few modes of vibration are relevant in practical applications.

For a vibrating system the calculation of the natural frequencies and their corresponding modes of vibration is resumed to the following eigenvalue problem:

$$\nabla \cdot (\mathbf{c} \nabla \mathbf{u}_0) = \rho \lambda_n \mathbf{u}_0 \quad (2.12)$$

where  $\lambda_n = \omega_n^2$  and  $\mathbf{c}$  is the matrix defined in Equation 2.7. Then, the natural frequencies  $\omega_n$  are related with the eigenvalues  $\lambda_n$  by  $\omega_n = \sqrt{\lambda_n}$  and the corresponding displacements of the vibration modes are the eigenvectors  $\mathbf{u}_0$ .

It must be remarked that in Equation 2.12,  $\mathbf{u}_0$  will just indicate the modes of vibration of the system; but not the actual amplitude of the oscillations. In order to calculate the amplitude of these oscillations, Equation 2.11 should be solved, taking into account the external excitation,  $\mathbf{X} = \mathbf{X}_0 \cos(\omega t)$ .

### 2.4.3.2. Damping

Damping is defined as an influence within an oscillatory system that prevents it from oscillating. It can be produced by different processes depending on the physical system. In the case of the vibrational magnetic structure, damping will be produced by friction within the mechanical system. Damping can be linearly modeled with the Rayleigh

viscous damping model, which enables to calculate the damping matrix  $\mathbf{C}$  (introduced in the mechanical system equation multiplying the velocity of the displacement) as a function of two parameters, known as Rayleigh parameters,  $\alpha$  and  $\beta$  as shown in Equation 2.13, where  $\mathbf{M}$  and  $\mathbf{K}$  are the mass and the stiffness matrices respectively.

$$\mathbf{C} = \alpha\mathbf{M} + \beta\mathbf{K} \quad (2.13)$$

This damping will lower the resonance peak with respect to when no damping is present since it otherwise would tend to infinity. Rayleigh parameters must be determined empirically from the measurement of the resonance of the structure since they depend on the geometry and the stress amplitude among other factors.

---



# Chapter 3

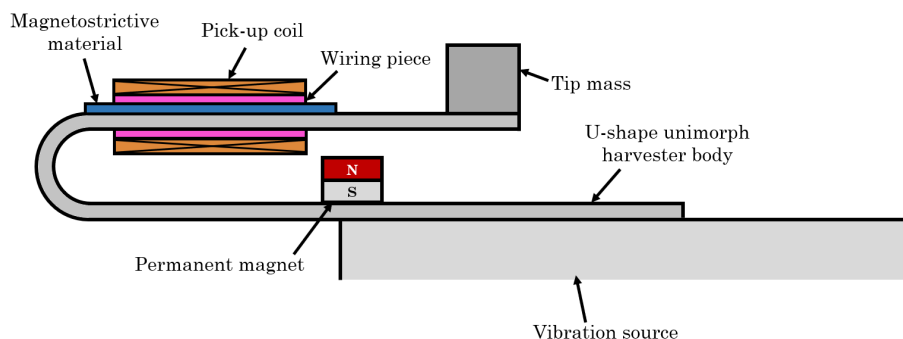
## Harvester Design and Simulation

In this chapter, the initial design of the harvester prototype is described as well as the steps taken to perform the mechanical simulations.

### 3.1. Initial Design

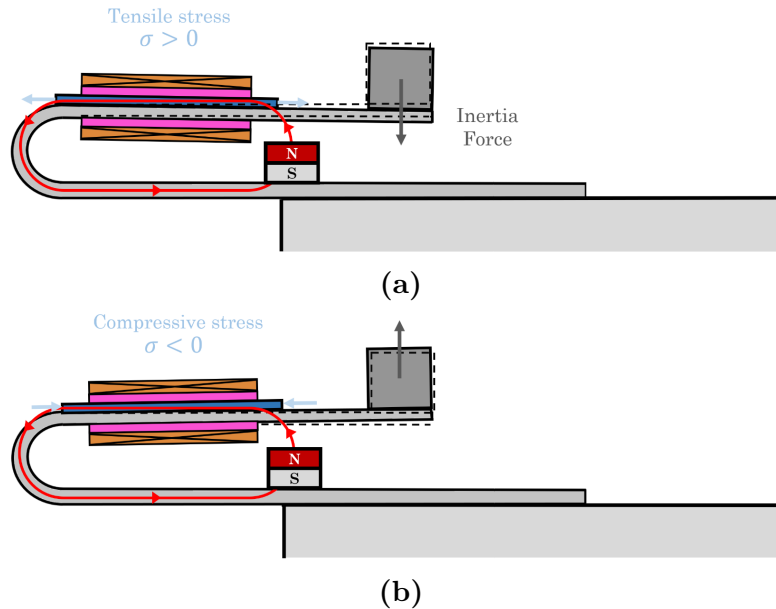
As it was explained in Section 2.3.5, among the different existent harvester configurations, bending type harvesters are those which enable to obtain energy from any vibrating surface. In particular U-shaped unimorph magnetostrictive vibration energy harvesters are those showing the greatest power output and further research is needed to improve their performance. For these reasons, this is the configuration selected to study. There are several U-shaped harvesters, with more or less complex geometries.

The objective at long term would be to design a highly efficient harvester that can be applied to many different applications and that can be produced in mass with a high performance and low cost. In order to make the manufacturing process less expensive and enable mass production while maintaining high performance, the configuration proposed by Ueno in [20] is chosen to be the best alternative (see Figure 3.1).



**Figure 3.1:** U-shape magnetostrictive harvester configuration proposed by Ueno [20].

This harvester configuration is composed by a simple-geometry body, which can be manufactured with a low cost by bending a metal sheet. Additionally, in [20] this geometry is demonstrated to have good resistance to fatigue.



**Figure 3.2:** (a) U-shape harvester with magnetostrictive material under tensile stresses. (b) U-shape harvester with magnetostrictive material under compressive stresses (harvester proposed by Ueno in [20]).

Figure 3.2 helps to explain the behavior of the initial harvester design. The permanent magnet creates a bias magnetic flux (indicated in red in the figure) which is necessary to maintain the magnetostrictive material sheet saturated. The location of the magnetostrictive material enables to produce uniform stresses in its longitudinal direction, either tensile or compressive. The magnetic saturation of the magnetostrictive material avoids the magnetic flux backflow when vibrations are produced. Thanks to the Villari effect, the stresses on the magnetostrictive material will alternately change the magnetic flux seen by the pick-up coil, generating an electromotive force.

So, the whole system behaves as a magnetic circuit which is formed by the harvester body, the magnetostrictive material, the gap and the magnet. Since the gap size will vary with the vibrations, this is another source of magnetic flux variation, and thus contributes to the electromotive force generated in the coil. The tip mass is the additional element which is added in the upper edge of the U-shaped body to tune its frequency of resonance. By increasing the tip mass the stresses that the material experiments can be augmented.

The size of the initial design of the harvester will be of 5 cm with 2 cm of magnetostrictive material. These are rough dimensions to start with the design and are based

upon the broadening of future applications, since reduced size is associated with portability and comfort as indicated in Section 2.1. The final dimensions of the components are shown in the technical drawings of Appendix A.

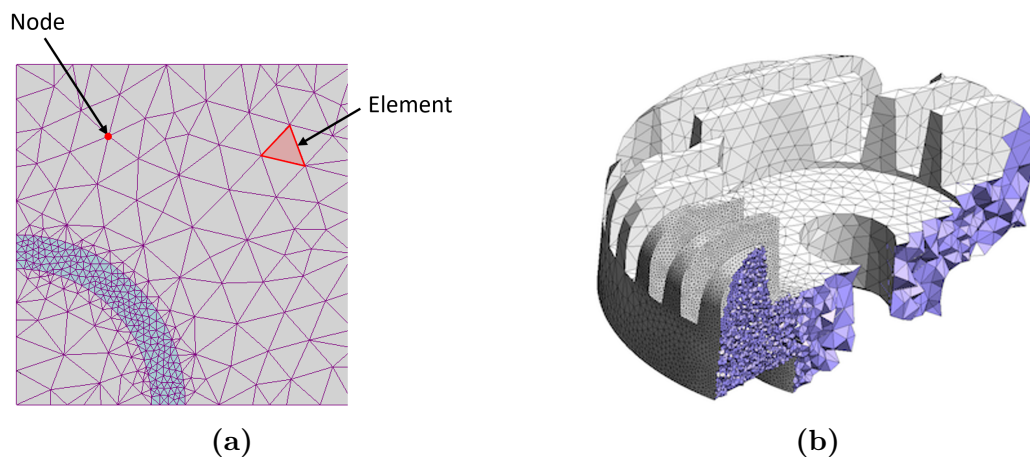
The objective is to maximize the stresses generated in the magnetostrictive material (greater induced electromotive force) and to obtain the first or main resonance frequency around 100 Hz. To reach this aim an extensive analysis of the magnetic vibrating structure of the harvester must be performed. In the present work, mechanical numerical simulations are done in order to validate the design from the calculation of the resonance frequency, the stresses and the displacements.

## 3.2. Mechanical Simulations

In the following section the concepts that will be used to perform the mechanical numerical simulations are explained in detail and the implementation of the simulations is explained.

### 3.2.1. Finite Element Method

FEM is a numerical method that is used for solving PDEs in two and three space variables. It consists on dividing the continuum system into a finite number of elements, which are simpler and smaller. This discretization is made by constructing a mesh, which has a finite number of nodes. These nodes define the elements into which the system has been discretized. Triangles are commonly used for discretizing 2D geometries, while tetrahedrons are used for 3D geometries, as shown in Figure 3.3.



**Figure 3.3:** (a) 2D FEM example [21]. (b) 3D FEM example [22].

Material properties are constant on each element and the problem to be solved consists of a linear system of equations with  $n$  unknowns, being  $n$  the number of nodes of the problem. It is in these nodes where the desired solutions are calculated (in the case of this work, the displacements and the stresses).

### 3.2.2. Software Used in the Simulations

In order to do the mechanical simulation of the harvester design different software programs will be used for modeling the 3D geometry, as well as for its adequate meshing and for solving the PDE (Partial Differential Equation) problem.

#### 3.2.2.1. SolidWorks®

SolidWorks® is a CAD software for mechanic modeling in 2D and 3D developed by SolidWorks Corp., affiliated to Dassault Systèmes. The program enables to define pieces and assemblies, as well as to draw technical plans easily. In the present work a license SOLIDWORKS Student Design Kit has been used because it is free and it provides with all the necessary tools for the geometry definition.

#### 3.2.2.2. MATLAB®

MATLAB® is a high-level language which integrates computation, visualization and programming in an interactive environment (<https://es.mathworks.com/products/matlab.html>). It can be used to solve many different problems, especially the ones related with matrices and vectors. It is typically used for the development of algorithms, simulations, data analysis, or graphics. Additionally, the program includes specific families of tools, named toolboxes; which are designed to particular technology applications and extend the MATLAB® environment capabilities.

This is the program that will be used to simulate mechanically the harvester, using the *Partial Differential Equation Toolbox*, which provides functions for solving structural mechanics, heat transfer, and general PDEs by using FEM. The Total Academic Headcount license of MATLAB® provided by UPNA has been employed in this work.

In addition, with MATLAB® new codes can be developed in order to perform new simulations. For example, magnetic and electromagnetic FEM simulations can be implemented in order to calculate the emf induced in the coil of the harvester. However, this work is limited to mechanical simulations.

---

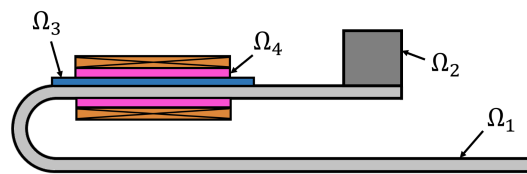
### 3.2.2.3. Gmsh<sup>®</sup>

Gmsh<sup>®</sup> is an open source three-dimensional finite element mesh generator with built-in processing facilities (<https://gmsh.info/>). Meshing, or mesh generation, is a process that consists on dividing the continuum space into discrete elements. This division is made by generating a 2D or 3D grid, which discretizes the geometry. Meshing is a key process in FEM, since the fields (in this case deformation and stresses) are defined in the nodes of each element. The more elements the mesh has, the more accurate the results of the numerical simulation will be, but the more resources and time the computation will require. That is why Gmsh<sup>®</sup> has been used for obtaining the most appropriate mesh for the simulations to be accurate and fast.

MATLAB<sup>®</sup> tools for making a particularized meshing for the geometry are quite limited, since there are just a few parameters that can be edited: mesh growth rate (related with the growth of the elements when they are further from the geometry edges) and maximum and minimum mesh edge length (define the limits of the size of the elements of the mesh to make it finer or coarser). Gmsh<sup>®</sup> however provides a wide number of tools to make an efficient meshing.

### 3.2.3. Geometry Definition

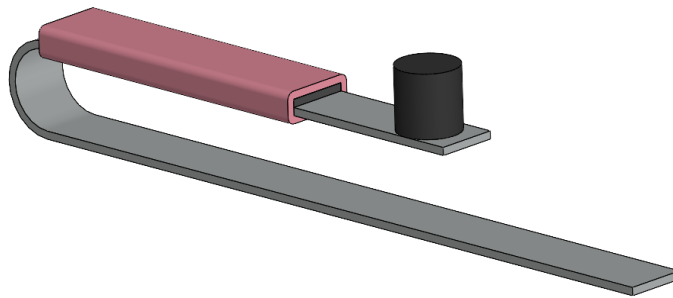
First of all, the geometry of the harvester must be defined. It must be remarked that this geometry is formed not by one single body, but by four different ones; also called domains or cells: the harvester main body, the magnetostrictive material, the tip mass and the piece supporting the pick-up coil (used to facilitate the removal of the wiring from the prototype in future tests), as indicated in Figure 3.4. A different PDE has to be defined in each domain because each one has its own density, Young Modulus and Poisson coefficient.



**Figure 3.4:** Harvester domains identification.

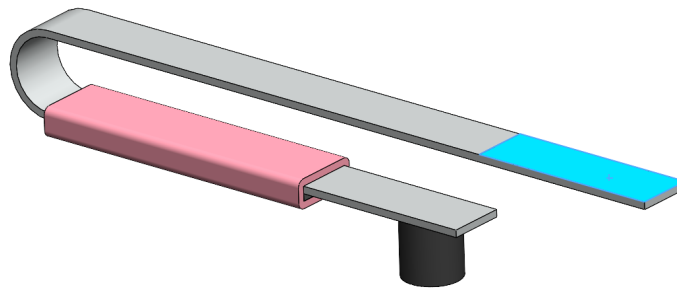
The complete geometry is composed of four different domains. However, in this work the mechanical simulation is done with just two domains,  $\Omega_1$  and  $\Omega_2$  in Figure 3.4, as an initial approximation, since the objective is the design of the vibrating structure. Though the simulations have not been performed for the complete four-domain geometry; it has been indicated how the two-domain simulations should be modified in order to obtain the complete geometry static and dynamic results. The simulation involving just the U-shaped body and the tip mass is thus a simplification of the complete four-domain geometry.

Figure 3.5 shows the complete geometry defined with no assigned domain to the pick-up coil itself since it will not be considered in the simulations. In any case, the pick-up coil would further reduce the resonance frequency since an extra mass is added to the upper part of the U-shaped body. This way, results are adequate to validate the design despite not taking the pick-up coil into account.



**Figure 3.5:** U-shape magnetostrictive vibration energy harvester geometry created with SolidWorks®.

As it can be seen in Figure 3.1 one part of the lower end of the U-shape harvester is fixed to the vibration source, but not the whole lower face. When defining the fixed boundary conditions of the PDE problem, the face in which they will be applied must be given. Therefore, in order to differentiate between the fixed and the free part in the lower face; the fixed part has been extruded 0.01 mm (see Figure 3.6). The geometry file will be saved as a .STEP file in order to be read properly by the mesh generator software Gmsh®.



**Figure 3.6:** Detail on the geometry of the fixed end of the harvester (marked in blue).

### 3.2.4. Meshing of the Harvester Geometry

As it has been previously commented, mesh generation is very important for obtaining accurate results as fast as possible using the minimum resources. Codes 3.1 and 3.2 show and explain the code required for obtaining the desired mesh on each

domain for the two studied geometries. It is mandatory for each domain to have mesh elements that do not interfere with the ones of the rest of the domains. The domains of interest where stresses are relevant are the magnetostrictive sheet (these stresses will be the ones defining the magnetic field variation) and the harvester main body. This way, these two domains should have a fine mesh, while the tip mass domain can have a coarser mesh to make the simulation faster. The size of the elements of the mesh of each domain is defined with the characteristic length. In the case of the geometry with just two domains, the mesh code is shown in Code 3.1.

Code 3.1: Gmsh<sup>®</sup> Domain Assignment and Meshing Parameters for the two-domain geometry

```

1 // Forces Gmsh to use OpenCascade instead of the native engine
2 SetFactory("OpenCASCADE");
3
4 // Load the body without interferences between the different volumes.
5 v() = ShapeFromFile("Harvester.step");
6 BooleanFragments{ Volume{v()}; Delete; }{}
7 // Here it is defined a characteristic length for the meshing of each of the
8 // volumes. For example for Volume 1 the characteristic length is defined to
9 // be 0.2 mm.
10 Characteristic Length{ PointsOf{Volume{1}}; } = 0.2;
11 Characteristic Length{ PointsOf{Volume{2}}; } = 0.5;
12
13 // Finally the physical groups are exported (necessary to be treated by MATLAB
14 // as domains). In general: Physical Volume(X) = {Y1,Y2,...}; where Y are the
15 // numbers that Gmsh assigns to each volume (can be seen with
16 // Tools/Options/Geometry/Visibility: Volume Label ON); and X is the number
17 // wanted to be considered by MATLAB for that domain.
18
19 // To the volume that Gmsh calls 1 it is assigned domain 1.
20 Physical Volume(1) = {1}; // U-shaped main body
21 Physical Volume(2) = {2}; // Tip mass

```

In the case of the four-domain geometry, Code 3.1 is modified so that the characteristic length definition and volume assignment is done for the four involved domains, as shown in Code 3.2.

Code 3.2: Gmsh<sup>®</sup> Domain Assignment and Meshing Parameters for the four-domain geometry

```

1 // Forces Gmsh to use OpenCascade instead of the native engine
2 SetFactory("OpenCASCADE");
3
4 // Load the body without interferences between the different volumes.
5 v() = ShapeFromFile("Harvester.step");
6 BooleanFragments{ Volume{v()}; Delete; }{}
7 // Here it is defined a characteristic length for the meshing of each of the
8 // volumes.
9 Characteristic Length{ PointsOf{Volume{1}; Volume{3}; Volume{4}}; } = 0.2;
10 Characteristic Length{ PointsOf{Volume{2}}; } = 0.5;
11

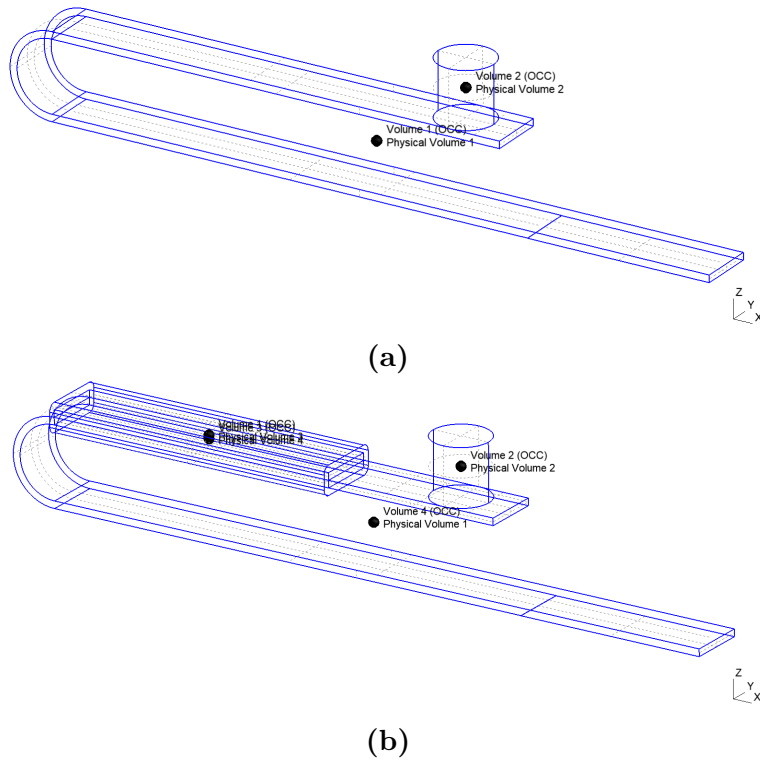
```

```

12 // Finally, physical groups are exported.
13 Physical Volume(3) = {1}; // Magnetostrictive material
14 Physical Volume(2) = {2}; // Tip mass
15 Physical Volume(4) = {3}; // Wiring piece
16 Physical Volume(1) = {4}; // U-shaped main body

```

In order for MATLAB<sup>®</sup> to consider the exported geometry as different domains, these must be defined as “physical volumes” in Gmsh<sup>®</sup>. The association between the volumes (defined automatically by the mesh generation program) and the physical volumes (volumes considered by MATLAB<sup>®</sup>) can be seen in Figure 3.7 for both studied geometries.

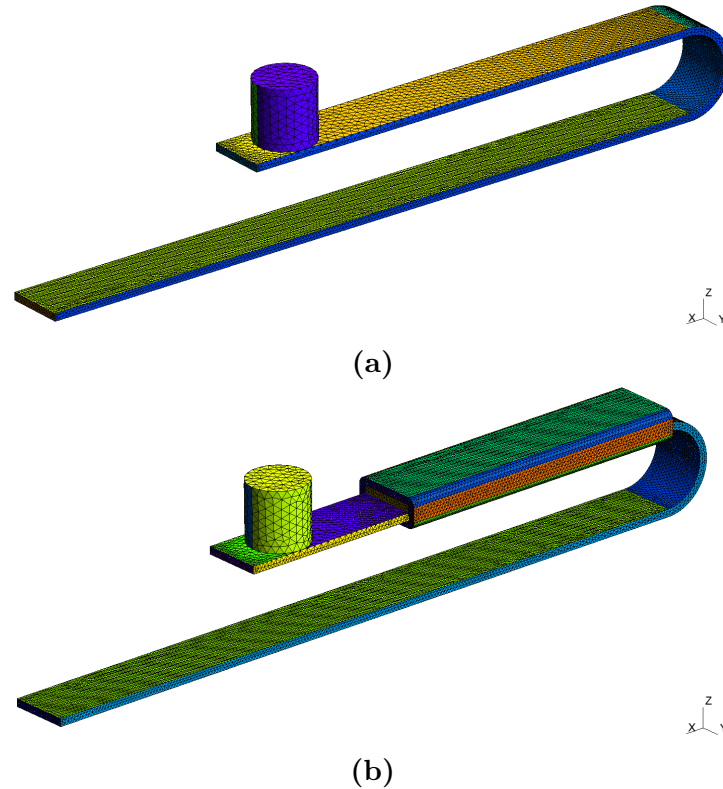


**Figure 3.7:** (a) Volumes and physical volumes for the two-domain geometry. (b) Volumes and physical volumes for the four-domain geometry.

By loading the .geo files (codes 3.1 and 3.2) in Gmsh<sup>®</sup> all the physical volumes and meshing parameters are defined. Thereafter, the “Mesh” module can be used to generate a 3D tetrahedral element mesh on the geometry, obtaining the results shown in Figure 3.8. The nodes and elements data is exported to MATLAB<sup>®</sup> as a .m file. The achieved meshing has bigger elements in the tip mass, which is the domain with the lower interest for the numerical simulations, while the U-shaped main body and the magnetostrictive sheet have a fine mesh. It is considered to be a good trade-off between

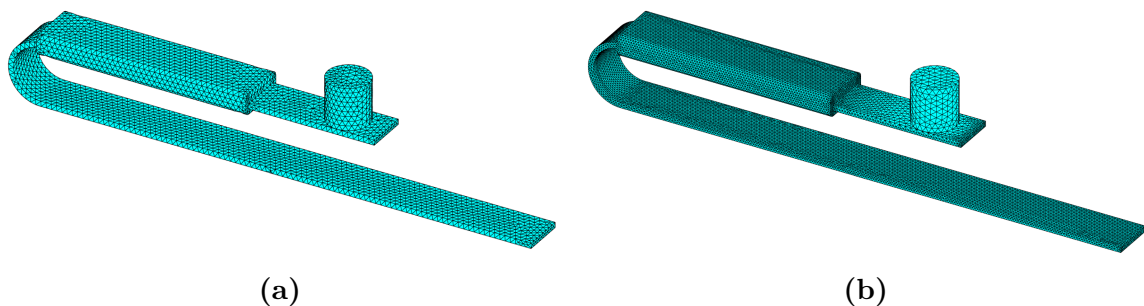


the simulations accuracy and the employed time and resources, since by making the meshing finer, the computer might run out of RAM memory during the computation.



**Figure 3.8:** (a) Mesh generated for the two-domain geometry. (b) Mesh generated for the four-domain geometry.

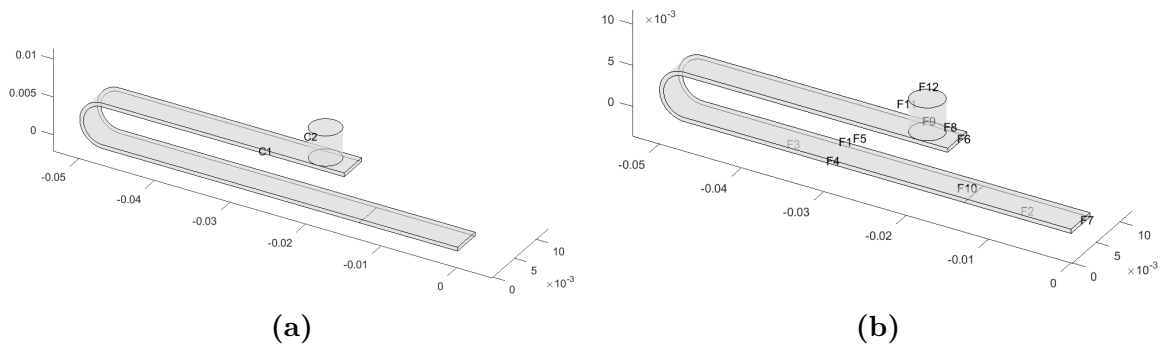
The MATLAB<sup>®</sup> scripts are shown and explained in Appendix C. In Code C.3 it has been included the option to use the MATLAB<sup>®</sup> meshing in case it is desired. Figure 3.9 compares the meshes generated by MATLAB<sup>®</sup> and Gmsh<sup>©</sup> for the four-domain geometry.



**Figure 3.9:** (a) Mesh generated by MATLAB<sup>®</sup>. (b) Mesh generated by Gmsh<sup>©</sup>.

### 3.2.5. PDE Problem Definition

The PDE problem definition is exposed for the initial simulation of the two-domain geometry that will enable to validate the U-shaped body design. Code C.1 creates a PDE model and loads the nodes and elements from Gmsh (`Gmsh_mesh_data.m` file) to create the geometry. In order to check if domains have been exported correctly and the face numbering needed for defining the boundary conditions, Figure 3.10 is shown.



**Figure 3.10:** (a) Harvester volume domain identification (dimensions in m). (b) Harvester face identification (dimensions in m).

Code C.2 shows the definition of the material coefficients for each domain and the definition of the boundary condition. The properties for the materials conforming each of the domains are summarized in Table 3.1 [23, 24, 25].

**Table 3.1:** Materials mechanical properties [23, 24, 25].

	Gray cast iron	Ferrite	Galfenol	PLA
$\rho$ (kg/m <sup>3</sup> )	7200	7870	7800	1240
$E$ (GPa)	110	200	59	3.5
$\nu$	0.28	0.291	0.44	0.36

The tip mass is a parameter that will enable to tune the resonance frequency of the prototype. It is desired that this parameter can be modified in an easy way in the simulations, without the need to change the tip mass volume. Therefore, a fictitious density is calculated for the tip mass as the ratio of the tip mass,  $m$ , and the volume  $V$  of the elements conforming the domain of the tip mass (domain 2 in (a) Figure 3.10), by using the function `calc_vol_average.m` given in Code C.11. The value for the gravity acceleration,  $g$ , is considered to be 9.81 m/s<sup>2</sup>. The  $\mathbf{c}$  matrices are calculated for each material using the function `elasticityC3D.m` included in the *Partial Differential Equation Toolbox*. Equations 3.1a and 3.1b show the form of the PDE problems and PDE eigenvalue problems respectively that MATLAB<sup>®</sup> is able to solve.

$$m \frac{\partial^2 \mathbf{u}}{\partial t^2} + d \frac{\partial \mathbf{u}}{\partial t} - \nabla \cdot (\mathbf{c} \nabla \mathbf{u}) + a \mathbf{u} = \mathbf{f} \quad (3.1a)$$

$$-\nabla \cdot (\mathbf{c} \nabla \mathbf{u}) + a \mathbf{u} = \lambda m \mathbf{u} \quad (3.1b)$$

Comparing equations 3.1a and 3.1b with equations 2.8, 2.11 and 2.12 on Section 2.4, the coefficients  $a$  and  $d$  are null, whereas  $m$  corresponds to the mass density and  $\mathbf{c}$  to the matrix defined in Equation 2.7. In Equation 3.1b,  $\lambda$  corresponds to the eigenvalues of the problem, or  $\omega_n^2$  by comparison with Equation 2.12. Coefficients  $m$ ,  $d$ ,  $\mathbf{c}$ ,  $a$  and  $\mathbf{f}$  can be defined at each domain with function `specifyCoefficients.m` as shown in Code C.2 (the coefficients specified in this code correspond to the ones needed to calculate the resonance frequencies, as it can be noticed by comparing Equations 2.12 and 3.1b).

There is a fixed boundary condition in the face attached to the vibration source. This is a support boundary condition ( $\bar{u}$ ) of Dirichlet type, since the solution values of the displacement vector  $\mathbf{u}$  are specified to be null. The fixed face can be seen in Figure 3.10 to be face F2. This Dirichlet condition is imposed with the function `applyBoundaryCondition.m` as shown in Code C.2.

### 3.2.6. Resonance Frequencies and Modes of Vibration

The resonance frequencies and modes of vibration are calculated in order to check if the initial design is optimal, that is, the main eigenfrequency is close to 100 Hz. In Code C.4 the natural frequencies are calculated as the square roots of the eigenvalues since, as it was explained in Section 2.4.3.1,  $\omega_n^2 = \lambda$ . The frequencies corresponding to the first six modes of vibration corresponding to the U-shaped harvester vibrant magnetic structure and a tip mass of 0.4781 g (mass of the ferrite magnet that has been used in the experimental part explained in Chapter 4), are displayed in Table 3.2.

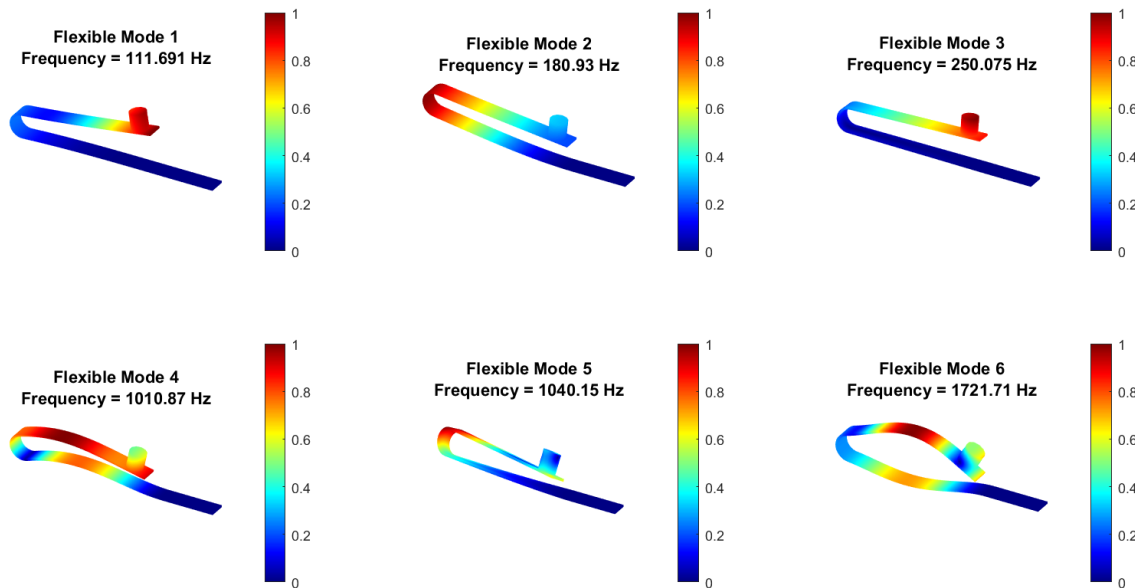
**Table 3.2:** Frequencies of resonance corresponding to first six modes of vibration.

Mode of vibration	Frequency (Hz)
1	<b>111.69</b>
2	180.93
3	250.07
4	1010.9
5	1040.1
6	1721.7

Code C.5 creates an animation of the first six modes of vibration of the harvester to see the shapes and how the harvester deforms in each vibration mode. For this purpose, function `animateHarvester.m` (see Code C.10) has been used to calculate each of the frames of the animation. This function basically creates an animation whose frames correspond to the deformation of the nodes at each time. The color scale indicates the deformation modulus normalized with respect to the maximum one for each mode of vibration, as indicated in Equation 3.2.

$$\text{Normalized deformation modulus} = \frac{\sqrt{u_x^2 + u_y^2 + u_z^2}}{\sqrt{u_x^2 + u_y^2 + u_z^2_{max}}} \quad (3.2)$$

This magnitude has been scaled in order for it to be perceptible in the graph. To accelerate the computation process, a coarser mesh than the one employed in the other simulations has been used. This can be done due to the fact in this case the analysis is qualitative and not quantitative, so accuracy is not as important. Figure 3.11 shows a single frame of the animation of the harvester modes of vibration.



**Figure 3.11:** Frame of the animation of the harvester modes of vibration.

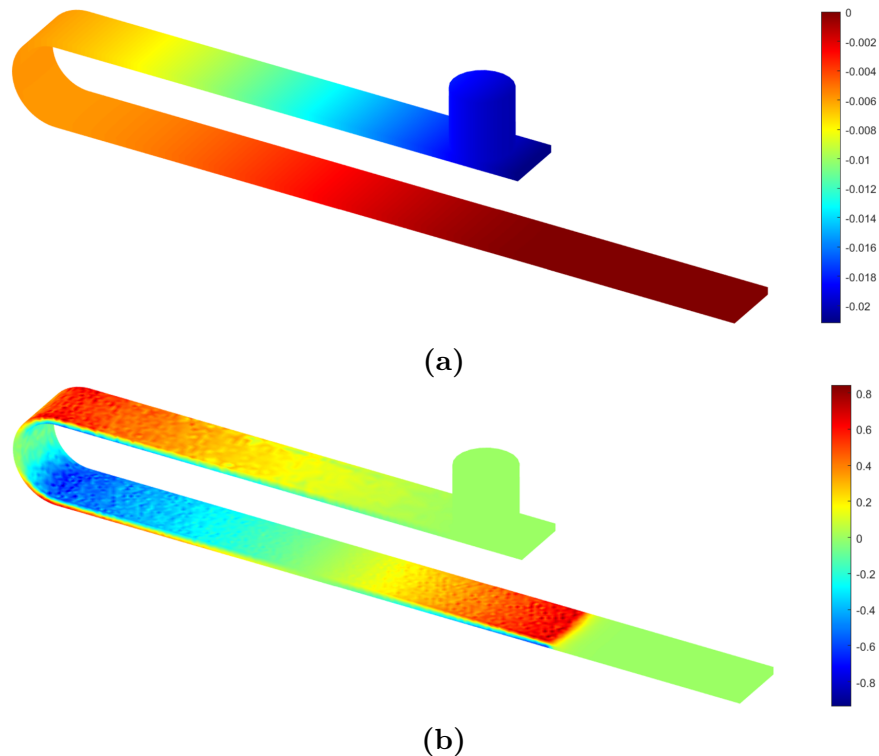
For the considered design, the natural frequency corresponding to the first mode of vibration is in the desired range, close to 100 Hz. The justification for considering this design optimal is its low manufacturing cost, its simplicity and that it is resonant in the range of frequencies where most of the industrial processes take place as explained in Section 2.2. The fact that the frequency is higher than 100 Hz is not an issue because after including the additional elements of the future harvester, the resonance

frequency will lower since mass would be added to the upper part of the U-shaped body. Numerical simulations will determine if the displacements and the stresses are adequate for the future harvester.

### 3.2.7. Static Simulation (Gravity Load)

In order to simulate the static case, that is, the harvester being subjected just to gravity acceleration, Code C.6 is implemented. In this case, the vector coefficient  $\mathbf{f}$  is defined by comparing Equations 2.8 and 3.1b as the product of density and gravity. There is a different volume forces vector for each of the domains, since each of them has a different density. The vector coefficient  $\mathbf{f}$  has a single negative component in the  $z$  direction.

Afterwards, stresses are calculated by using the function `evaluateCGradient.m` from the previously calculated displacement vectors,  $\mathbf{u}$ . However,  $\sigma_{xx}$  is the component of interest, since it is the one coupled with the magnetic flux into the magnetostrictive material. Figure 3.12 shows the displacement in the  $z$  direction in millimeters and  $\sigma_{xx}$  stresses in MPa under static loading.



**Figure 3.12:** (a) Displacement in  $z$  direction (mm) under static loading for the two-domain geometry. (b)  $\sigma_{xx}$  (MPa) under static loading for the two-domain geometry.

It can be observed that the obtained displacements are valid for the static case (deformation by gravity) since they will produce the upper part to go down a negligible length in comparison with the harvester structure dimensions (a few hundredths of millimeter). Therefore, there is no risk that the upper U-shaped main body part enters in contact with the lower part since they are separated by 5 mm.

With respect to the stresses, it is observed that the maximum  $\sigma_{xx}$  is produced in the area close to the bent part of the U-shaped structure. This means that in order to optimize the future harvester and maximize the stresses transmitted to the active or magnetostrictive material, and thus the power output of the device, the active material sheet should be located close to the bent part of the U-shaped body.

### 3.2.8. Dynamic Simulation (Harmonic Load)

For the dynamic simulation (see Code C.8), an oscillatory acceleration will be generated by the vibration source. Since the lower part of the U-shaped main body is fixed to an oscillatory acceleration source, the component will be moving in a non-inertial system with an oscillatory inertial force. This inertial force will be a vector whose only component different from zero will be the  $z$  component. This  $z$  component will have an amplitude given by the product of the density and the acceleration of the vibration source (in this case it will be considered to be  $10 \text{ m/s}^2$  because it is the typical value for industrial machinery vibrations [9]). Therefore, in Code C.8 it is defined the inertial force amplitude vector for each of the domains and the frequency at which the source is vibrating (the resonance frequency of the first mode close to 100 Hz, since it is the frequency for which the vibrating structure has been designed to obtain an optimal performance).

In the case of the dynamic simulation, the damping phenomenon must be taken into account, since if it did not exist, the displacements and stresses would tend to infinity as the system approached the resonance frequency. This damping effect does not affect the resonance frequencies and modes of vibration and the results of the static simulation. However, they do affect the dynamic simulation results. As it was exposed in Section 2.4.3.2, Rayleigh coefficients should be determined empirically and then introduced into the simulation to calculate the displacements and the stresses. This has been made in Code C.7, by comparing the results obtained in the laboratory with the ones of the simulation to determine the parameters that provide the best fitting between both results. These parameters that have been determined are mainly the two Rayleigh damping coefficients,  $\alpha$  and  $\beta$ . In addition, the Young Modulus of the U-shaped main body,  $E$ , has been slightly modified from the initial supposed value from [23]. Chapter 5 presents the results since empirical data is needed for taking into account the damping phenomenon.

---

---

In Code C.8 it can be seen how the coefficients have been specified by comparing Equations 2.11 and 3.1b in an analogous way to what it was done in Section 3.2.5.

In the case of the four-domain geometry not simulated in this work, the stresses occurring in the magnetostrictive material sheet are determinant for the future magnetostrictive harvester performance. Thus, in Appendix B it has been included an explanation on the two factors that would determine the optimal magnetostrictive material to be included in the future magnetostrictive harvester: the average Galfenol stresses under vibration and its magnetization change with vibration stresses depending on the applied manufacturing annealing stress.





## Chapter 4

# Harvester Vibrating Magnetic Structure Characterization

In the present chapter, the physical construction of the magnetic vibrating structure modeled in the simulations is developed. Besides, the different devices and the methodology followed for its resonance frequency and amplitude of vibration characterization are described.

### 4.1. U-shaped Main Body Characterization

After the geometry definition described in the previous chapter (see the technical drawing in Appendix A), the vibrating magnetic structure was characterized (U-shaped main body) by the experimental determination of the frequency of resonance and the amplitude of vibration.

The U-shaped main body of the harvester has been manufactured by GRUPO IAM from a 100% gray iron sheet provided by Hierros Landaben. This U-shaped main body is made of iron because a ferromagnetic material is needed in order to close the magnetic circuit generated by the bias magnet as it was explained in Section 3.1.

A total of 10 equal pieces were manufactured from a 0.5 mm in thickness iron plate by cutting it with a Water Jet Cutting (WJC) machine in a rectangular shape of dimensions  $88.5 \times 4$  mm. Then the pieces were bent with an external radius of 3 mm according to Plan 1.01 in Appendix A to get the desired shape by using a bending tool. The optimal simulation results of frequency and displacements were obtained for a U-shaped body with a short side length of 32 mm and a long side length of 47 mm, similar to the dimensions proposed by Ueno in [20].

Figure 4.1 shows a picture of the U-shaped iron main body taken in the laboratory. During the performance of the experiments, it was observed that this component was susceptible to pitting corrosion due to ambient moisture (noticeable in the figure).



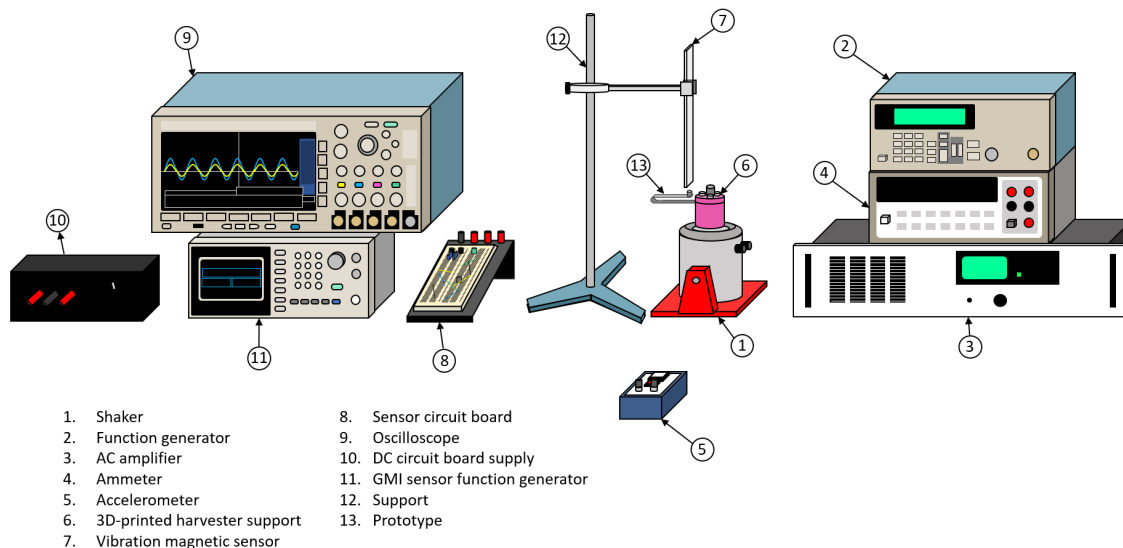
**Figure 4.1:** U-shaped iron main body.

## 4.2. Laboratory Material

In the following section, it is exposed the different equipment that has been employed to characterize the prototype. Two main aspects have been addressed:

- Generation of the ambient vibrations.
- Characterization of the U-shaped body vibration: frequency of resonance and amplitude of vibration determination.

In order to clarify the disposal of the elements conforming the laboratory experiment, a numerated diagram is shown in Figure 4.2. The different wire connections between the laboratory equipment have not been represented for clarity reasons but will be described in the corresponding subsections and are resumed in Figure 4.3.



**Figure 4.2:** Laboratory setup.

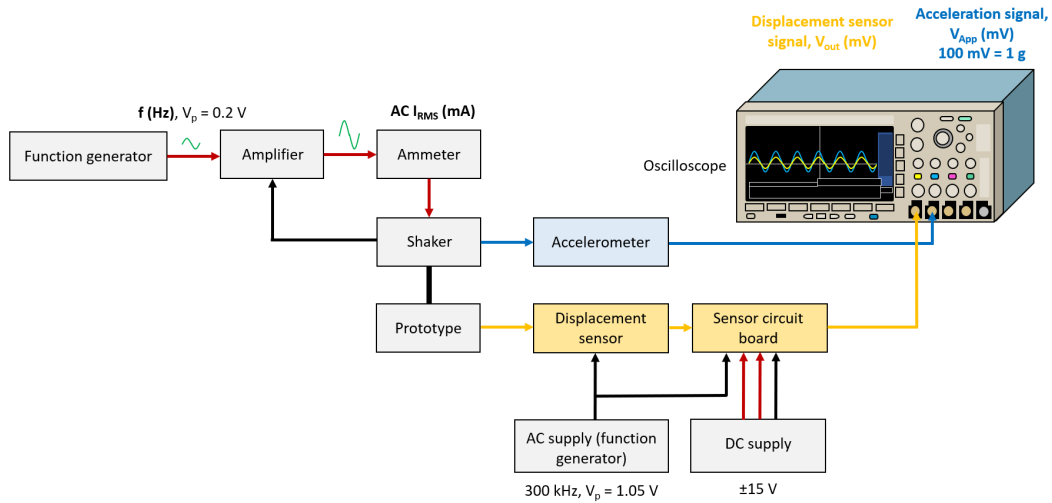


Figure 4.3: Laboratory setup connections.

### 4.2.1. Generation of Ambient Vibration

In this subsection the laboratory equipment used for generating the ambient vibration is described: shaker, function generator, amplifier, ammeter, accelerometer and 3D-printed support.

#### 4.2.1.1. Shaker

This device (LDS<sup>®</sup> V201 from Brüel & Kjær) simulates the vibration source, and its mission is to transmit the mechanical ambient vibrations to the U-shaped body under the assumption of a simple harmonic oscillation motion of peak amplitude  $Y_0$ . This shaker is designed for fatigue and resonance testing, modal and structural analyses, and vibration screening of small components over a wide frequency range, from 5 to 13000 Hz. Figure 4.4 shows the shaker model used in the experimental setup.

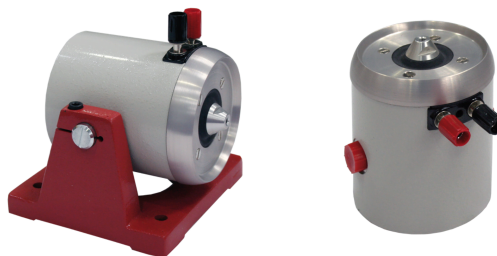


Figure 4.4: LDS<sup>®</sup> V201 permanent magnet shaker.

#### 4.2.1.2. Function Generator

This device (AFG310 SONY Tektronix Arbitrary Function Generator) generates the alternating current (AC) signal that powers and controls the movement of the shaker. A sinusoidal signal is chosen, leading to the already mentioned simple harmonic motion of the harvester structure. This device permits to easily select the frequency of vibration. Nonetheless, this instrument has no power enough to feed the shaker, so an AC amplifier is required. Figure 4.5 shows function generator model used in the experimental setup.



**Figure 4.5:** AFG310 SONY Tektronix Arbitrary Function Generator.

#### 4.2.1.3. AC Amplifier

This amplifier (LDS<sup>®</sup> LPA100 from Brüel & Kjær) enables to provide with the sufficient power to the shaker. The amplification can be modified with this device thanks to a rotating button. The screen of the device shows the voltage amplitude as well as the AC current Root Mean Square (RMS) value, but with poor accuracy. That is why an ammeter is connected in series before the connection to the shaker. The connection of the amplifier to the ammeter and to the ground of the shaker is made thanks to a coaxial cable. Figure 4.6 shows the amplifier model used in the experimental setup.



**Figure 4.6:** LDS<sup>®</sup> LPA100 linear power amplifier.

---

#### 4.2.1.4. Ammeter

In order to measure with accuracy the AC RMS current,  $I_{RMS}$ , that is being supplied to the shaker, a 34401A Agilent multimeter is employed. The ammeter will be connected in series between the amplifier and the shaker. Figure 4.7 shows the ammeter model used in the experimental setup.

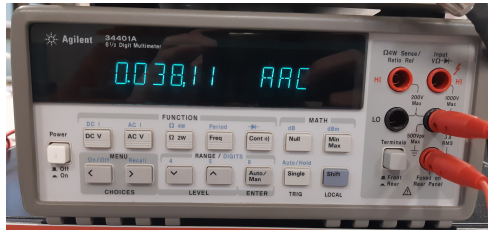


Figure 4.7: 34401A Agilent multimeter.

#### 4.2.1.5. Accelerometer

The device (TLD352C33 from PCB Piezotronics) is an ICP<sup>®</sup> piezoelectric sensor used to measure the acceleration of the shaker during vibration. The output is an AC peak-to-peak voltage signal,  $V_{App}$  (mV), measured with an oscilloscope (explained in Section 4.2.2.3). This voltage signal can be translated into a conventional peak acceleration,  $A_0$  ( $m/s^2$ ), with the conversion factor supplied by the manufacturer, 100 mV (peak-to-peak) = 9.81  $m/s^2$  by the expression  $A_0(m/s^2) = V_{App}(mV) \cdot \frac{1}{2} \cdot \frac{9.81(m/s^2)}{100(mV)}$  (halved to obtain the peak value). Figure 4.4 shows the accelerometer used in the experimental setup.

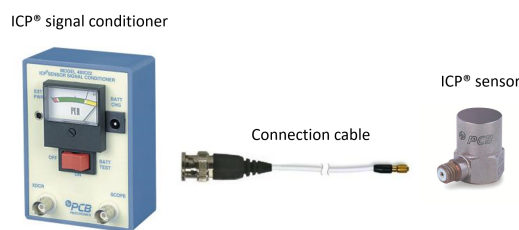


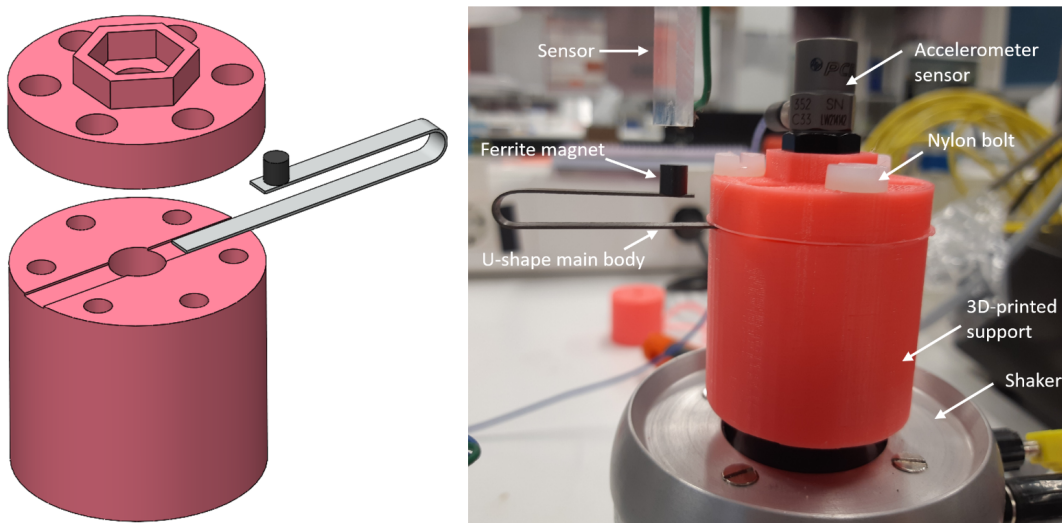
Figure 4.8: ICP<sup>®</sup> sensor and 480C02 ICP<sup>®</sup> signal conditioner.

#### 4.2.1.6. 3D-printed Harvester Support

Since the U-shaped body can not be directly fixed to the shaker, a homemade support is designed. This component also permits to fix the accelerometer probe on its

top, so that the acceleration during harvester vibration can be properly measured. The technical drawings of the designed support can be seen in the Appendix A in Plans 2.00, 2.01 and 2.02.

The support is comprised of two different pieces of polylactic acid composite (PLA) printed with a 3D printer (BQ Witbox 2). The lower piece is threaded to the shaker by a conical hole. This piece counts with a thin groove (0.4 mm in depth). The upper piece counts with a similar groove so the U-shaped body can be inserted in between. Finally, the two pieces are fixed by three plastic nylon bolts. Figure 4.9 shows some details of the SolidWorks® design of the upper and lower parts as well as an the result of the assembly after the 3D-printing.



**Figure 4.9:** 3D-printed support details.

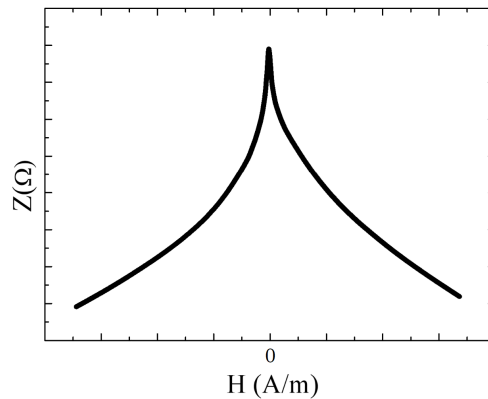
## 4.2.2. Characterization of U-shaped Body Vibration

To characterize the amplitude of vibration of the U-shaped body, a Giant Magnetoimpedance (GMI) based magnetic sensor is employed. In this section, the principle of operation of the sensor and the rest of the devices used for the vibration characterization are introduced.

### 4.2.2.1. Vibration Magnetic Sensor

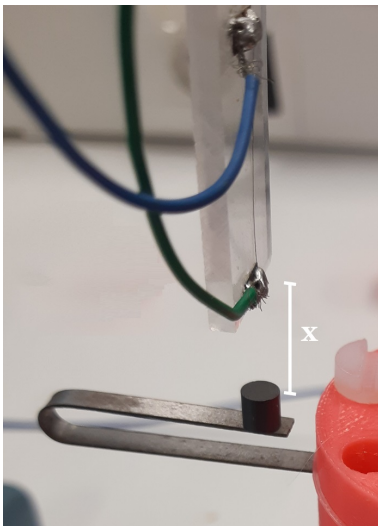
The sensor developed for the amplitude of vibration characterization is based on the Giant Magnetoimpedance (GMI) effect. This effect consists on huge changes in the high-frequency electric impedance of a soft magnetic conductor under the action of an

external magnetic field [26]. A typical curve of impedance versus external magnetic field is shown in Figure 4.10 [26]. As it can be observed, the larger the magnetic field is, the lower the impedance will be; observing a maximum at zero external magnetic field.



**Figure 4.10:** Electric impedance versus external magnetic field [26].

As the sensor nucleus, an amorphous wire obtained by in-rotating water quenching technique was used. The wire, with nominal composition  $\text{Co}_{66}\text{Fe}_{12}\text{Si}_{13}\text{B}_{15}\text{Cr}_4$  (3 cm in length and mean diameter of  $90\ \mu\text{m}$ ), was excited under conditions that optimize its GMI effect,  $f = 300\ \text{kHz}$ ,  $I_{pp} = 15\ \text{mA}$ . The wire is fixed to a methacrylate piece in order to ease its handling, as it can be seen in Figure 4.11. This methacrylate piece is sustained over the harvester tip magnet with the aid of a support that enables to regulate the distance between the ferrite magnet and the wire.



**Figure 4.11:** Displacement sensor.

To characterize the amplitude of the vibrations, a cylindrical ferrite magnet (mass of  $0.4781\ \text{g}$ , diameter of  $4\ \text{mm}$  and height of  $4\ \text{mm}$ ) is attached to the U-shaped vibrating body. The variations in the relative position,  $x$  (see Figure 4.11), of the magnet with respect to the sensor, lead to different magnetic fields acting on the sensor and to the corresponding proportional changes in the impedance of the sensor, permitting the U-shaped body amplitude of oscillation determination,  $X_0$ . This motion can be approximated to a simple harmonic motion as:

$$x(t) = X_0 \cos(\omega t + \phi) \quad (4.1)$$

Where  $X_0$  is the peak amplitude at any moment of the U vibrating body and  $\omega = 2\pi f$  is the angular frequency and  $\phi$  the initial phase of the oscillation. The acceleration of the vibration of the U-shaped body can be easily obtained from the position variation, leading to Equation 4.2:

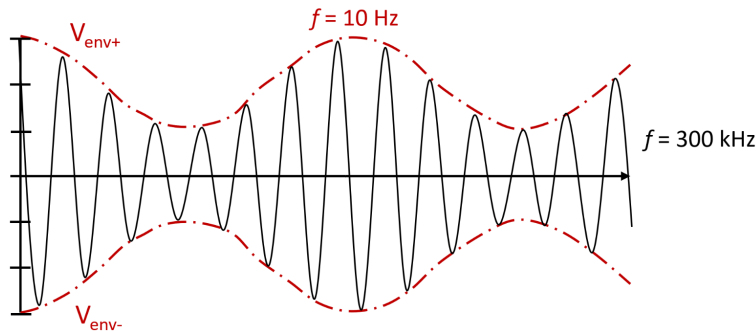
$$a(t) = -X_0 \omega^2 \cos(\omega t + \phi) \quad (4.2)$$

Far from the resonance both the shaker and the U-shaped body oscillate under the same acceleration and so the same amplitude  $Y_0 = X_0$ . This circumstance can be employed for the estimation of  $X_0$  when the vibration of both systems is simultaneously measured. Consequently, the correlation between  $X_0$  and the experimental acceleration  $A_0$  ( $\text{m/s}^2$ ), obtained from the measurements of  $V_{App}$  (mV) with the accelerometer, can be estimated from Equation 4.3.

$$X_0 = Y_0 = \left| \frac{-A_0}{\omega^2} \right| \quad (4.3)$$

#### 4.2.2.2. Sensor Circuit Board

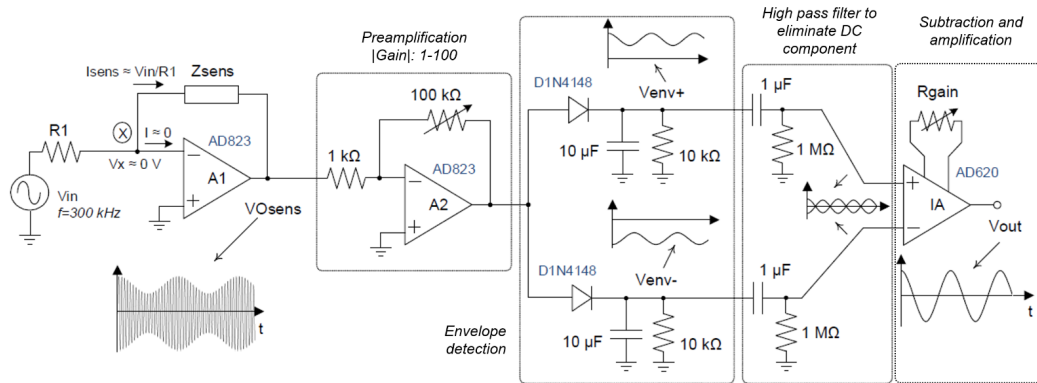
As a result of the vibration, the periodic changes in the sensor impedance lead to an AM (Amplitude Modulation) modulated signal (see Figure 4.12) that must be deconvoluted in such a way that its amplitude,  $V_{env+}$  and/or  $V_{env-}$  is proportional to  $x$ . The minimum on  $V_{env+}$  or  $V_{env-}$  represents the moment in which the distance between the magnet and the sensor is minimum, while the maximum of the same signal will represent the maximum distance. For this purpose, a homemade electronic interface was used [26].



**Figure 4.12:** Signal deconvolution diagram.

Figure 4.13 shows the schematics of the analog homemade electronic interface. The electronic interface was powered with a  $\pm 15$  V DC power supply.



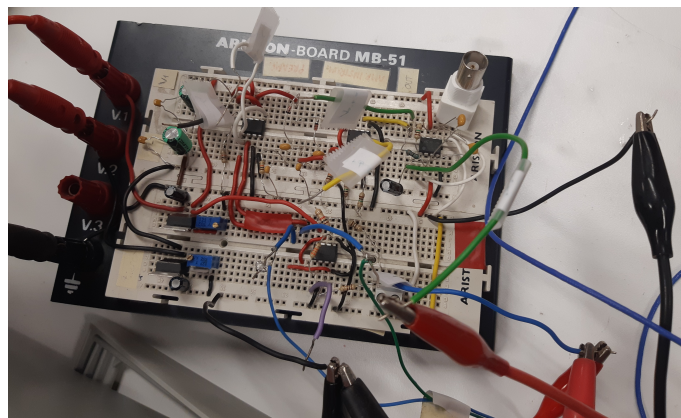


**Figure 4.13:** Analog homemade electronic interface schematic in [26].

Two different stages can be found:

- **Sensor excitement:** It is excited with a 300 kHz sinusoidal signal (function generator Stanford Research Systems DS345,  $V_{in}$ ) in series with a resistor,  $R$ , obtaining a current,  $I_{pp} = \frac{V_{in}}{R}$ . The sensor disposition permits a constant current  $I_{pp}$  to flow through it, independently of its impedance change, thanks to an Operational Amplifier (OA).
- **Demodulation stage:** This stage is beyond the objectives of this work and constitutes a general scheme in the AM demodulation of signals. Initially, an amplification of the sensor signal (see Figure 4.13) is developed. Then, diodes are used to estimate the values of  $V_{env+}$  and  $V_{env-}$ . Subsequently, a high-pass filter eliminates the DC component of enveloping signals, that are finally subtracted and amplified, resulting in the final peak-to-peak output signal,  $V_{out}$ .

Figure 4.14 shows a picture of the analog homemade electronic interface.



**Figure 4.14:** Analog homemade electronic interface in [26].

### 4.2.2.3. Oscilloscope

The oscilloscope employed is the model MDO 3024 (Mixed Domain Oscilloscope) of Tektronix, with a bandwidth of 200 MHz and a sample rate of 5 GS/s, shown in Figure 4.15. The oscilloscope will be used to analyze two signals during the characterization of the resonance frequency of the harvester: the displacement signal coming from the displacement sensor circuit board,  $V_{out}$  (channel 1, in yellow) and the acceleration signal coming from the accelerometer,  $V_{App}$  (channel 2, in blue). In both cases, the associated peak signals can be calculated by halving these output peak-to-peak signal values.



**Figure 4.15:** Tektronix MDO3024 Oscilloscope.

## 4.3. Experimental Measurements

With the described experimental setup, different measurements are made to characterize the vibrant magnetic structure and to validate its use for constructing magnetostrictive harvesters. First of all, the optimal distance, in terms of sensor sensitivity, between the sensor and the vibrating structure was determined. Then, with the help of the accelerometer, the displacement sensor is calibrated permitting the translation of the measured output signal into amplitude of vibration of the U-shaped body. Finally, different frequency analyses are made as the components are added to the harvester to check the simulation results.

### 4.3.1. Determination of the Optimal Tip-Sensor Distance

The initial step is to optimize the sensitivity of the sensor during the detection process. The effect of the distance between the magnet attached to the U-shaped body and the amorphous wire in the sensor response was analyzed in a qualitative way.

---

Under a fixed frequency and amplitude of vibration, the sensor height was varied until the maximum output signal  $V_{out}$  was found. A distance of  $d = 1.35$  cm resulted as the optimum one. This distance was calculated from two direct measurements taken with a height caliper (model H4-30 from Mitutoyo): the distance from the sensor tip to the desk,  $d_{sens} = 17.46$  cm, and the distance from the top of the magnet of the harvester to the desk,  $d_{magnet} = 16.11$  cm. This distance between the sensor and the magnet was not modified along the whole process of experimentation.

### 4.3.2. Calibration of the Displacement Sensor

In second place, the displacement sensor was calibrated. This stage aims to correlate the variations of  $V_{out}$  with the amplitude of oscillation of the vibrating U-shaped structure,  $X_0$ , as explained in Section 4.2.2.1. The frequency was fixed at  $f = 10$  Hz to ensure that no resonance was present and the amplitude of oscillation of the shaker fulfills  $Y_0 = X_0$ . Then, the vibration of the system was simultaneously characterized by the accelerometer and the displacement sensor under increasing values of  $I_{RMS}$  from the amplifier. Accordingly, the peak-to-peak voltage values of the sensor,  $V_{out}$ , and the accelerometer,  $V_{App}$ , signals were registered.

The conversion factor of the accelerometer permits to translate  $V_{App}$  (in mV) into actual peak acceleration,  $A_0$ . This way, the acceleration peak amplitude  $A_0$  that the shaker is transmitting to the U-shaped body can be calculated in  $m/s^2$  for each of the measurements with expression 4.4.

$$A_0 = V_{App} \cdot \frac{9.81}{200} \quad (4.4)$$

**Note:** Peak values are used for direct comparison with simulated data in Chapter 5.

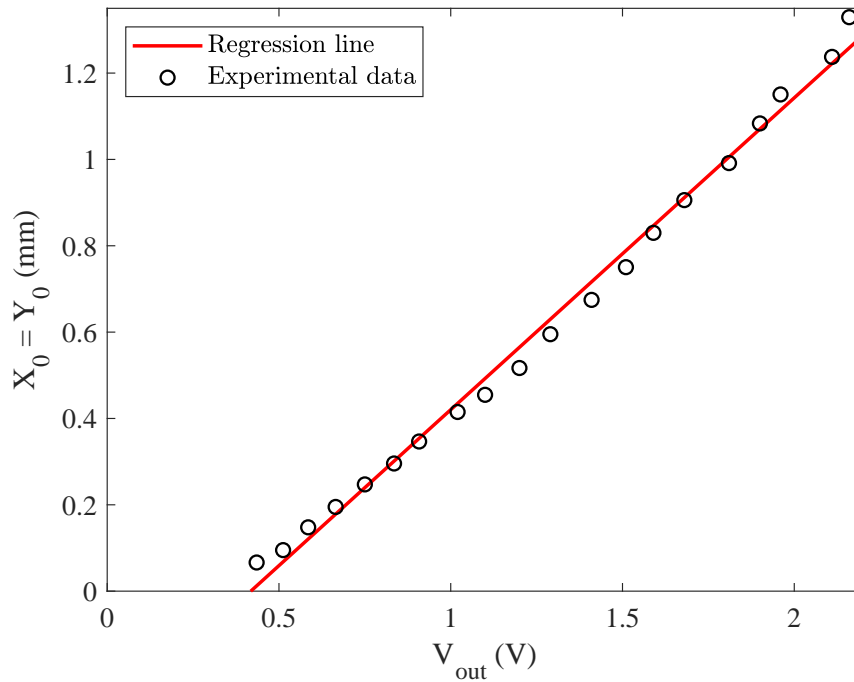
The amplitude of vibration of the shaker and the U-shaped body, can be obtained from expression 4.5.

$$X_0 = Y_0 = \left| -\frac{A_0}{\omega^2} \right| = \left| -\frac{A_0}{(2\pi f)^2} \right| \quad (4.5)$$

This way, by using equation 4.5, since both  $f$  and  $A_0$  are known, the amplitude of oscillation of the U-shaped body can be determined. With these data, the calibration results after plotting the oscillation amplitude  $X_0 = Y_0$  in millimeters versus the sensor output signal amplitude  $V_{out}$  in volts. Laboratory measurements related with the sensor calibration are resumed in Table 4.1, and Figure 4.16 shows the calibration graph.

**Table 4.1:** Calibration of the displacement sensor.

$f$ (Hz)	$I_{RMS}$ (mA)	$V_{out}$ (mV)	$V_{App}$ (mV)	$A_0$ (m/s <sup>2</sup> )	$X_0 = Y_0$ (mm)
20.75		435	5.34	0.2619	0.06635
40.25		512	7.65	0.3752	0.09505
60.41		585	11.9	0.5837	0.1479
79.70		665	15.7	0.7701	0.1951
100.85		750	19.9	0.9761	0.2473
120.65		835	23.8	1.1674	0.2957
139.65		908	27.9	1.3685	0.3466
160.93		1020	33.4	1.6383	0.4150
179.66		1100	36.6	1.7952	0.4547
200.11		1200	41.6	2.0405	0.5169
220.42		1290	47.9	2.3495	0.5951
241.78		1410	54.3	2.6634	0.6747
259.54		1510	60.4	2.9626	0.7504
281.57		1590	66.8	3.2765	0.8300
300.15		1680	72.9	3.5757	0.9058
319.49		1810	79.8	3.9142	0.9915
341.85		1900	87.2	4.2772	1.0834
359.15		1960	92.6	4.5420	1.1505
380.25		2110	99.6	4.8854	1.2375
400.74		2160	107.0	5.2484	1.3294

**Figure 4.16:** Calibration of the displacements sensor.

---

The observed relationship between the two magnitudes is linear, and the best-fit line obtained by using least-squares method is shown in equation 4.6 with a regression coefficient  $R^2 = 0.9932$ .

$$X_0 = 0.7223 V_{out} - 0.3020 \quad (4.6)$$

Equation 4.6 permits to easily translate the displacement sensor output peak-to-peak signal  $V_{out}$  into the oscillation peak amplitude of the U-shaped body,  $X_0$ . This calibration is a general result and can be employed in later experiments for the amplitude of vibration  $X_0$  for any frequency, even at resonance.

It can be appreciated the calibration line does not pass through zero. This offset is due to the presence of the diodes with a knee voltage of 0.7 V in the electronic interface (see Figure 4.13), that make it necessary to surpass a certain vibration value to start obtaining the displacement sensor voltage signal. This is an issue that could be diminished by adjusting the preamplification of the sensor signal so that less oscillation amplitude is necessary to obtain the output signal. Nonetheless, this is out of the scope of this project and will be analyzed in future work.

---



# Chapter 5

## Results and Discussion

The main objective of the work is to determine the frequency of resonance of the U-shaped structure during vibration. Accordingly, the amplitude of the vibrating structure is registered under a constant shaker oscillation amplitude value,  $Y_0$ , for different frequencies of oscillation. This way, the resultant vibrating structure oscillation amplitude,  $X_0$ , can be compared under similar measurement conditions, permitting the determination of the frequency of resonance, since the shaker oscillation is the same for all analyzed frequencies.

In spite of this, different resonance analyses are done in order to know how the addition of the different elements that comprise a vibrational harvester may affect to the frequency of resonance. After the described initial analysis for the U-shaped harvester body with a tip mass constituted by the ferrite magnet, the effect of the addition of the Galfenol sheet and a homemade 3D-printed piece to incorporate the collecting pick-up coil is done. Finally, an additional non-magnetic tip mass is added to check how the value of the frequency of resonance is affected and so, the possibility of tuning it depending on the desired application. For each of these experiments, a table with the collected data is presented, as well as a graph plotting the structure vibration displacement amplitude,  $X_0$ , versus the frequency,  $f$ .

### 5.1. U-shaped Harvester Body

As mentioned, it is relevant to compare  $X_0$  values of the U-shaped body for a constant shaker oscillation amplitude, taken to be  $Y_0 \approx 0.1$  mm. To do that, the value of the experimental parameter,  $V_{App}$  (mV), has to be properly adjusted for each analyzed frequency. This is done by modifying  $I_{RMS}$  with the button of the AC amplifier until  $V_{App}$  reaches the desired value, so that the values of  $Y_0$  are approximately equal for all the frequencies. Equation 5.1, obtained from the combination of expressions 4.4 and 4.5, permits the calculation of  $V_{App}$  in each case.

$$V_{App} = \frac{200}{9.81} \frac{Y_0 (2\pi f)^2}{1000} \quad (5.1)$$

Under this procedure, measurements resumed in Table 5.1 are obtained for frequencies between 40 and 150 Hz.  $X_0$  is calculated from Equation 4.6.

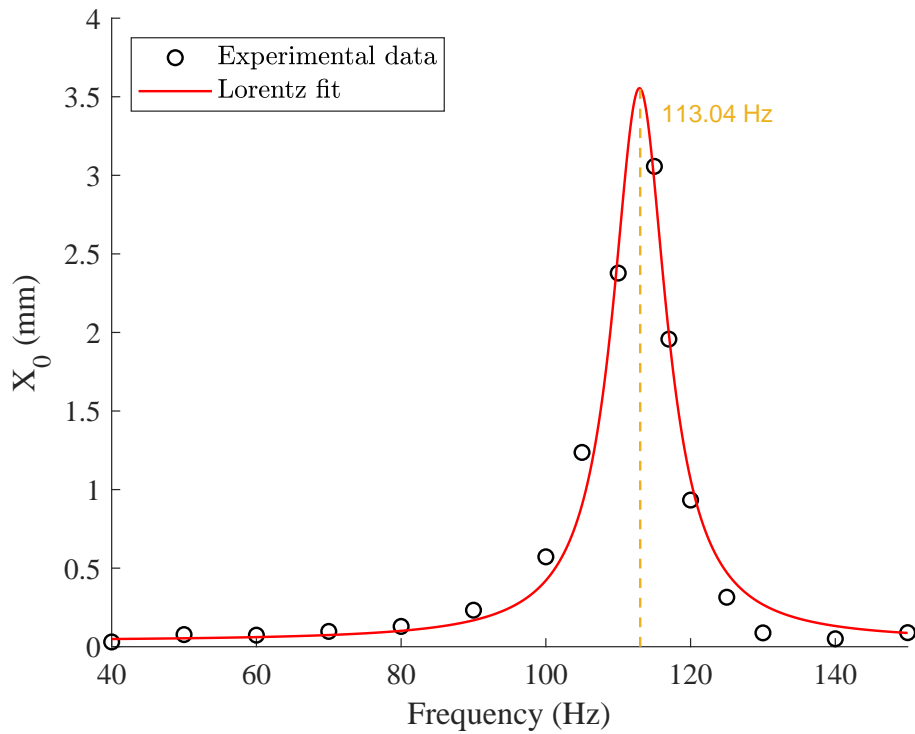
**Table 5.1:** Data from the frequency sweep analysis of the U-shaped harvester body.

$f$ (Hz)	$I_{RMS}$ (mA)	$V_{out}$ (mV)	$V_{App}$ (mV)	$A_0$ (m/s <sup>2</sup> )	$Y_0$ (mm)	$X_0$ (mm)
40	14.35	460	130	6.38	0.1009	0.0303
50	44.82	525	206	10.10	0.1024	0.0772
60	82.41	520	306	15.01	0.1056	0.0736
70	130.79	553	409	20.06	0.1037	0.0974
80	186.54	597	527	25.85	0.1023	0.1292
90	252.66	740	670	32.86	0.1028	0.2325
100	341.44	1210	835	40.96	0.1037	0.5720
105	412.48	2130	934	45.81	0.1053	1.2366
110	489.48	3710	1010	49.54	0.1037	2.3779
115	486.33	4650	1050	51.50	0.0986	3.0569
117	450.87	3128	1145	56.16	0.1039	1.9575
120	384.59	1710	1190	58.37	0.1027	0.9332
125	448.71	854	1262	61.90	0.1004	0.3149
130	503.62	540	1400	68.67	0.1029	0.0880
140	616.64	488	1640	80.44	0.1040	0.0505
150	716.04	542	1880	92.21	0.1038	0.0895

In order to analyze at which frequency the resonance peak is located,  $X_0$  is plotted versus frequency. To have an estimated curve from the experimental data, it is fitted to a Lorentz curve by using MATLAB<sup>®</sup>, whose expression is given in Equation 5.2. In this expression  $y_0$  is the offset of the curve,  $x_c$  is the center,  $w$  is the width and  $A$  is the area. In Figure 5.1 it can be seen a value of 113 Hz is obtained for the resonance frequency from the fitting procedure, close to the desired 100 Hz.

$$y = y_0 + \frac{2A}{\pi} \frac{w}{4(x - x_c)^2 + w^2} \quad (5.2)$$





**Figure 5.1:** Frequency sweep of the U-shaped harvester body.

## 5.2. Potential Harvester Construction

Although this work is focused on the design of the U-shaped main body, its potential application is linked to the construction of a magnetostrictive harvester. The harvester implementation requires the addition of different elements to the analyzed structure, basically the magnetostrictive layer and the pick-up coil fixing piece. Despite the performance of a potential harvester is not an objective of this work (and not characterized), the effect of the addition of these elements to the U-shaped body performance is experimentally analyzed. Analogously to the previous section, their effect on the frequency and amplitude of vibration is studied. The possibility of tuning the frequency of resonance with the addition of “tip masses” was also examined.

### 5.2.1. U-shaped Harvester Body with Galfenol Sheet and 3D-printed Piece

In this section it is analyzed the effect of the incorporation of the magnetostrictive material sheet and the 3D-printed wiring component to the behavior of the harvester structure. A brief description of both elements is performed.

### 5.2.1.1. Galfenol Sheet

The magnetostrictive material selected for constructing the harvester was Galfenol ( $\text{Fe}_{81.6}\text{Ga}_{18.4}$ ) due to its proper balance between cost and performance (see properties in Table 2.2). Several  $20 \times 4 \times 0.5$  mm pieces were supplied by TdVib LLC. Two different types of Galfenol sheets were purchased: as-cast, and stress-annealed under a compressive stress of 20 MPa.

The optimal Galfenol sheet selection for the future harvester is explained in Appendix B. This decision does not have any implications in the present work since it does not affect the mechanical properties of the vibrant magnetic structure. However, it is a key factor in the future harvester performance that would integrate the vibrant U-shaped structure developed in this project. Figure 5.2 shows one of the provided as-cast Galfenol pieces.



**Figure 5.2:** As-cast Galfenol sheet.

To fix the Galfenol sheet to the U-shaped main body, an epoxy adhesive (Rapid Araldite<sup>®</sup> from CEYS) was used. The fixation with this adhesive will guarantee the transmission of stresses between the two components for a wide range of stresses and temperatures, making the joint highly durable. Figure 5.3 shows the assembly of the Galfenol sheet on the U-shaped body next to a U-shaped body without the magnetostrictive layer.



**Figure 5.3:** U-shaped iron body with and without glued Galfenol sheet.

It is noted that the Galfenol layer has been glued as close as possible to the curved part of the U-shaped main body due to the fact it is in this place that the higher stresses will occur in a similar way to what it happens in a clamped beam (see stress simulation results in sections 3.2.7 and 5.3).

### 5.2.1.2. Copper Wiring

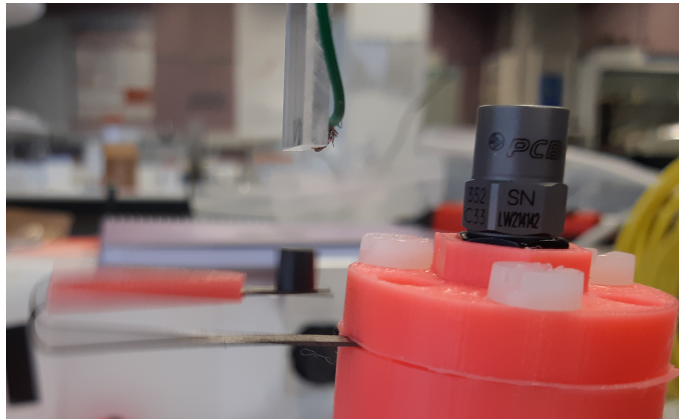
In order to ease the copper wiring assembly in the harvester, this wiring will be made on a Polylactic Acid (PLA) 3D-printed piece whose dimensions are indicated in Plan 1.03 in Appendix A. This way, the wiring could be easily located and retired from the harvester assembly. Figure 5.4 shows the 3D-printed piece around which there will be between 2000 and 3000 coil turns of a 0.05 mm in diameter copper wire.



**Figure 5.4:** U-shaped body with Galfenol sheet and 3D-printed wiring piece.

### 5.2.1.3. Resonance Analysis

Analogously to Section 5.1, after assembling the Galfenol sheet to the U-shape and locating the 3D-printed piece, a second resonance analysis is done. Figure 5.5 shows the visible resonant vibration of the structure with the attached elements during the laboratory experiment.



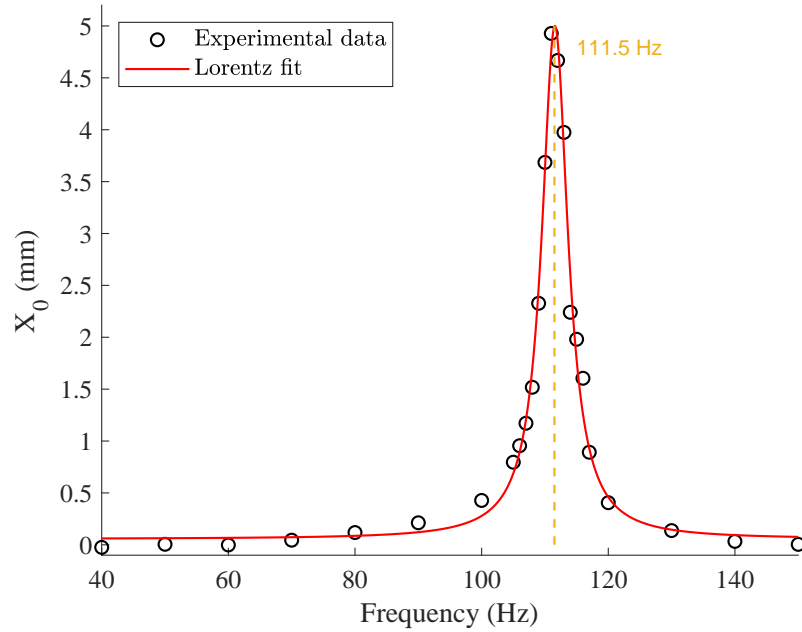
**Figure 5.5:** Structure body with Galfenol sheet and 3D-printed piece oscillating in resonance.

Table 5.2 shows the data gathered from the frequency sweep and Figure 5.6 presents the obtained results. The resonance peak is observed at a frequency of 111.5 Hz, a slightly lower frequency than the one observed in Section 5.1. This lower frequency is

justified by the fact that some mass has been added to the upper part of the U-shaped structure. Nonetheless, this resonance frequency change is not very significant due to the low weight of the Galfenol sheet and the PLA 3D-printed piece.

**Table 5.2:** Data from the frequency sweep analysis of the U-shaped harvester body with Galfenol sheet and 3D-printed piece.

$f$ (Hz)	$I_{RMS}$ (mA)	$V_{out}$ (mV)	$V_{App}$ (mV)	$A_0$ (m/s <sup>2</sup> )	$Y_0$ (mm)	$X_0$ (mm)
40	24.88	384	128	6.28	0.0994	-0.0246
50	48.60	425	220	10.79	0.1093	0.0050
60	82.87	416	312	15.30	0.1077	-0.0015
70	130.95	480	420	20.60	0.1065	0.0447
80	185.87	582	536	26.29	0.1041	0.1184
90	251.13	712	680	33.35	0.1043	0.2123
100	319.46	1010	810	39.73	0.1006	0.4275
105	310.73	1520	890	43.65	0.1003	0.7959
106	320.65	1740	936	45.91	0.1035	0.9549
107	328.92	2040	952	46.70	0.1033	1.1716
108	335.52	2520	960	47.09	0.1023	1.5183
109	358.02	3640	984	48.27	0.1029	2.3273
110	404.48	5520	968	47.48	0.0994	3.6853
111	415.92	7240	1084	53.17	0.1093	4.9277
112	423.21	6880	1072	52.58	0.1062	4.6677
113	425.61	5920	1040	51.01	0.1012	3.9742
114	427.46	3520	1072	52.58	0.1025	2.2406
115	435.79	3160	1072	52.58	0.1007	1.9806
116	438.65	2640	1152	56.51	0.1064	1.6050
117	442.12	1653	1180	57.88	0.1071	0.8920
120	453.78	980	1180	57.88	0.1018	0.4059
130	490.14	608	1460	71.61	0.1073	0.1372
140	599.88	464	1660	81.42	0.1052	0.0331
150	736.11	424	1980	97.12	0.1093	0.0043



**Figure 5.6:** Frequency sweep of the U-shaped harvester body with Galfenol sheet and 3D-printed piece.

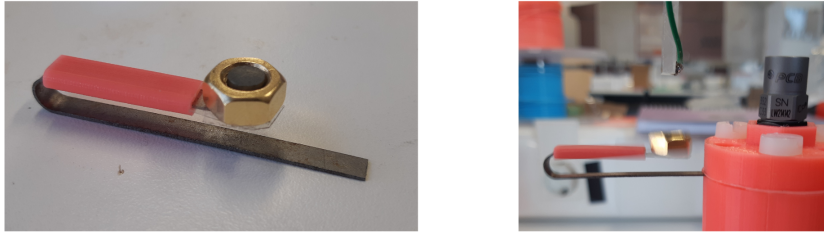
## 5.2.2. U-shaped Harvester Body with Galfenol Sheet, 3D-printed Piece and Additional Tip Mass

In this section it is analyzed how the incorporation of an additional mass affects the behavior of the harvester structure in terms of the possible variation of the frequency of resonance.

### 5.2.2.1. Tip Mass

The tip mass is the additional element which is added in the upper edge of the U-shaped body to tune its frequency of resonance (see Figure 3.1). As an initial tip mass the ferrite magnet was used. It is important to recall that this magnet permits the estimation of  $X_0$  by the GMI-based magnetic sensor.

Additional mass was added to the prototype in order to characterize the structure with this additional element and evaluate the tuning capabilities. A brass nut with a mass of 2.1972 g was fixed to the tip of the prototype with adhesive tape. This particular element was selected due to the fact it has an inner hole into which the ferrite magnet enters, and because it is made of a non-ferromagnetic material, so it does not affect the vibration magnetic sensor measurements. Figure 5.7 shows two pictures of the prototype with the additional tip mass.



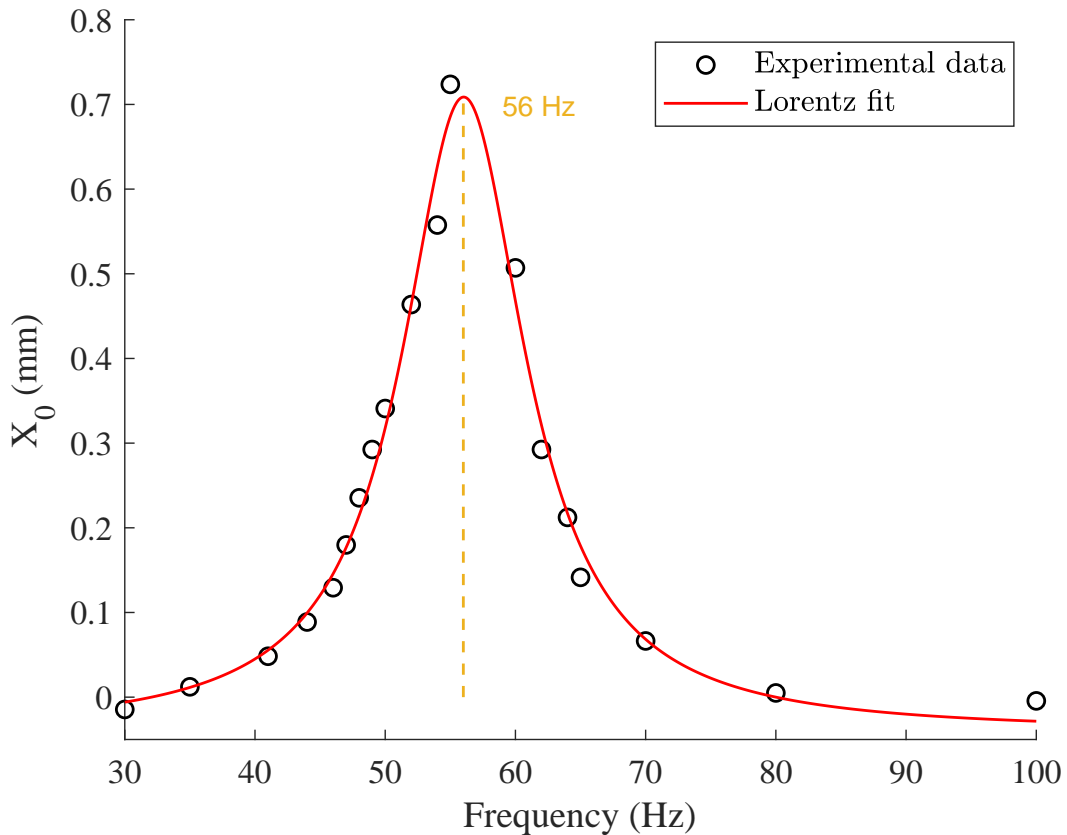
**Figure 5.7:** Structure body with Galfenol sheet, 3D-printed piece and additional tip mass.

### 5.2.2.2. Resonance Analysis

Analogously to Section 5.1, a third resonance analysis is done after adding the additional tip mass. Table 5.3 and Figure 5.8 present the obtained results.

**Table 5.3:** Data from the frequency sweep analysis of the U-shaped harvester body with Galfenol sheet, 3D-printed piece and additional tip mass.

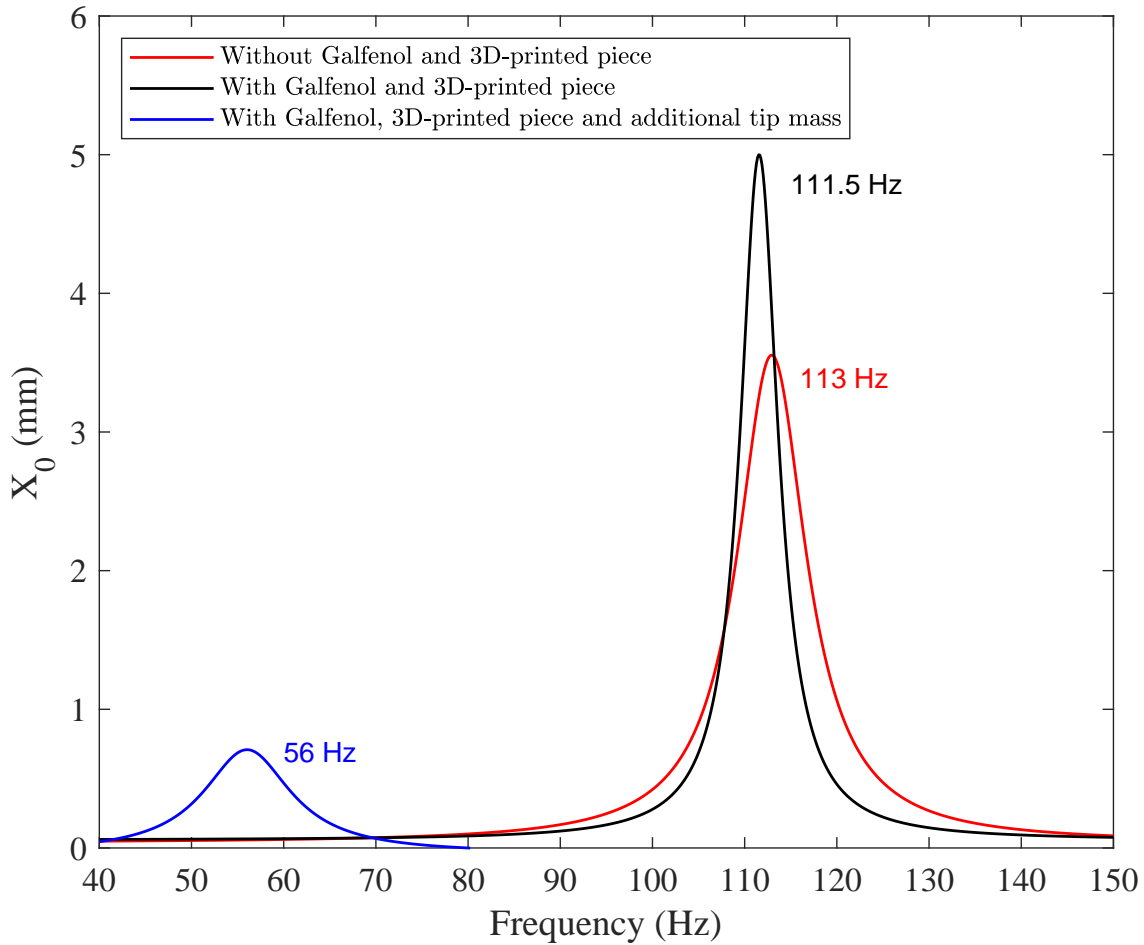
$f$ (Hz)	$I_{RMS}$ (mA)	$V_{out}$ (mV)	$V_{App}$ (mV)	$A_0$ (m/s <sup>2</sup> )	$Y_0$ (mm)	$X_0$ (mm)
30	16.33	398	72	3.53	0.0994	-0.0145
35	17.28	435	102	5.00	0.1035	0.0122
41	23.72	485	132	6.47	0.0976	0.0483
44	31.42	541	156	7.65	0.1001	0.0888
46	34.60	597	168	8.24	0.0986	0.1292
47	37.39	667	172	8.44	0.0967	0.1798
48	39.01	744	182	8.93	0.0981	0.2354
49	41.66	823	188	9.22	0.0973	0.2925
50	45.13	890	198	9.71	0.0984	0.3409
52	50.89	1060	210	10.30	0.0965	0.4637
54	36.06	1190	225	11.04	0.0959	0.5576
55	30.78	1420	243	11.92	0.0998	0.7237
60	40.29	1120	294	14.42	0.1015	0.5070
62	36.06	823	321	15.75	0.1038	0.2925
64	30.78	712	329	16.14	0.0998	0.2123
65	34.98	614	352	17.27	0.1035	0.1415
70	91.58	510	412	20.21	0.1045	0.0664
80	123.44	425	547	26.83	0.1062	0.0050
100	173.21	412	794	38.95	0.0987	-0.0044



**Figure 5.8:** Frequency sweep of the U-shaped harvester body with Galfenol sheet, 3D-printed piece and additional tip mass.

The resonance peak is observed at a frequency of 56 Hz, which is a significant change compared to the one observed in sections 5.1 and 5.2.1.3. This relevant frequency reduction is due to the weight added to the tip, of 2.1972 g, which results to be high in comparison with the weight of the Galfenol sheet and the PLA 3D-printed piece. These results imply that the resonance frequency of the system can be easily tuned by just modifying the tip mass.

Finally, the resonance analyses for the three different prototype configurations are compared in Figure 5.9. It can be seen how the resonance frequency is barely lowered when adding the Galfenol and the 3D-printed piece, and how it is approximately halved with the addition of the tip mass. It is observed the amplitude of vibration increases when including the Galfenol and the 3D-printed wiring piece. However, a clear decrease in the amplitude of vibration is noticed when incorporating the additional tip mass. This amplitude of vibration variation can be attributed to the difference of stiffness, mass and geometry between the different configurations, that introduce variations in the vibration resonant modes and resonant frequencies.



**Figure 5.9:** Comparison between the resonance analyses at a constant shaker vibration amplitude of 0.1 mm.

### 5.3. Comparison between Theoretical and Empirical Results

In this section, the theoretical and the empirical obtained results are compared. In order to determine the damping parameters to perform the numerical simulation, the ideal (no damping) theoretical resonance curve is compared with the respective experimental one obtained from the laboratory data. These damping coefficients are only determined for the U-shaped body with the ferrite magnet tip mass without any other additional element. Nevertheless, it is important to mention that their adjustment does not affect significantly to the value of the resonance frequency. A Young modulus of 113 GPa (similar to the initially considered value of 110 GPa from [23] since the manufacturer of the U-shaped body did not provide this data) is considered. This slight variation modifies the resonance frequency value from 111.7 Hz to 113.2 Hz.

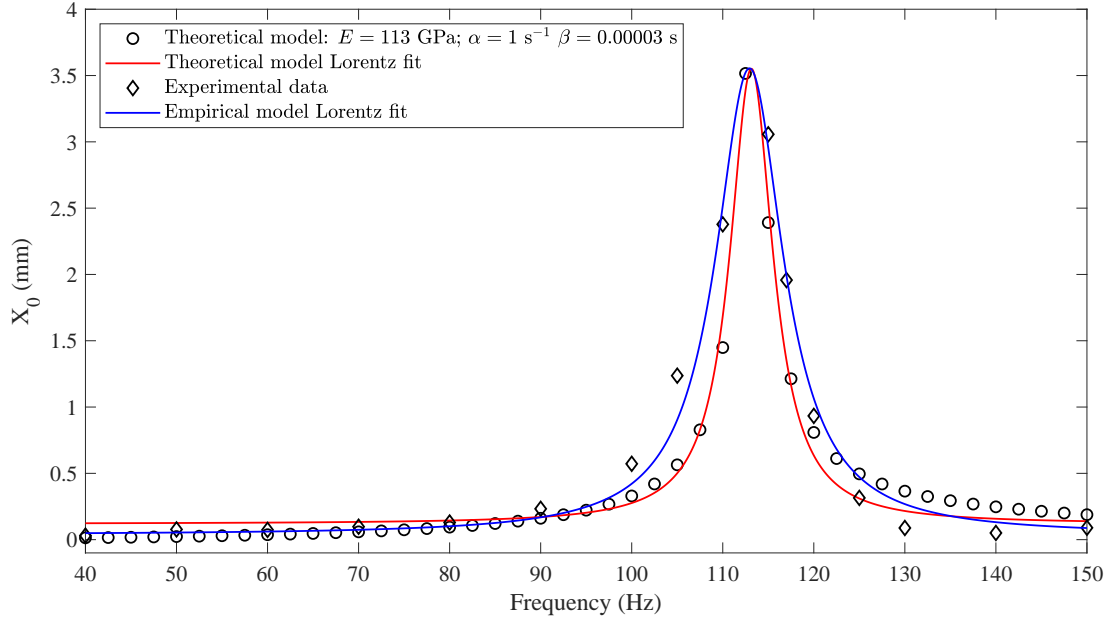


The values for the two Rayleigh parameters,  $\alpha$  and  $\beta$ , that lead to the best fit between the theoretical and the laboratory data for the U-shaped main body with the tip mass are shown in Table 5.4.

**Table 5.4:** Damping coefficients determination.

$\alpha$ ( $s^{-1}$ )	$\beta$ (s)
1	0.00003

Figure 5.10 shows the theoretical prediction and the empirical results for the U-shaped body with the tip mass conformed by the cylindrical ferrite magnet.

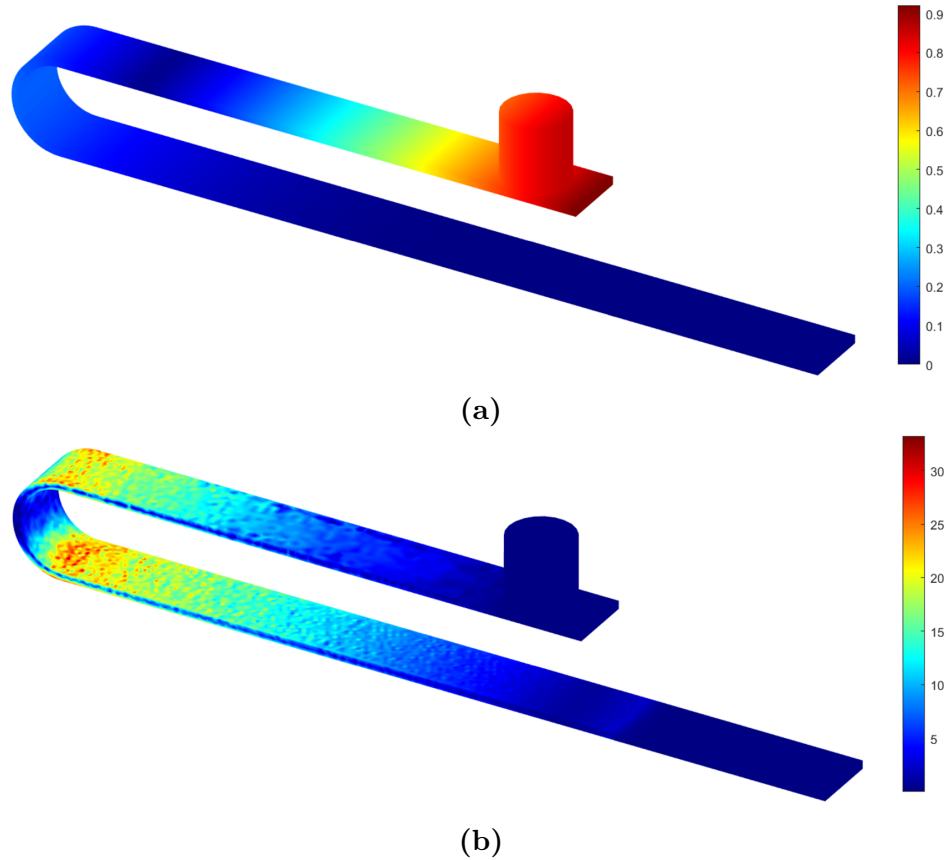


**Figure 5.10:** Comparison of theoretical and empirical results of the U-shaped body.

It can be observed that the theoretical results agree with the results obtained in the laboratory. Thus, the theoretical model is optimum to model the behavior of the system and permits to predict the performance of the U-shaped vibrating structure (and the harvester based on it), in terms of its resonance. This affirmation also relies on the fact that, as checked experimentally, the addition of the magnetostrictive sheet and the pick-up coil barely modify the resonance frequency. As a consequence, the previously proposed modeling has been revealed as a powerful tool for the design of magnetostrictive harvester devices.

Now the Rayleigh damping parameters are known, the dynamic simulation is performed following the procedure indicated in Section 3.2.8. The displacements in the  $z$

direction for the U-shaped main harvester body as well as the  $\sigma_{xx}$  stresses are shown in Figure 5.11. These displacements and stresses are the solutions for a vibration source with a frequency of 113 Hz (resonance frequency) and an acceleration of 10 m/s<sup>2</sup>.



**Figure 5.11:** (a) Displacement in  $z$  direction (mm) under dynamic loading for the two-domain geometry. (b)  $\sigma_{xx}$  (MPa) under dynamic loading for the two-domain geometry.

In Figure 5.11 it can be observed that the maximum displacements are lower than the distance between the upper and the lower parts of the U-shaped main body, so the design is validated for dynamic resonance conditions. The oscillation amplitudes can be seen to be lower than in the resonance analyses due to the fact the shaker oscillation amplitude,  $Y_0$ , corresponding to a peak acceleration  $A_0$  of 10 m/s<sup>2</sup> for a frequency of 113 Hz, is lower than 0.1 mm (0.0198 mm). With respect to the generated stresses, maximum  $\sigma_{xx}$  stresses are observed in the bent part of the U-shaped main body as in the static solution.

It should be noticed that the solutions for the displacements and stresses in Figure 5.11 are amplitude values. Thus, in order to obtain the total displacements and stresses, the constant values from the static solution in Figure 3.12 should be added. However,

it can be seen that the displacements and stresses produced by the action of gravity in static are almost negligible in comparison to those produced by the vibration source.



# Chapter 6

## Conclusions and Future Work

In this last chapter, the main conclusions extracted from the project are exposed and contrasted with the initial objectives. Additionally, the future work lines to further develop this work are commented.

### 6.1. Main Conclusions

The fulfillment of the objectives presented at the beginning of this project is discussed in the present section, together with the conclusions of the obtained theoretical and empirical results.

The different objectives that were initially proposed in Chapter 1 have been successfully achieved. A magnetic vibrant structure was designed from the initial proposal of Ueno in [20] by using SolidWorks<sup>®</sup>. This design was submitted to numerical simulations in MATLAB<sup>®</sup> in order to validate the design by the analysis of the resonance frequency, the stresses and the displacements under static and dynamic conditions. Since all these factors were optimized, it was concluded that the structure could suppose the base for a magnetostrictive vibrational harvester with an adequate performance. Moreover, the prototype has a great potential in low frequency applications thanks to its low material and manufacturing costs, its long useful life, its compactness and its tuning possibilities.

An initial prototype was then constructed and different parts of the future magnetostrictive harvester were included in order to study empirically the behavior of different configurations of the system. It was observed that the behavior of the design was easily-adjustable, something which increases its applications potential thanks to the possibility of customizing the resonance frequency to obtain the maximum performance on each use.

Finally, the results obtained in the numerical simulations in MATLAB<sup>®</sup> for the U-shaped body, show a relevant agreement with the experimental data. This fact validates

the performed theoretical analysis as a pre-manufacturing stage of the prototype where the main features can be estimated with accuracy, which implies lower design costs for obtaining the desired behavior of the device.

## 6.2. Future Work Lines

There exist three main future work lines that could suppose the continuation of the present project and have been excluded due to time constraints:

- Determination of the harvester performance along time and possible ways to lower the cost of the design.
- Magnetic and electric numerical simulations to be able to study the overall behavior of the harvester without the need of constructing it.
- Implementation of the device in real applications.

### 6.2.1. Harvester Performance Determination

This project has centered on the design and validation of the magnetic vibrant structure that would constitute the base of a future magnetostrictive harvester. The next step to what has been done in this work would be to assemble the copper pick-up coil on the 3D-printed wiring piece. After this, the induced emf could be measured with an oscilloscope, in order to determine the performance of the harvester. An study on which is the optimal load for obtaining the maximum power from the harvesting device (for different frequencies and accelerations) would also be highly useful to adapt the harvester to different applications.

Though in this project Galfenol has been used as magnetostrictive material due to its greater magnetostrictive saturation constant, it could be studied whether Fe–Co alloys could be employed to lower the harvester cost with comparable performance. A possible way to obtain a similar performance would be to implement a second magnetostrictive sheet on the opposite side of the upper part of the U-shaped main body. This can not be made with Galfenol due to the fact it presents a positive magnetostriction constant and it would lead to the canceling of the magnetic flux variation through the coil. However, Fe–Co alloys present the possibility of having negative magnetostriction, so that both the upper and the lower active layers can contribute to augment the magnetic flux variation through the coil without canceling, enhancing harvester's performance.

Additionally, during this project it was commented that the U-shaped main body of the harvester was susceptible to pitting corrosion. An study could be done on how

---

this phenomenon affects the performance and the durability of the device, with fatigue tests and emf measurements.

### 6.2.2. Mechanical-Magnetic Coupling and Electromagnetic Induction Numerical Simulations

In addition to the mechanical numerical simulations carried out in this project, a further simulation study could be done. By using MATLAB<sup>®</sup>, it could be numerically simulated the mechanical-magnetic coupling (governed by Villari's or inverse magnetostriction effect), as well as the electromotive force induction that would take place (governed by Faraday's law). There exist no specific functions for magnetostriction phenomenons in MATLAB<sup>®</sup> so the needed functions would be implemented manually.

These additional numerical simulations could be afterwards compared with the experimental results in order to check if the modeling of the inverse magnetostriction and electromotive force induction effects is adequate. If the modeling is accurate, the code could be used to modify the geometry and parameters of design to further optimize the harvester, diminishing the experimentation costs to obtain the best device possible.

### 6.2.3. Real Applications Implementation

Finally, after having a complete characterization of the device, knowing how its performance is affected by ambient conditions and time; it could be optimized for a particular use and implemented in different real applications. Industrial applications in particular show a high potential due to the large presence of heavy machinery whose generated vibrations are of low frequency (approximately 100 Hz [9]). Moreover, these vibrations are commonly periodic if generated by rotating machines, something which enhances the harvester performance (closer to ideal sinusoidal vibrations). An study could be performed in order to enable the energy collected by the harvester from a variable vibrating source, to power a device whose consumption is not constant along time.

---





# Bibliography

- [1] F. Narita and M. Fox, “A Review on Piezoelectric, Magnetostrictive, and Magnetoelectric Materials and Device Technologies for Energy Harvesting Application,” *Advanced Engineering Materials*, vol. 20, no. 5, p. 1700743, Nov. 2017, doi: 10.1002/adem.201700743.
- [2] A. Al-Fuqaha, M. Guizani, M. Mohammadi, M. Aledhari, and M. Ayyash, “Internet of Things: A Survey on Enabling Technologies, Protocols and Applications,” *IEEE Communications Surveys & Tutorials*, vol. 17, no. 4, pp. 2347–2376, Nov. 2015, doi: 10.1109/COMST.2015.2444095.
- [3] L. Wang and F. Yuan, “Vibration energy harvesting by magnetostrictive material,” *Smart Materials and Structures*, vol. 17, no. 4, pp. 45 009–14, Aug. 2008, doi: 10.1088/0964-1726/17/4/045009.
- [4] A. Patil and A. Shirolkar, “A Review on System-on-Chip SoC Designs for Real-Time Industrial Application,” *International Journal of Trend in Scientific Research and Development*, vol. 2, no. 1, pp. 1534–1537, Dec. 2017, doi: 10.31142/ijtsrd7077.
- [5] K. Lasse, “State of the IoT 2018: Number of IoT devices now at 7B - Market accelerating,” *IoT Analytics*, 2018. [Online]. Available: <https://iot-analytics.com/state-of-the-iot-update-q1-q2-2018-number-of-iot-devices-now-7b/> [Accessed: Aug. 18, 2021]
- [6] M. Shirvanimoghaddam *et al.*, “Paving the Path to a Green and Self-Powered Internet of Things,” Dec. 2017.
- [7] Z. Deng and M. J. Dapino, “Review of magnetostrictive vibration energy harvesters,” *Smart Materials and Structures*, vol. 26, no. 10, p. 103001, Sep. 2017, doi: 10.1088/1361-665X/aa8347.
- [8] S. Roundy, P. K. Wright, and J. Rabaey, “A Study of Low Level Vibrations as a Power Source for Wireless Sensor Nodes,” *Computer Communications*, vol. 26, no. 11, pp. 1131–1144, Jul. 2003, doi: 10.1016/S0140-3664(02)00248-7.
- [9] L. Tang, Y. Yang, and C. Soh, “Toward Broadband Vibration-based Energy Harvesting,” *Journal of Intelligent Material Systems and Structures*, vol. 21, pp. 1867–

- 1897, Dec. 2010, doi: 10.1177/1045389X10390249.
- [10] S. Dey, D. Roy, S. Patra, and T. Santra, “Performance of a modified magnetostrictive energy harvester in mechanical vibration,” *Heliyon*, vol. 5, p. e01135, Jan. 2019, doi: 10.1016/j.heliyon.2019.e01135.
- [11] G. Bertotti, *Hysteresis in Magnetism*. San Diego: Academic Press, 1998, pp. 129–162.
- [12] J. Slaughter and E. Summers, “Galfenol Energy Harvesting,” *ETREMA Products, Inc.*, 2017. [Online]. Available: [http://www.tdvib.com/wp-content/uploads/2015/07/whitepaper\\_galfenolenergyharvester.pdf](http://www.tdvib.com/wp-content/uploads/2015/07/whitepaper_galfenolenergyharvester.pdf) [Accessed: Dec. 21, 2021]
- [13] V. Berbyuk, “Vibration energy harvesting using Galfenol based transducer,” *Proceedings of SPIE - The International Society for Optical Engineering*, vol. 8868, Apr. 2013, doi: 10.1117/12.2009812.
- [14] H. Zhang, “Power generation transducer from magnetostrictive materials,” *Applied Physics Letters*, vol. 98, no. 23, p. 2505, Jun. 2011, doi: 10.1063/1.3597222.
- [15] T. Ueno and S. Yamada, “Performance of Energy Harvester Using Iron–Gallium Alloy in Free Vibration,” *IEEE Transactions on Magnetics*, vol. 47, no. 10, pp. 2407–2409, Oct. 2011, doi: 10.1109/TMAG.2011.2158303.
- [16] Y. Park, H. Kang, and N. M. Wereley, “Conceptual design of rotatory magnetostrictive energy harvester,” *Journal of Applied Physics*, vol. 115, no. 17, 2014, doi: 10.1063/1.4865976.
- [17] S. Kita, T. Ueno, and S. Yamada, “Improvement of force of magnetostrictive vibration power generator for high efficiency,” *Journal of Applied Physics*, vol. 117, no. 17, p. 17B508, May 2015, doi: 10.1063/1.4907237.
- [18] T. Ueno, “U-shape magnetostrictive vibration based power generator for universal use,” in *Smart Materials and Nondestructive Evaluation for Energy Systems 2016*, vol. 9806, Apr. 2016, p. 98060E, doi: 10.1117/12.2218759.
- [19] P. L. Gould, *Introduction to Linear Elasticity*. New York: Springer, 1994, pp. 39–67.
- [20] T. Ueno, “Magnetostrictive low-cost high-performance vibration power generator,” *Journal of Physics Conference Series*, vol. 1052, no. 1, p. 012075, Jul. 2018, doi: 10.1088/1742-6596/1052/1/012075.
- [21] I. Zureks, “Example of 2D Mesh,” *Wikimedia Commons*, 2021. [Online]. Available: [https://commons.wikimedia.org/wiki/File:Example\\_of\\_2D\\_mesh.png](https://commons.wikimedia.org/wiki/File:Example_of_2D_mesh.png) [Accessed: Dec. 20, 2021]
-

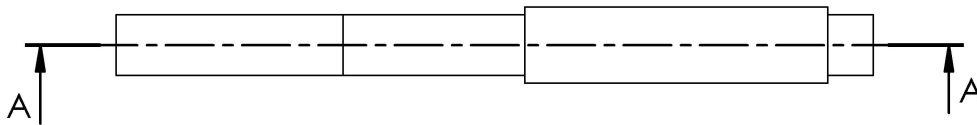
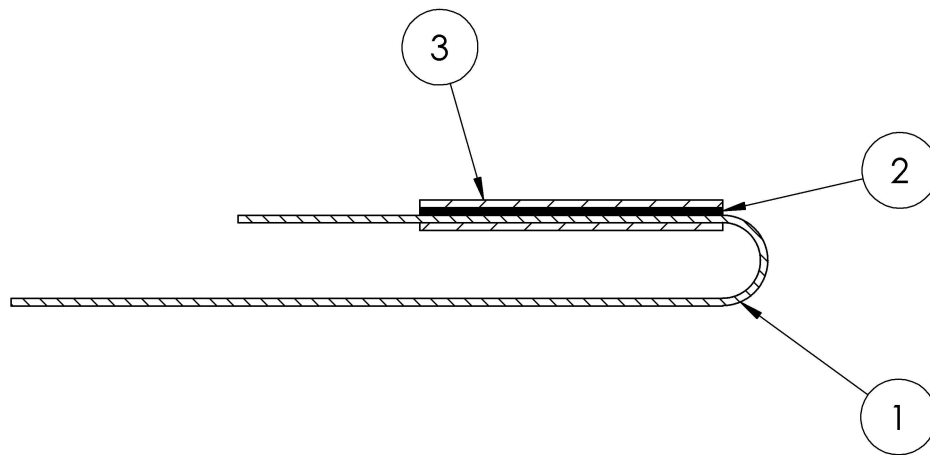
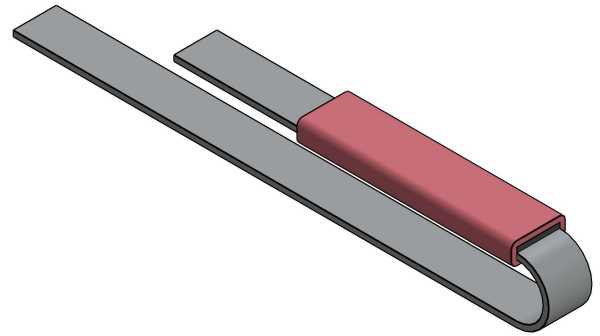
- 
- [22] C. Geuzaine and J. Remacle, "Gmsh. A three-dimensional finite element mesh generator with built-in pre- and post- processing facilities," *International Journal for Numerical Methods in Engineering*, vol. 79, no. 11, pp. 1309–1331, Sep. 2009, doi: 10.1002/nme.2579.
- [23] M. Elsherbiny, A. Khattab, and M. Kassab, "Design of a Deployment Mechanism for the Solar Array on a Small Satellite," *American Journal of Mechanical Engineering*, vol. 1, no. 3, pp. 66–72, Jan. 2012, doi: 10.12691/ajme-1-3-2.
- [24] C. S. Clemente and D. Davino, "Modeling and Characterization of a Kinetic Energy Harvesting Device Based on Galfenol," *Materials*, vol. 12, no. 19, p. 3199, Sep. 2019, doi: 10.3390/ma12193199.
- [25] J. Torres, J. Coteló, J. Karl, and A. P. Gordon, "Mechanical Property Optimization of FDM PLA in Shear with Multiple Objectives," *JOM*, vol. 67, pp. 1183–1193, Mar. 2015, doi: 10.1007/S11837-015-1367-Y.
- [26] J. J. Beato-López, I. Royo-Sirvestre, J. M. Algueta-Miguel, and C. Gómez-Polo, "A Combination of a Vibrational Electromagnetic Energy Harvester and a Giant Magnetoimpedance (GMI) Sensor," *Sensors*, vol. 20, no. 7, p. 1873, Mar. 2020, doi: 10.3390/s20071873.
- [27] "Structural Dynamics of Tuning Fork," *MathWorks, Inc.*, 2021. [Online]. Available: <https://es.mathworks.com/help/pde/ug/structural-dynamics-of-tuning-fork.html> [Accessed: Sep. 3, 2021]
- [28] C. S. Clemente, D. Davino, and V. P. Loschiavo, "Analysis of a Magnetostrictive Harvester with a Fully Coupled Nonlinear FEM modelling," *IEEE Transactions on Magnetics*, vol. 57, no. 6, pp. 1–4, Jun. 2021.
- [29] H. Liu, W. Li, X. Sun, C. Cong, C. Cao, and Q. Zhao, "Enhanced the capability of magnetostrictive ambient vibration harvester through structural configuration, pre-magnetization condition and elastic magnifier," *Journal of Sound and Vibration*, vol. 492, no. 3, p. 115805, Oct. 2020, doi:10.1016/j.jsv.2020.115805.
- [30] H. Liu, C. Cong, Q. Zhao, and K. Ma, "Comprehensive Analysis of the Energy Harvesting Performance of a Fe-Ga Based Cantilever Harvester in Free Excitation and Base Excitation Mode," *Sensors*, vol. 19, no. 15, p. 3412, Aug. 2019, doi: 10.3390/s19153412.
- [31] M. Ito, T. Minamitani, and T. Ueno, "Influences of Fe-Ga Alloy Crystallinity for the Application to a Magnetostrictive Vibration Energy Harvester," *Journal of Physics Conference Series*, vol. 1407, no. 1, p. 012113, Nov. 2019, doi: 10.1088/1742-6596/1407/1/012113.
- [32] R. J. M. Vullers, R. V. Schaijk, I. Doms, C. V. Hoof, and R. Mertens, "Micropower
-


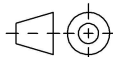
- energy harvesting,” *Solid-State Electronics*, vol. 53, no. 7, pp. 684–693, Jul. 2009, doi: 10.1016/j.sse.2008.12.011.
- [33] K. Mori *et al.*, “On the Possibility of Developing Magnetostrictive Fe-Co/Ni Clad Plate with Both Vibration Energy Harvesting and Mass Sensing Elements,” *Materials*, vol. 14, no. 16, p. 4486, Aug. 2021, doi: 10.3390/ma14164486.
- [34] Q. Cao *et al.*, “Modeling and experiments of a laminated magnetostrictive cantilever beam,” *Advances in Mechanical Engineering*, vol. 7, no. 4, Apr. 2015, doi: 10.1177/1687814015573761.
- [35] H. M. Schurter and A. Flatau, “Elastic properties and auxetic behavior of Galfenol for a range of compositions,” *Proceedings of SPIE - The International Society for Optical Engineering*, vol. 6929, Mar. 2008, doi: 10.1117/12.776173.
-

## **Appendix A**

### **Vibrant Magnetic Structure and Support Technical Drawings**

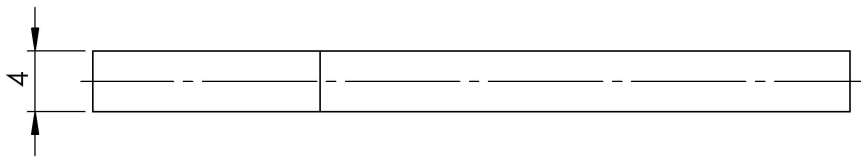
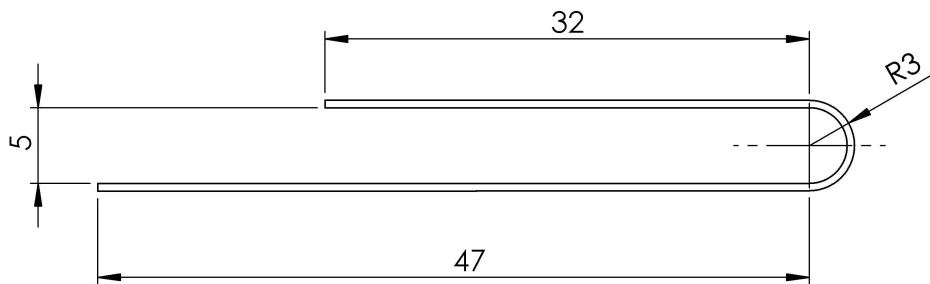
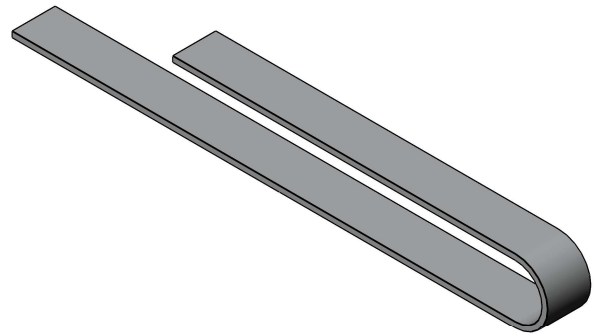




ELEMENT N°	CODE	DESCRIPTION	MATERIAL	QUANTITY
1	HARV-101	U-SHAPE MAIN BODY	IRON	1
2	HARV-102	MAGNETOSTRICTIVE SHEET	GALFENOL	1
3	HARV-103	3D-PRINTED WIRING PIECE	PLA	1
DATE: 04/01/2022		SIGNATURE: 		
AUTHOR: Daniel Sotelo Aguirre		PROJECT: DESIGN, SIMULATION, CONSTRUCTION AND CHARACTERIZATION OF A VIBRANT MAGNETIC STRUCTURE FOR ITS USE IN MAGNETOSTRICTIVE ENERGY HARVESTERS		
<b>E.T.S.I.I.I.T</b>		DENOMINATION: VIBRANT MAGNETIC STRUCTURE		WEIGHT (g): 1.843
<b>upna</b>		PLANE N°: 1.00	CODE: HARV-100	 A4 SCALE: 2:1

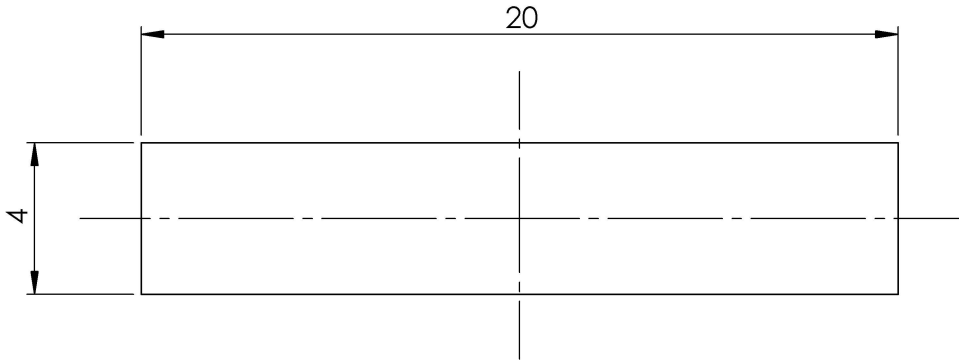
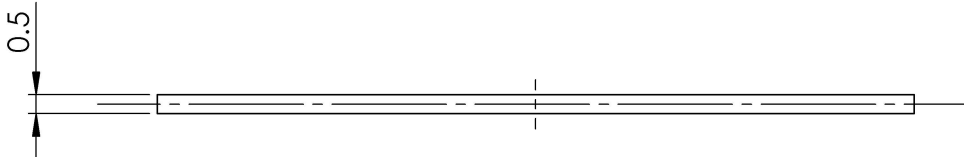
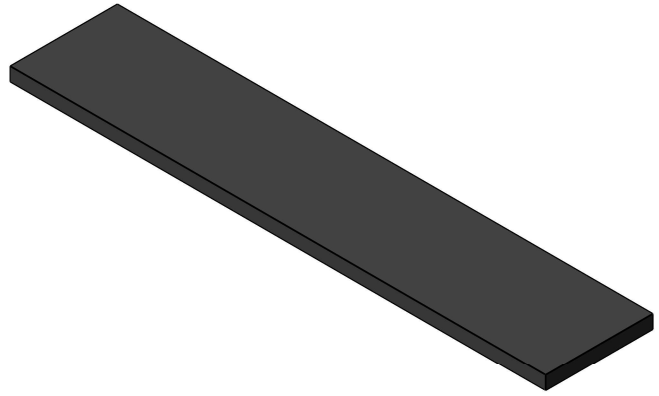






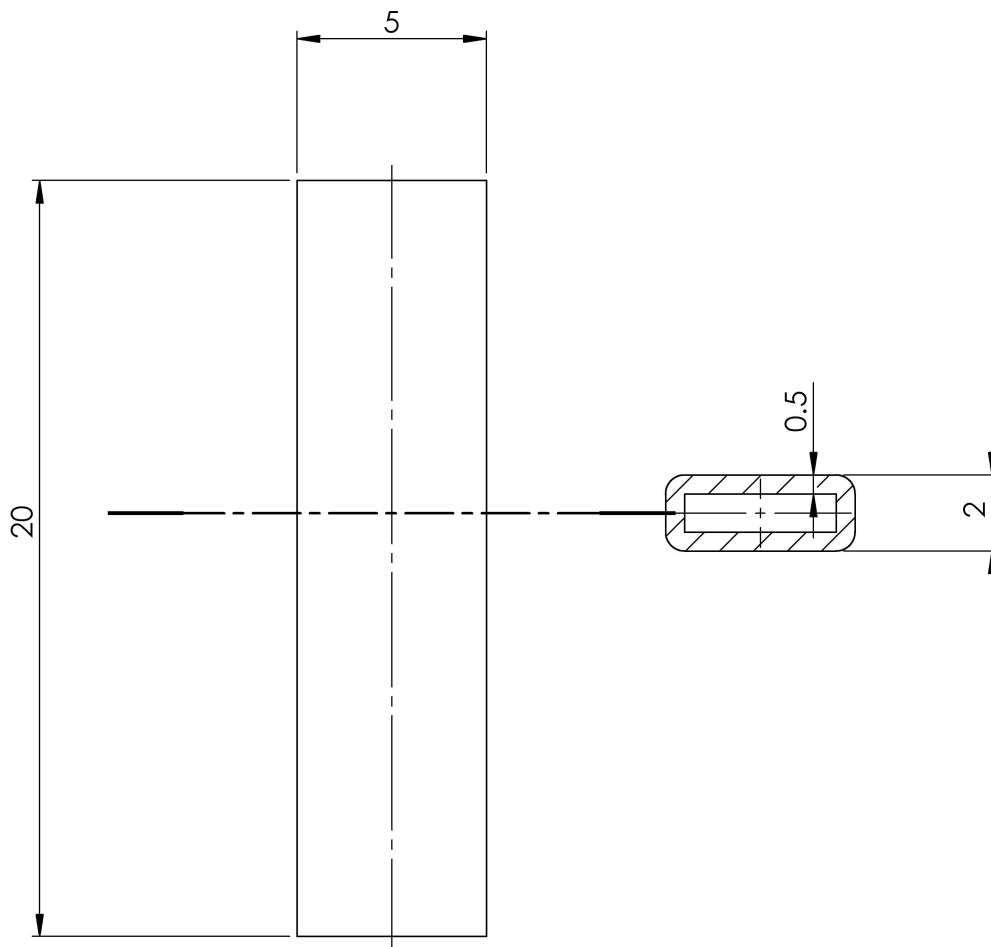
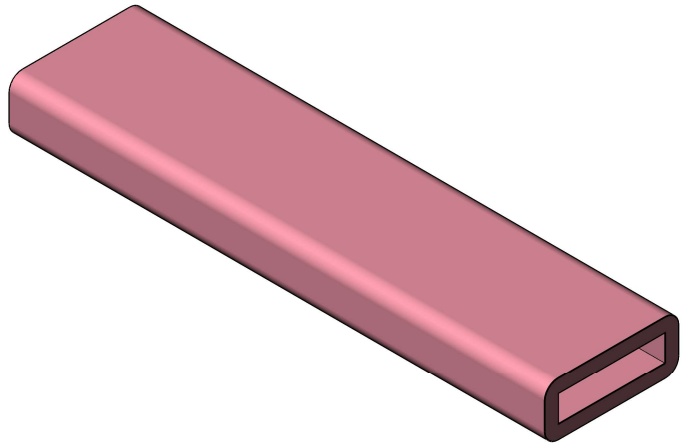
DATE: 04/01/2022	SIGNATURE: 	PROJECT: DESIGN, SIMULATION, CONSTRUCTION AND CHARACTERIZATION OF A VIBRANT MAGNETIC STRUCTURE FOR ITS USE IN MAGNETOSTRICTIVE ENERGY HARVESTERS		
AUTHOR: Daniel Sotelo Aguirre		DENOMINATION: U-SHAPE MAIN BODY	MATERIAL: IRON	WEIGHT (g): 1.388
<b>E.T.S.I.I.I.T</b>	PLANE N°: 1.01	CODE: HARV-101	A4	SCALE: 2:1
<b>upna</b>				





DATE: 12/01/2022	SIGNATURE: 	PROJECT: DESIGN, SIMULATION, CONSTRUCTION AND CHARACTERIZATION OF A VIBRANT MAGNETIC STRUCTURE FOR ITS USE IN MAGNETOSTRICTIVE ENERGY HARVESTERS			
AUTHOR: Daniel Sotelo Aguirre		DENOMINATION: MAGNETOSTRICTIVE SHEET	MATERIAL: GALFENOL	WEIGHT (g): 0.312	
<b>E.T.S.I.I.I.T</b>	PLAN N°: 1.02	CODE: HARV-102		A4	SCALE: 5:1
<b>upna</b>					

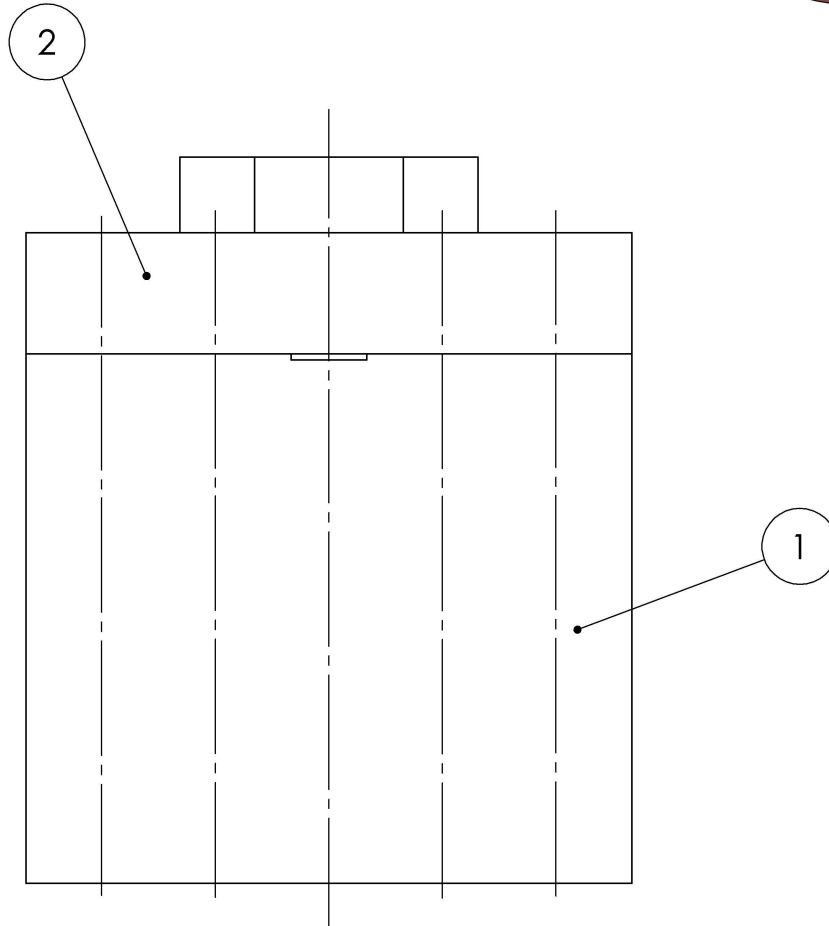
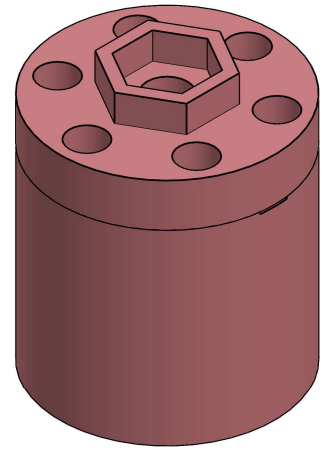



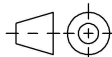


Not indicated radius dimension: 0.5 mm

DATE: 04/01/2022	SIGNATURE: 	PROJECT: DESIGN, SIMULATION, CONSTRUCTION AND CHARACTERIZATION OF A VIBRANT MAGNETIC STRUCTURE FOR ITS USE IN MAGNETOSTRICTIVE ENERGY HARVESTERS		
AUTHOR: Daniel Sotelo Aguirre		DENOMINATION: 3D-PRINTED WIRING PIECE	MATERIAL: PLA	WEIGHT (g): 0.143
<b>E.T.S.I.I.I.T</b>	PLAN N°: 1.03	CODE: HARV-103		SCALE: 5:1
<b>upna</b>			A4	

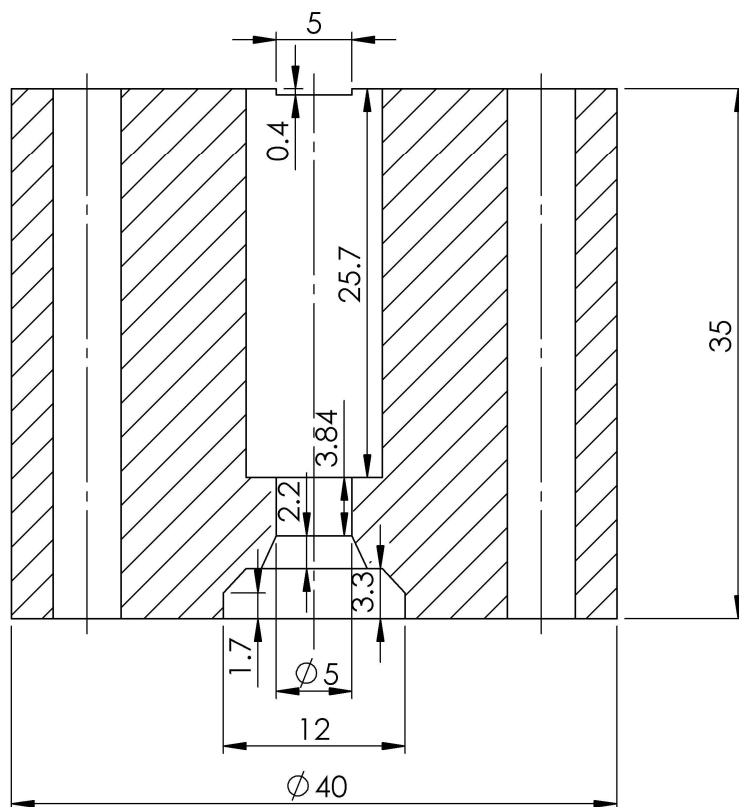
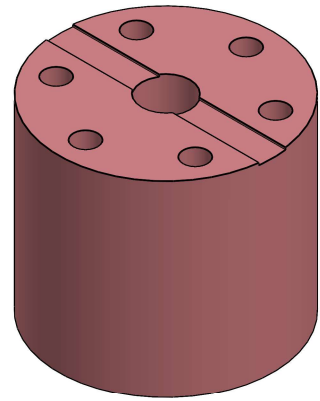
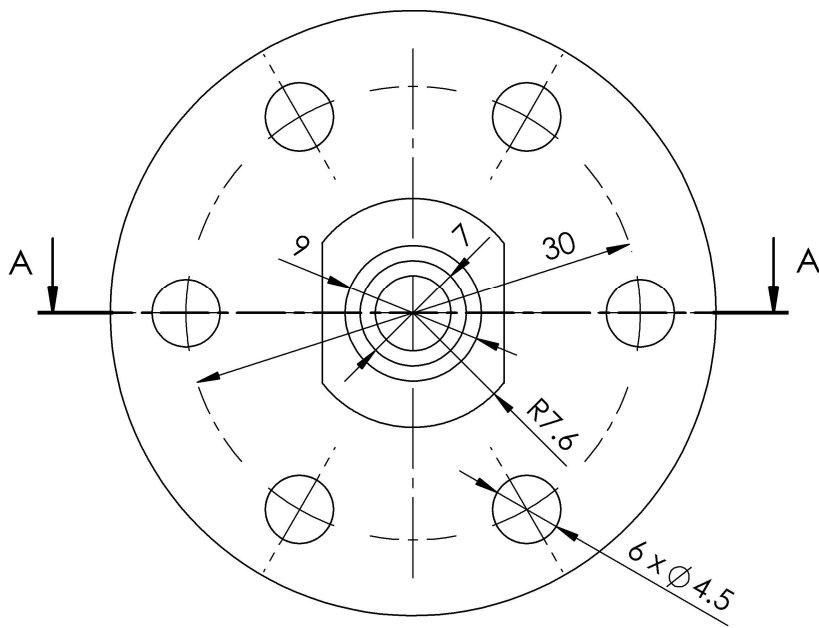




ELEMENT N°	CODE	DESCRIPTION	MATERIAL	QUANTITY
1	HARV-201	BOTTOM 3D-PRINTED HARVESTER SUPPORT	PLA	1
2	HARV-202	UPPER 3D-PRINTED HARVESTER SUPPORT	PLA	1
DATE: 04/01/2022		SIGNATURE: 		
AUTHOR: Daniel Sotelo Aguirre		PROJECT: DESIGN, SIMULATION, CONSTRUCTION AND CHARACTERIZATION OF A VIBRANT MAGNETIC STRUCTURE FOR ITS USE IN MAGNETOSTRICTIVE ENERGY HARVESTERS		
<b>E.T.S.I.I.I.T</b>		DENOMINATION: HARVESTER SUPPORT SYSTEM		WEIGHT (g): 58.36
<b>upna</b>		PLAN N°: 2.00	CODE: HARV-200	 A4 SCALE: 2:1

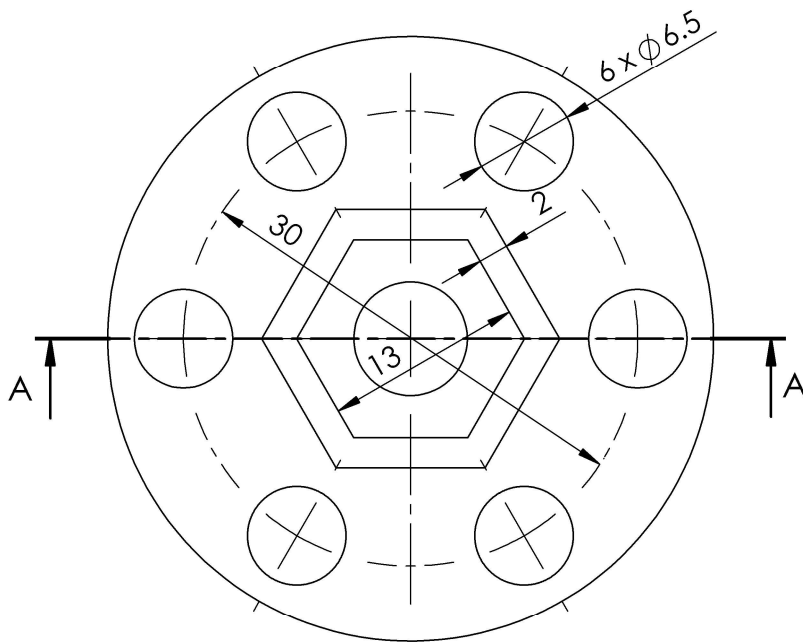
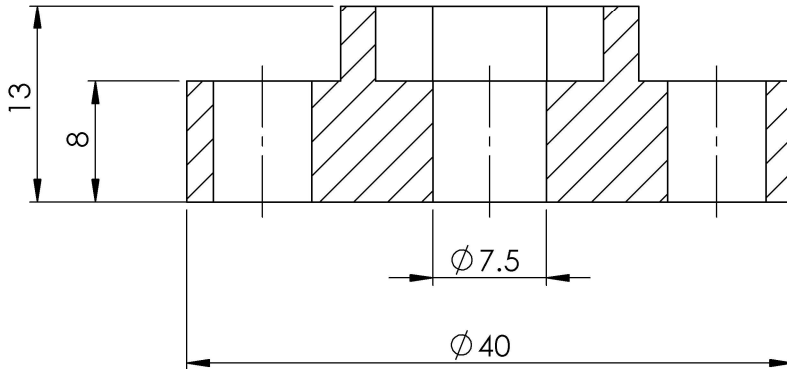
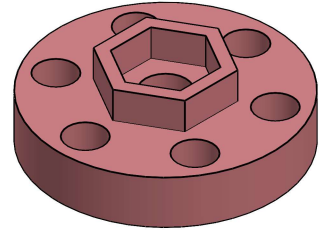






DATE: 04/01/2022	SIGNATURE: 	PROJECT: DESIGN, SIMULATION, CONSTRUCTION AND CHARACTERIZATION OF A VIBRANT MAGNETIC STRUCTURE FOR ITS USE IN MAGNETOSTRICTIVE ENERGY HARVESTERS
AUTHOR: Daniel Sotelo Aguirre	DENOMINATION: BOTTOM 3D-PRINTED HARVESTER SUPPORT	MATERIAL: PLA
<b>E.T.S.I.I.I.T</b>	PLAN Nº: 2.01	WEIGHT (g): 47.66
<b>upna</b>	CODE: HARV-201	SCALE: 2:1
		A4





DATE: 04/01/2022	SIGNATURE: 	PROJECT: DESIGN, SIMULATION, CONSTRUCTION AND CHARACTERIZATION OF A VIBRANT MAGNETIC STRUCTURE FOR ITS USE IN MAGNETOSTRICTIVE ENERGY HARVESTERS
AUTHOR: Daniel Sotelo Aguirre	DENOMINATION: UPPER 3D-PRINTED HARVESTER SUPPORT	MATERIAL: PLA
<b>E.T.S.I.I.I.T</b>	PLAN N°: 2.02	WEIGHT (g): 10.7
<b>upna</b>	CODE: HARV-202	SCALE: 2:1
		A4



## Appendix B

# Optimal Galfenol Sheet Selection for the Future Harvester

In this appendix it is shown how the optimal selection of the Galfenol magnetostrictive sheet should be made for the future harvester construction. The two main factors that are considered are the average stresses in the magnetostrictive layer under vibration and the magnetization function of the material.

By using function `calc_vol_average.m` the average stress in the magnetostrictive material sheet for the simulated vibration conditions could be determined for the four-domain geometry. By summing the average constant stress generated due to the static gravity load and the amplitude of the average stress due to the oscillatory acceleration produced by the vibration source, the average stresses that the magnetostrictive material would suffer along one vibration cycle could be known (see Code C.9).

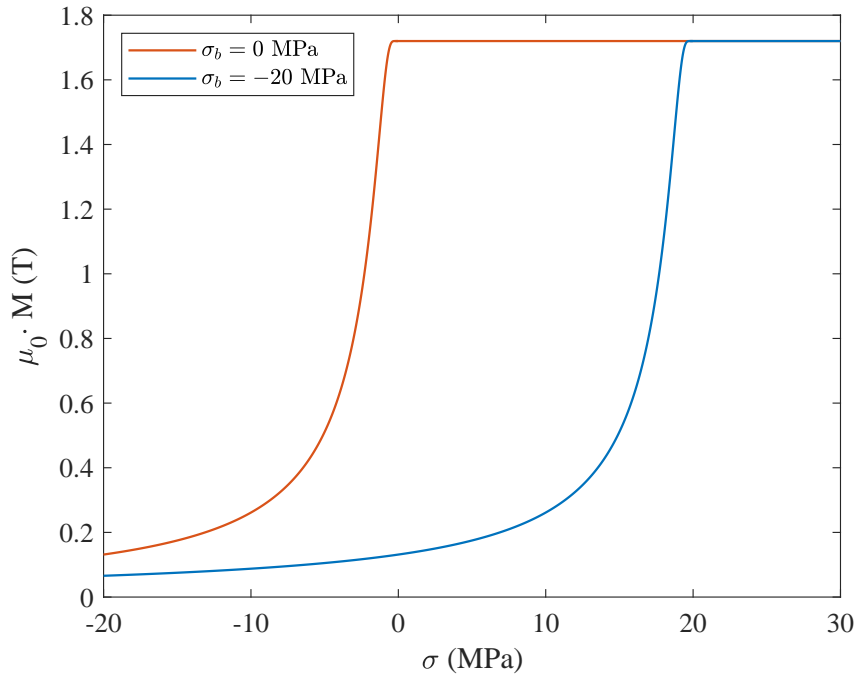
After knowing the average stresses in the magnetostrictive material along one period of vibration, it is modeled the magnetization of Galfenol as a function of the applied stresses. This magnetostrictive material can be manufactured with or without applied compressive stress during the annealing process. Different performance is expected from the different types of Galfenol pieces. The as-cast state produces changes in the magnetization only when compressive loads are applied. Under tensile stresses (one-half of the vibration) the material is magnetically saturated and no changes in the magnetization are produced. The stress annealing process permits the translation of the as-cast magnetization curve, leading to a magnetization change interval under both compressive and tensile stress, consequently optimizing the energy conversion.

The equation provided in [28] is employed for determining the magnetization dependence on the applied stress on Galfenol. In this equation, the applied compressive stress in the manufacturing process,  $\sigma_b$ , is a parameter. This way, it can be determined, together with the information provided by Code C.9 about the average stresses in the active material along one vibration cycle, which is the manufacturing stress that should be demanded to the provider.

The best solution will be the one for which the maximum magnetization variation is produced at the average total stress at which the Galfenol sheet is working (which could be determined from Code C.9). This way, the magneto-mechanical coupling will be maximized. Equation B.1 models the Galfenol magnetization as a function of the magnetic field intensity and the applied stress as shown in [28].

$$M(H, \sigma) = \frac{\alpha \cdot \frac{H}{\gamma \cdot (\sigma + \sigma_b)}}{\beta + \left(\frac{H}{\gamma \cdot (\sigma + \sigma_b)}\right)^4} + M_s \cdot \tanh \frac{H}{\gamma \cdot (\sigma + \sigma_b)} \quad (\text{B.1})$$

In this equation,  $M_s$  is the magnetic saturation,  $\sigma_b$  is the built-in stress due to the stress annealing process (limited by TdVib LLC, the supplier of the Galfenol sheets),  $\alpha$ ,  $\beta$  and  $\gamma$  are some model parameters and  $H$  is the magnetic field intensity due to the bias flux magnet. The values that have been given to the different parameters are the ones in [28] since this simulation will be taken as an approximation:  $M_s = 1.72$  T,  $\alpha = 1.1233$  T,  $\beta = 0.8415$  and  $\gamma = -9.7927 \cdot 10^{-5}$  T<sup>-1</sup>. The magnetic field intensity from the Nd magnet is expected to be between 100 and 200 A/m in the Galfenol sheet, so it is set at  $H = 150$  A/m. The code corresponding to this simulation is Code C.17. Figure B.1 shows the Galfenol magnetization curves for the two built-in stresses available from the manufacturer TdVib LLC.



**Figure B.1:** Galfenol magnetization curves for the two built-in stresses available from the manufacturer TdVib LLC.

It must be noticed that the built-in stress corresponding to the maximum magnetization variation should be chosen, but if real stresses are actually higher, the material would saturate and no variation in the magnetization would be appreciated, so the harvester performance would be severely affected. The manufacturer was only able to provide Galfenol sheets as-grown without any stress applied during the annealing process, or with a compressive stress of  $-20$  MPa during the annealing process. Taking into account the risks of just acquiring the stress annealed galfenol sheets due to the high compression stress values, it is decided to acquire both types of Galfenol sheets in order to analyze how it affects the future harvester performance.

With respect to the vibrant structure that is being analyzed in this project, this Galfenol sheet purchase decision does not have any implications since mechanical properties will not be affected. This election will only be affecting the future harvester performance which will integrate the structure developed in this work.

---





# Appendix C

## MATLAB<sup>®</sup> Scripts

### C.1. MechanicalSimulation.m

In this main script a mechanical simulation is done to calculate the modes of vibration and the displacements and stresses of the prototype. This script will help to determine if the geometry is valid (first mode of vibration close to 100 Hz) and to optimize the model (maximize the average stress in the magnetostrictive material).

#### Code C.1: Geometry and PDE Problem Definition

```
1 clear all;
2 close all;
3 clc;
4
5 % Create the PDE model with three unknowns: displacements in directions
6 % x, y and z.
7 elastic_model = createpde(3);
8
9 % Load the 3D harvester geometry file from the nodes and elements by running the file Gmsh_mesh_data.m.
10 % The positions of the nodes are scaled so that the dimensions are in meters instead of milimeters.
11 Gmsh_mesh_data
12 nodes = msh.POS'*1e-3; elem = msh.TETS; groupsID = elem(:, 5);
13 elem = elem(:, 1:4); elem = elem';
14
15 % Create the geometry from the nodes and the elements loaded.
16 gm = geometryFromMesh(elastic_model, nodes, elem, groupsID);
17
18 % Figure to know how the program names the geometry domains and faces.
19 figure('Name', 'Harvester geometry identification (dimensions in m)')
20 subplot(1, 2, 1);
21 pdegplot(elastic_model, 'FaceLabels', 'off', 'CellLabels', 'on', 'FaceAlpha', 0.5);
22 title('Harvester domain identification (dimensions in m)');
23
24 subplot(1, 2, 2);
25 pdegplot(elastic_model, 'FaceLabels', 'on', 'CellLabels', 'off', 'FaceAlpha', 0.5);
26 title('Harvester face identification (dimensions in m)');
```

#### Code C.2: Coefficients Definition and Boundary Conditions

```
1 % Define the material properties of the different domains.
2 % The main body of the harvester (Cell 1) is made of gray cast iron:
3 % - Young Modulus (E) = 110 GPa (initial approximation)
```

```

4 % – Poisson's Ratio (nu) = 0.28
5 % – Density (rho) = 7200 kg/m^3
6
7 % The tip mass (Cell 2) is made of ferrite:
8 % – Young Modulus (E) = 200 GPa
9 % – Poisson's Ratio (nu) = 0.291
10 % – Density (rho) = 7870 kg/m^3
11
12 % The magnetostrictive material (Cell 3) is made of Galfenol:
13 % – Young Modulus (E) = 59 GPa
14 % – Poisson's Ratio (nu) = 0.44
15 % – Density (rho) = 7800 kg/m^3
16
17 % The wiring piece (Cell 4) is made of PLA:
18 % – Young Modulus (E) = 3.5 GPa
19 % – Poisson's Ratio (nu) = 0.36
20 % – Density (rho) = 1240 kg/m^3
21
22 % This code corresponds to the two-domain geometry simulation. In order to do the four-domain geometry
23 % simulation, the parameters for the two additional domains must be defined here.
24 E = [110e9; 200e9];
25 nu = [0.28; 0.291];
26 % Note density of domain 2 is defined based on the tip mass as it can be next seen.
27 rho = [7200; 0];
28
29 % In the case of the tip mass, the variable desired to be controlled is the added mass. However, since the
30 % parameter needed is the density, it will be calculated by dividing the mass variable by the volume
31 % corresponding to the volume of domain C2.
32
33 % Tip mass in kg (S.I.):
34 % – First configuration (just U-shaped body and ferrite magnet): 0.4781 g.
35 % – Second configuration (U-shaped body, Galfenol sheet and ferrite magnet): 0.4781 g.
36 % – Third configuration (U-shaped body, Galfenol sheet, ferrite magnet and additional tip mass): 2.6753 g.
37 m = 0.4781e-3;
38
39 % In order to calculate the volume of the tip mass the function calc_vol_average.m is employed. This function
40 % can provide both the volume of a domain and the volumetric average of a magnitude in that domain. In this
41 % case the interest is put just on the second output of the function which gives the volume. The first output
42 % will be used later in the simulation. To see further details on the function used go to the file
43 % calc_vol_average.m.
44 [~, volume_tip_mass] = calc_vol_average(elastic_model, 0, 2);
45 rho(2) = m / volume_tip_mass; % Density value.
46
47 g = 9.81; % Gravity value.
48
49 % Calculation of elasticity c matrices considering the materials isotropic.
50 c = [elasticityC3D(E(1), nu(1)), elasticityC3D(E(2), nu(2))];
51
52 % Coefficients are specified using specifyCoefficients function
53 % considering the two domains: the main body (Cell 1) and the tip mass
54 % (Cell 2).
55 for i = 1:gm.NumCells
56     specifyCoefficients(elastic_model, 'm', rho(i), 'd', 0, 'c', c(:, i), 'a', 0, 'f', 0, 'Cell', i);
57 end
58
59 % Define the boundary conditions, in this case we want face F2
60 % (see Figure 3.10) to be fixed to the reference system, that is, a Dirichlet
61 % type condition with displacement vector: u = [0; 0; 0].
62 applyBoundaryCondition(elastic_model, 'dirichlet', 'Face', 2, 'u', [0; 0; 0]);

```

## Code C.3: Mesh Generation

```

1 % If the Matlab meshing is desired instead of the one generated by Gmsh, uncomment the following command
2 % (Hmax defines the maximum size of the mesh elements):
3 % generateMesh(elastic_model , 'Hmax', 5e-4);
4
5 % Figure to visualize the obtained meshing.
6 figure('Name', 'Harvester mesh')
7     pdeplot3D(elastic_model);
8     title('Harvester mesh');

```

## Code C.4: Solution: Resonance Frequencies

```

1 % Look for the frequencies and resonance modes between 0 and 1e9 and save the solution in res_n.
2 res_n = solvepdeeig(elastic_model, [0, 1e9]);
3
4 % The solutions for the resonance are inside the part .Eigenvalues. The values of the natural frequencies are to
5 % the square so we operate with the square root.
6 omegas = sqrt(res_n.Eigenvalues);
7
8 % The natural frequency (rad/s) is: omega = 2*pi*f so we determine the resonance frequencies as:
9 fn = omegas/(2*pi);
10
11 % Table with the resonance frequencies.
12 tmodalResults = table((1:length(fn)), fn);
13 tmodalResults.Properties.VariableNames = {'Mode', 'Frequency (Hz)'};
14 disp(tmodalResults);

```

## Code C.5: Animation of the Prototype's First 6 Modes of Vibration

```

1 % Create a modal-solid.
2 model_animated = createpde('structural','modal-solid');
3
4 % Geometry is built as before from the mesh file Gmsh_mesh_data.m and then scaled so that all dimensions
5 % are in m (S.I.). In order to minimize the memory necessary to calculate the frames of the animation, a
6 % coarser meshing can be employed since data is not wanted to be used quantitatively but qualitatively in this
7 % case.
8 gm_animated = geometryFromMesh(model_animated, nodes, elem, groupsID);
9 generateMesh(model_animated, 'Hmax', 0.001);
10
11 % Define the structural properties of each of the domains.
12 for i = 1:gm_animated.NumCells
13     structuralProperties(model_animated, 'Cell', i, 'YoungsModulus', E(i), 'PoissonsRatio', nu(i), ...
14     'MassDensity', rho(i));
15 end
16
17 % Define the boundary condition, consisting on the lower face to be fixed (which was seen in Figure 1 to be
18 % Face 2).
19 structuralBC(model_animated, 'Face', 2, 'Constraint', 'fixed');
20
21 % Solve the model for the given frequency range.
22 RF = solve(model_animated, 'FrequencyRange', [0, 4000] * 2 * pi);
23
24 % With the function animateHarvester.m each of the frames is obtained in order to see the modes of vibration
25 % animation.
26 frames = animateHarvester(RF, omegas);
27 % Finally, the animation is created by the function movie(), which plays the created frames. The figure is
28 % configured to be able to be seen completely once the animation has started. 8 is the times the movie is
29 % played and 30 the FPS.
30 movie(figure('units', 'normalized', 'outerposition', [0 0 1 1]), frames, 8, 30)

```

## Code C.6: Solution: Gravity Load, Deformations and Stresses

```

1 % In this case it is taken into account the gravity force F.
2 f_grav = rho' .* [0; 0; -g];
3
4 % The coefficients are defined for each of the domains (cells).
5 for i = 1:gm.NumCells
6     specifyCoefficients(elastic_model, 'm', 0, 'd', 0, 'c', c(:, i), 'a', 0, 'f', f_grav(:, i), 'Cell', i);
7 end
8
9 % Solve the PDE.
10 res_static = solvepde(elastic_model);
11
12 % Tension amplitude in the x direction (gradient of c).
13 [cgradx_static, ~, ~] = evaluateCGradient(res_static);
14
15 figure('Name', 'Z-displacement and \sigma_{xx} under gravity load (MPa)')
16 subplot(1, 2, 1);
17 pdeplot3D(elastic_model, 'ColorMapData', ...
18     res_static.NodalSolution(:, 3) * 1e3);
19 title('Displacement in Z direction (mm)');
20
21 subplot(1, 2, 2);
22 pdeplot3D(elastic_model, 'ColorMapData', cgradx_static(:, 1) * 1e-6);
23 title('\sigma_{xx} under gravity load (MPa)');

```

## Code C.7: Damping Coefficients Determination

```

1 % Create a modal-solid.
2 model_freq = createpde('structural', 'frequency-solid');
3
4 % Create the geometry from the nodes and the elements loaded.
5 gm = geometryFromMesh(model_freq, nodes, elem, groupsID);
6
7 % Definition of the damping parameters of the system (suppositions)
8 E(1) = 113e9;
9 alpha = 1;
10 beta = 0.00003;
11 structuralDamping(model_freq, 'Alpha', alpha, 'Beta', beta);
12
13 % Define the structural properties of each of the domains.
14 for i = 1:gm.NumCells
15     structuralProperties(model_freq, 'Cell', i, 'YoungsModulus', E(i), 'PoissonsRatio', nu(i), ...
16         'MassDensity', rho(i));
17 end
18
19 % Define the boundary condition, consisting on the lower face to be fixed (which was seen to be Face 2).
20 structuralBC(model_freq, 'Face', 2, 'Constraint', 'fixed');
21 % Solve the model for the given frequency range.
22 freqList = 40:2.5:150;
23 omegaList = freqList*2*pi;
24
25 for ifreq = 1:length(freqList)
26     % Body load due to non-inertial reference frame. If A is the
27     % acceleration of the shaker (amplitude of 0.1 mm):
28     A = 0.1e-3 * omegaList(ifreq)^2;
29     structuralBodyLoad(model_freq, 'GravitationalAcceleration', [0; 0; A]);
30     RF = solve(model_freq, [1, omegaList(ifreq)]);
31
32     % Create a matrix where the displacement in the z direction for each frequency in freqList is shown in each
33     % column.
34     uz(:, ifreq) = RF.Displacement.z(:, 2);
35     fprintf('Frequency: %f Hz\n', freqList(ifreq))
36 end

```

```

37 % Average displacement of the magnet at the tip (domain 2)
38 [mean_uz, V] = calc_vol_average(elastic_model, uz , 2);
39
40 % Define the data found in the laboratory, both the frequencies and the displacements in the z direction (X_0)
41 freqListLab1 = [40, 50, 60, 70, 80, 90, 100, 105, 110, 115, 117, 120, 125, 130, 140, 150];
42
43 uzLab1 = [0.0302564, 0.0772085, 0.0735968, 0.0974341, 0.1292171, 0.2325118, 0.5720119, 1.2365653, ...
44          2.3778636, 3.0568639, 1.9574613, 0.9331822, 0.3148586, 0.0880436, 0.0504819, 0.0894883];
45
46 lorentzEq = 'a + 2*b/3.14159254 * c/(4*(x-d)^2 + c^2)';
47 startPoints = [0 185 10 115];
48 p_th = fit( freqList', (abs(mean_uz)*1000)', lorentzEq, 'Start', startPoints);
49 p_lab1 = fit( freqListLab1', uzLab1', lorentzEq, 'Start', startPoints);
50
51 % Plot the average displacement of the tip mass for each frequency.
52 figure('Name', 'Comparison between theoretical and experimental resonance frequency results')
53 pth = plot(p_th, 'r', freqList, abs(mean_uz)*1000, 'k o'); hold on;
54 set(pth, 'Linewidth', 1);
55 plab = plot(p_lab1, 'b', freqListLab2, uzLab2, 'k d'); hold off;
56 set(plab, 'Linewidth', 1);
57 xlabel('Frequency (Hz)', 'FontSize', 12);
58 ylabel(['X_{0}', ' (mm)'], 'FontSize', 12);
59 xlim([40, 150]); ylim([-0.1, 5.5]);
60 legend({'Theoretical model: E = 113 GPa; ', '$\alpha = 1$ s$^{-1}$', '$\beta = 0.00003$ s'], ...
61        'Theoretical model Lorentz fit', 'Experimental data', 'Empirical model Lorentz fit'}, 'interpreter', ...
62        'latex', 'FontSize', 11, 'Location', 'Northwest');
63 set(gca, 'fontname', 'times', 'fontsize', 12);

```

## Code C.8: Solution: Harmonic Load, Deformations and Stresses

```

1 % Create a modal-solid.
2 model_harmonic = createpde('structural', 'frequency-solid');
3 % Create the geometry from the nodes and the elements loaded.
4 gm = geometryFromMesh(model_harmonic, nodes, elem, groupsID);
5
6 % Definition of the damping parameters of the system
7 structuralDamping(model_harmonic, 'Alpha', alpha, 'Beta', beta);
8
9 % Define the structural properties of each of the domains.
10 for i = 1:gm.NumCells
11     structuralProperties(model_harmonic, 'Cell', i, 'YoungsModulus', E(i), 'PoissonsRatio', nu(i), ...
12     'MassDensity', rho(i));
13 end
14
15 % Define the boundary condition, consisting on the lower face to be fixed (which was seen to be Face 2).
16 structuralBC(model_harmonic, 'Face', 2, 'Constraint', 'fixed');
17
18 % Solve the model for the desired frequency.
19 freq = 113;
20 omega = freq*2*pi;
21
22 % Body load due to non-inertial reference frame. If A is the acceleration of the shaker in m/s^2:
23 A = 10;
24 structuralBodyLoad(model_harmonic, 'GravitationalAcceleration', [0; 0; A]);
25
26 % Two different omega values are needed for it to work, so only the values corresponding to omega will be
27 % considered.
28 RF = solve(model_harmonic, [1, omega]);
29
30 % The z displacement is the vector in the second column of RF.Displacement.z (the column that corresponds
31 % to omega).
32 uz = RF.Displacement.z(:, 2);
33

```

```

34 % The amplitude of the tension in the x direction is the one desired. It puts a "_0" to indicate it is the
35 % amplitude of the tension. Sigma_xx is calculated using the function evaluateStress:
36 stresses = evaluateStress(RF);
37 sxx_harmonic_0 = abs(stresses.xx(:, 2));
38 % modulus because the solutions are complex
39
40 % Finally plot two figures with the amplitudes of the tensions and the displacements. The displacement in the
41 % z direction has already been calculated: uz, but since the solution is complex the modulus is calculated with
42 % abs().
43 figure('Name', ['Z-displacement and \sigma_{xx} under dynamic', 'load (MPa)'])
44 subplot(1, 2, 1);
45 pdeplot3D(elastic_model, 'ColorMapData', abs(uz)*1e3);
46 title('Displacement in Z direction (mm)');
47
48 subplot(1, 2, 2);
49 pdeplot3D(elastic_model, 'ColorMapData', sxx_harmonic_0*1e-6);
50 title('\sigma_{xx} under dynamic load (MPa)');

```

#### Code C.9: Stresses in the magnetostrictive material

```

1 % For the design of the harvester it is very significant to achieve a relevant value of stress in the x direction in
2 % the magnetostrictive material since this will affect directly the magnetic field created according to the Villari
3 % effect. In order to obtain the mean value of stress in the x direction in the magnetostrictive sheet (Cell 3),
4 % the previously commented function, calc_vol_average.m is used. Consult the file calc_vol_average.m for
5 % further details on how it works.
6
7 % Calculate the average stress in the x direction in the case of the static load in the magnetostrictive sheet.
8 [avg_sxx_grav, ~] = calc_vol_average(elastic_model, cgradx_static(:, 1) * 1e-6, 3);
9
10 % Calculate the average stress in the x direction in the case of the harmonic load in the magnetostrictive sheet
11 % (Cell 3). It can be noted that this average value calculated in this case is the amplitude.
12 [avg_sxx_harmonic_0, ~] = calc_vol_average(elastic_model, sxx_harmonic_0*1e-6, 3);
13
14 % Calculate a time vector for one period divided in 100 time steps and calculate the vector of the average
15 % stress due to harmonic load during one period by multiplying the amplitude calculated before by the sine
16 % of the natural frequency times the time vector.
17 time_vector = 0:1/freq/100:1/freq;
18 avg_sxx_harmonic = avg_sxx_harmonic_0*sin(omega*time_vector);
19
20 % Plot the average stress in the x direction in the magnetostrictive sheet due to gravity load, harmonic load
21 % produced by the accelerometer and to both of them (total load) during one period of the oscillatory load.
22 figure('Name', ['Average \sigma_{xx} in the magnetostrictive laminate along one cycle on the accelerometer', ...
23 '(10 m/s^2)']);
24 hold on; yline(avg_sxx_grav, 'k', 'LineWidth', 0.8);
25 plot(time_vector, avg_sxx_harmonic, 'LineWidth', 0.8);
26 plot(time_vector, avg_sxx_harmonic + avg_sxx_grav, 'LineWidth', 2); hold off;
27 xlim([0, 1/freq]);
28 xlabel('Time (s)', 'FontSize', 12);
29 ylabel(['\sigma_{xx}', ' (MPa)'], 'FontSize', 12);
30 legend({'\overline{\sigma}_{xx};gravity;load}', '$\overline{\sigma}_{xx};harmonic;load$', ...
31 '$\overline{\sigma}_{xx};total;load$', 'interpreter', 'latex', 'FontSize', 16);
32 title(['Average \sigma_{xx} in the magnetostrictive laminate along one cycle on the accelerometer', ...
33 '(10 m/s^2)'], 'FontSize', 14);

```

## C.2. animateHarvester.m

The function `animateHarvester.m` calculates the frames of the periodic deformation with time, scaled so that it is observable, of a harvester for the first six modes of vibration. This code is based on the example in [27]. The inputs and outputs of this function are shown in Table C.1.

**Table C.1:** Inputs and outputs of the function `animateHarvester.m`.

INPUTS	- R	: solution of the desired modal structural solid for a certain frequency range.
	- omegas	: column vector with the natural frequencies corresponding to the different modes of vibration of the harvester.
OUTPUTS	- frames	: the desired number of frames (can be changed in the animation parameters) for the six first modes of vibration of the harvester.

### Code C.10: Function `animateHarvester.m`

```

1 function frames = animateHarvester(R, omegas)
2     % Animation parameters.
3     scale = 8e-5;
4     nFrames = 30; % Number of total frames.
5     flexibleModes = 1:6; % Interval of modes of vibration of interest.
6
7     % Create a deformed model for plotting purpose.
8     deformedModel = createpde('structural', 'modal-solid');
9
10    % Undeformed mesh data.
11    nodes = R.Mesh.Nodes;
12    elements = R.Mesh.Elements;
13
14    % Construct pseudo time-vector that spans one period of first six modes.
15    omega = omegas(1:6);
16    timePeriod = 2*pi./omegas(1:6); % Time period is T = 2*pi/omega.
17
18    % Create figure from where capturing the frames.
19    h = figure('units', 'normalized', 'outerposition', [0 0 1 1]);
20    % Plot deformed shape of the first six flexible modes and capture frame
21    % for each pseudo time step.
22    for n = 1:nFrames
23        for modeID = 1:6
24            % Construct a modal deformation and a modulus matrix.
25            modalDeformation = [R.ModeShapes.ux(:, flexibleModes(modeID))';
26                                R.ModeShapes.uy(:, flexibleModes(modeID))';
27                                R.ModeShapes.uz(:, flexibleModes(modeID))'];
28
29            modalDeformationMagi = sqrt(modalDeformation(1,:).^2 + ...
30                                       modalDeformation(2,:).^2 + ...
31                                       modalDeformation(3,:).^2);
32            % Normalize the displacement magnitude with respect to the maximum one.
33            modalDeformationMag = modalDeformationMagi/max(modalDeformationMagi);
34
35            % Compute nodal locations of deformed mesh by creating a vector with nFrames between 0 and the

```

```
36 % period of the mode of vibration. Then the deformed positions of the nodes are the ones of the
37 % nodes plus the scaled deformation which is the result of the amplitude (scaled deformation
38 % vector) times the sine of omega times the time.
39 pseudoTimeVector = linspace(0, timePeriod(modeID), nFrames);
40 nodesDeformed = nodes + scale.*modalDeformation*sin(omega(modeID).*pseudoTimeVector(n));
41
42 % Construct a deformed geometric shape using displaced nodes and elements from unreformed
43 % mesh data.
44 geometryFromMesh(deformedModel, nodesDeformed, elements);
45
46 % Plot the deformed mesh with magnitude of mesh as color plot.
47 subplot(2, 3, modeID)
48 pdeplot3D(deformedModel, 'ColorMapData', modalDeformationMag)
49 title(sprintf(['Flexible Mode %d\n', 'Frequency = %g Hz'], modeID, omega(modeID)/2/pi));
50
51 % Remove colorbar for clarity.
52 % colorbar off
53 delete(findall(gca, 'type', 'quiver'));
54
55 % Remove deformed geometry to reuse to model for next mode.
56 deformedModel.Geometry = [];
57 end
58
59 % Capture a frame of six deformed mode for time instant.
60 frames(n) = getframe(h);
61 end
62
63 end
```



### C.3. calc\_vol\_average.m

The function `calc_vol_average.m` calculates the volume average of `u` scalar magnitude in the cell corresponding to `domainID`. The inputs and outputs of this function are given in Table C.2.

**Table C.2:** Inputs and outputs of the function `calc_vol_average.m`.

INPUTS	- modelPDE	:	PDE model as defined by <code>createpde</code> (number of unknowns).
	- u	:	solution column vector with the magnitude at each node. e.g. <code>cgradx_harmonic_0(:, 1)*1e-6</code> .
	- domainID	:	ID number of the domain or cell of interest.
OUTPUTS	- avg	:	volume average of <code>u</code> magnitude in the input cell or domain.
	- V	:	volume of the input cell or domain.

Code C.11: Function `calc_vol_average.m`

```

1 function [avg, V] = calc_vol_average(modelPDE, u, domainID)
2     % Duplicate the model for avoiding overwriting.
3     model = createpde(1);
4     model.Geometry = modelPDE.Geometry;
5     model.Mesh = modelPDE.Mesh;
6     model.BoundaryConditions = modelPDE.BoundaryConditions;
7
8     % Specify the new coefficients so that coefficients for the rest of
9     % domains apart from domainID are null.
10    specifyCoefficients(model, 'm', 0, 'd', 0, 'c', 0, 'a', 0, 'f', 0);
11    specifyCoefficients(model, 'm', 0, 'd', 0, 'c', 0, 'a', 0, 'f', 1, 'Cell', domainID);
12
13    % Volumetric load vector resulting from the integration of the discretized version of the f coefficient.
14    FEMs = assembleFEMatrices(model, 'F');
15    F = FEMs.F;
16
17    % Volume of domainID will be the sum of all the components of F (sum of the volume of all the elements
18    % conforming the domain).
19    V = sum(F);
20
21    % The average of u in domainID will be the volume corresponding to each node times the function u at
22    % each node, all divided by the total volume.
23    avg = F'*u/V;
24
25 end

```

## C.4. ExperimentalData.m

In this script the data collected from the calibration of the displacement sensor and the different resonance analyses is used to elaborate the different plots.

Code C.12: Calibration of the Displacements Sensor (Figure 4.16)

```

1  y = [0.06635, 0.09505, 0.1479, 0.1951, 0.2473, 0.2957, 0.3466, 0.4150, 0.4547, 0.5169, 0.5951, 0.6747, 0.7504, ...
2  0.8300, 0.9058, 0.9915, 1.0834, 1.1505, 1.2375, 1.3294];
3  x = [0.435, 0.512, 0.585, 0.665, 0.750, 0.835, 0.908, 1.020, 1.100, 1.200, 1.290, 1.410, 1.510, ...
4  1.590, 1.680, 1.810, 1.900, 1.960, 2.110, 2.160];
5
6  p = polyfit(x, y, 1);
7  xl = linspace(0, 2.2);
8  yl = polyval(p, xl);
9
10 figure('Name', 'Calibration of the displacement sensor')
11 plot(xl,yl, 'r','Linewidth', 1.5); hold on;
12 xlim([0, 2.2]); ylim([0, 1.35]);
13 plot(x, y, 'k o', 'Linewidth', 1); hold off;
14 xlabel('V_{out} (V)'); ylabel('X_{0} = Y_{0} (mm)');
15 legend({'Regression line','Experimental data'}, 'interpreter', 'latex', 'FontSize', 11, 'Location', 'Northwest');
16 set(gca,'fontname','times', 'fontsize', 12);
17 saveas(gcf, 'Calibration', 'eps')

```

Code C.13: Frequency sweep of the first prototype configuration (Figure 5.1)

```

1  x1 = [40, 50, 60, 70, 80, 90, 100, 105, 110, 115, 117, 120, 125, 130, 140, 150];
2  y1 = [0.0302564, 0.0772085, 0.0735968, 0.0974341, 0.1292171, 0.2325118, 0.5720119, 1.2365653, 2.3778636, ...
3  3.0568639, 1.9574613, 0.9331822, 0.3148586, 0.0880436, 0.0504819, 0.0894883];
4
5  lorentzEq = 'a + 2*b/3.14159254 * c/(4*(x-d)^2 + c^2)';
6  startPoints = [0 183 10 115];
7  p_th1 = fit( x1', y1', lorentzEq, 'Start', startPoints);
8
9  figure('Name', 'Resonance Analysis: Configuration I')
10 hold on;
11 p1 = plot( p_th1, 'r', x1, y1, 'k o');
12 set(p1, 'Linewidth', 1);
13 plot([113.04; 113.04], [0; 3.55], '--', 'Linewidth', 1);
14 text(116, 3.4, '113.04 Hz', 'Color', [0.9290 0.6940 0.1250], 'FontSize', 10); hold off;
15 xlabel('Frequency (Hz)'); ylabel('X_{0} (mm)'); xlim([40, 150]);
16 legend({'Experimental data','Lorentz fit'}, 'interpreter', 'latex', 'FontSize', 11, 'Location', 'Northwest');
17 set(gca,'fontname','times', 'fontsize', 12);
18 saveas(gcf, 'ResI', 'eps')

```

Code C.14: Frequency sweep of the second prototype configuration (Figure 5.6)

```

1  x2 = [40, 50, 60, 70, 80, 90, 100, 105, 106, 107, 108, 109, 110, 111, 112, 113, 114, 115, 116, 117, 120, 130, ...
2  140, 150];
3  y2 = [-0.0246415, 0.0049745, -0.0015266, 0.0447032, 0.1183820, 0.2122862, 0.4275438, 0.7959375, ...
4  0.9548525, 1.1715547, 1.5182782, 2.3272998, 3.6853003, 4.9277262, 4.6676836, 3.9742365, ...
5  2.2406189, 1.9805762, 1.6049591, 0.8920088, 0.4058735, 0.1371628, 0.0331458, 0.0042521];
6
7  lorentzEq2 = 'a + 2*b/3.14159254 * c/(4*(x-d)^2 + c^2)';
8  startPoints = [0 185 10 115];
9  p_th2 = fit( x2', y2', lorentzEq2, 'Start', startPoints);
10
11 figure('Name', 'Resonance Analysis: Configuration II')
12 hold on;

```

```

13 p2 = plot( p_th2, 'r', x2, y2, 'k o');
14 set(p2, 'Linewidth', 1);
15 plot([111.5; 111.5], [0; 5], '--', 'Linewidth', 1);
16 text(115, 4.8, '111.5 Hz', 'Color', [0.9290 0.6940 0.1250], 'FontSize', 10); hold off;
17 xlabel('Frequency (Hz)'); ylabel('X_{0} (mm)');
18 xlim([40, 150]); ylim([-0.1, 5.2]);
19 legend({'Experimental data', 'Lorentz fit'}, 'interpreter', 'latex', 'FontSize', 11, 'Location', 'Northwest');
20 set(gca, 'fontname', 'times', 'fontsize', 12);
21 saveas(gcf, 'ResII', 'eps')

```

Code C.15: Frequency sweep of the third prototype configuration (Figure 5.8)

```

1 x3 = [30, 35, 41, 44, 46, 47, 48, 49, 50, 52, 54, 55, 60, 62, 64, 65, 70, 80, 100];
2 y3 = [-0.0145287, 0.0121979, 0.0483149, 0.0887660, 0.1292171, 0.1797809, 0.2354011, 0.2924661, ...
3 0.3408629, 0.4636608, 0.5575651, 0.7237035, 0.5070012, 0.2924661, 0.2122862, 0.1414969, ...
4 0.0663734, 0.0049745, -0.0044160];
5
6 lorentzEq3 = 'a + 2*b/3.14159254 * c/(4*(x-d)^2 + c^2)';
7 startPoints = [0 120 10 52];
8 p_th3 = fit( x3', y3', lorentzEq3, 'Start', startPoints);
9
10 figure('Name', 'Resonance III')
11 hold on;
12 p3 = plot( p_th3, 'r', x3, y3, 'k o');
13 set(p3, 'Linewidth', 1);
14 plot([56; 56], [0; 0.708], '--', 'Linewidth', 1);
15 text(59, 0.7, '56 Hz', 'Color', [0.9290 0.6940 0.1250], 'FontSize', 10); hold off;
16 xlabel('Frequency (Hz)'); ylabel('X_{0} (mm)');
17 xlim([30, 100]); ylim([-0.05, 0.8]);
18 legend({'Experimental data', 'Lorentz fit'}, 'interpreter', 'latex', 'FontSize', 11, 'Location', 'Northeast');
19 set(gca, 'fontname', 'times', 'fontsize', 12);
20 saveas(gcf, 'ResIII', 'eps')

```

Code C.16: Comparison between the resonance analyses (Figure 5.9)

```

1 figure('Name', 'Resonance comparison', 'units', 'normalized', 'outerposition', [0, 0, 0.5, 0.8])
2 p1 = plot(p_th1, 'r'); set(p1, 'Linewidth', 1);
3 text(116, 3.4, '113 Hz', 'Color', 'r', 'FontSize', 10); hold on;
4 p2 = plot(p_th2, 'k'); set(p2, 'Linewidth', 1);
5 text(115, 4.8, '111.5 Hz', 'Color', 'k', 'FontSize', 10);
6 p3 = plot(p_th3, 'b'); set(p3, 'Linewidth', 1);
7 text(60, 0.7, '56 Hz', 'Color', 'b', 'FontSize', 10); hold off;
8 xlabel('Frequency (Hz)'); ylabel('X_{0} (mm)');
9 xlim([40, 150]); ylim([0, 6]);
10 legend({'Without Galfenol and 3D-printed piece', 'With Galfenol and 3D-printed piece', ...
11 'With Galfenol, 3D-printed piece and additional tip mass'}, 'interpreter', 'latex', 'FontSize', 9, ...
12 'Location', 'Northwest');
13 set(gca, 'fontname', 'times', 'fontsize', 12);
14 saveas(gcf, 'Comparative', 'eps')

```

## C.5. GalfenolMagnetizationModel.m

This function model has been extracted from [28] and models the magnetization of the Galfenol material as a function of the applied stress (Figure B.1).

Code C.17: Galfenol Magnetization Function Model

```

1 % Parameters definition
2 alpha = 1.1233; % Three first parameters from the model
3 beta = 0.8415;
4 gamma = -9.7927e-5;
5
6 % Built-in stress in the stress annealing process
7 sigma_b = -20e6;
8 sigma = sigma_b:-0.001*sigma_b:-0.99999*sigma_b;
9 sigma_2 = -0.99*sigma_b:-0.5*sigma_b:-3*sigma_b;
10 sigma_0 = sigma + sigma_b; %Define the vector for the non-applied stress
11 sigma_0_2 = sigma_2 + sigma_b;
12
13 M_s = 1.72; % Magnetic saturation of Galfenol (in T)
14 M_s_list = [];
15 for i = 1:length(sigma_2)
16     M_s_list(i) = M_s;
17 end
18
19 % Magnetic field strength (expected to be between 100 and 200 A/m)
20 H = 150;
21
22 % Applied stress vector
23 f = gamma * (sigma + sigma_b(1));
24 z = H./f;
25 M = alpha * z/(beta + z.^4) + M_s * tanh(z);
26
27 figure('Name', 'Galfenol Magnetization Function Model')
28 plot(sigma_0*10^-6, M, 'Color', [0.8500, 0.3250, 0.0980], 'Linewidth', 1); hold on;
29 plot(sigma_0_2*10^-6, M_s_list,'Color', [0.8500, 0.3250, 0.0980], 'Linewidth', 1);
30 plot(sigma*10^-6, M, 'Color', [0, 0.4470, 0.7410], 'Linewidth', 1);
31 plot(sigma_2*10^-6, M_s_list, 'Color', [0, 0.4470, 0.7410], 'Linewidth', 1);
32 hold off;
33 xlim([-20, 30]);
34 xlabel('\sigma (MPa)', 'FontSize', 12);
35 ylabel('\mu_{0}\cdot M (T)', 'FontSize', 12);
36 legend({'\sigma_b = 0$ MPa', '\sigma_b = -20$ MPa'}, 'interpreter', 'latex', 'FontSize', 10, ...
37 'Location', 'Northwest');
38 set(gca,'fontname','times', 'fontsize', 12);
39 saveas(gcf, 'Magnetization', 'eps')

```